

Biaxial Tension Testing of 8-in. (200-mm) Diameter TR-XTREME™ Ductile Iron pipe

Shih-Hung Chiu

Qinglai Zhang

Shakhzod Takhirov

Kenichi Soga



Berkeley
CENTER FOR
Smart Infrastructure

CSI Report 2023/02
Center for Smart Infrastructure (CSI)
Department of Civil and Environmental Engineering
University of California, Berkeley May 2023

EXECUTIVE SUMMARY

This report describes the experimental and numerical results of the biaxial tension tests (combined bending and tension force) performed on 8 inches TR-XTREME™ ductile iron pipe manufactured by U.S. Pipe. The purpose of the testing is to evaluate the load capacity, joint opening characteristics, and the failure mechanism of the TR-XTREME™ restrained joint, which is designed to be used in areas of seismic activity. The two biaxial tension tests were performed for different orientations of the locking segments at the bell joint connection. The data obtained from distributed fiber optic sensors are used to validate the three-dimensional (3D) finite element (FE) model. The model can be used as a reference model for future related pipeline tests and optimizing pipeline design and installation.

Keywords: *Ductile iron pipe, water pipelines, biaxial tension, fiber optic, finite element analysis.*

ACKNOWLEDGMENTS

The East Bay Municipal Utility District (EBMUD) provided the funding for this project, and U.S. Pipe supplied the pipes used for the experiment. Completing the work would not be possible without the support of Llyr Griffith, John Kochan, and Phillip Wong of the University of California, Berkeley. Active involvement and guidance from Jeff Mason of U.S. Pipe and David Katzev of EBMUD are greatly appreciated.

DISCLAIMER

Any opinions, findings, conclusions, or recommendations expressed in this report are those of the author(s) and do not necessarily reflect those of the University of California, Berkeley.

CONTENTS

EXECUTIVE SUMMARY	II
ACKNOWLEDGMENTS.....	III
DISCLAIMER.....	IV
LIST OF FIGURES.....	VII
LIST OF TABLES.....	IX
1. Introduction.....	10
2. Test Setup	13
2.1 Experimental Setup.....	13
2.2 Specimen List.....	14
2.3 Test Procedure.....	15
3. Instrumentation.....	16
3.1 Conventional Instruments	16
3.2 Distributed Fiber Optic Sensors	18
4. Test Results.....	21
4.1 Calculation Approach	21
4.2 Experimental Data Analysis.....	21
4.2.1 Moment and Rotation.....	22
4.2.2 Axial Force and Joint Opening	23
4.2.3 Axial Strain	24
4.2.4 Hoop Strain	30
4.3 Failure Modes	37
5. Finite Element Analysis.....	38
5.1 Overview of numerical model	38
5.2 Determination of Pipe Parameters	39
5.3 FEM Results of Test 1.....	39
5.3.1 Overview of FE analysis	39
5.3.2 Bell deformation.....	41
5.3.3 Spigot deformation.....	42
5.3.4 Strain comparison of the FE Model and Experimental Data	44
5.4 FEM Results of Test 2.....	46
5.4.1 Overview of FE analysis	46
5.4.2 Bell deformation.....	48
5.4.3 Spigot deformation.....	49
5.4.4 Strain comparison of the FE Model and Experimental Data	49
5.5 Failure mode comparison between FEM and experiments.....	51
6. Conclusion.....	54
7. Reference.....	55

<i>Appendix A: Distributed Fiber Optic Sensing</i>	<i>56</i>
<i>Appendix B: Distributed Fiber Optic Sensors Result</i>	<i>58</i>
(a) Test 1.....	58
(b) Test 2.....	64
<i>Appendix C: Comparison of FEM simulation results and experimental results</i>	<i>70</i>
(a) Test 1.....	70
(b) Test 2.....	74

LIST OF FIGURES

Figure 1-1 Mechanism of TR-XTREME™ joint (U.S. Pipe, 2020)	10
Figure 1-2 Recommended installation positions (U.S. Pipe, 2020).....	11
Figure 1-3 Sketch of testing setup and procedure.....	12
Figure 1-4 Cross-section of the joint regarding each stage.....	12
Figure 2-1 Sketch of the experimental setup	13
Figure 2-2 Overview of the experimental setup	14
Figure 2-3 Locking segments orientation	14
Figure 3-1 Instrumentation plan of conventional instruments	17
Figure 3-2 DFOS instrumentation plan.....	19
Figure 4-1 Moment vs. Rotation.....	22
Figure 4-2 Sketch of the bell after Push Down stage.....	23
Figure 4-3 Axial force vs. average joint opening	24
Figure 4-4 Stress distribution of the cross-section of the bell under the Pull stage.....	24
Figure 4-5 Axial strain vs. rotation of Specimen 1	25
Figure 4-6 Axial strain vs. rotation of Specimen 2.....	26
Figure 4-7 Strain development of bell pipe in the longitudinal direction under 8.36-degree rotation. (a) Top side of Specimen 1, (b) West side of Specimen 1, (c) Top side of Specimen 2, (d) West side of Specimen 2	27
Figure 4-8 Strain development of spigot in the longitudinal direction under 8.36-degree rotation condition. (a) Top side of Specimen 1, (b) West side of Specimen 1, (c) Top side of Specimen 2, (d) West side of Specimen 2	28
Figure 4-9 Strain development of bell pipe in longitudinal direction under 140 kips axial force loading condition. (a) Top side of Specimen 1, (b) West side of Specimen 1, (c) Top side of Specimen 2, (d) West side of Specimen 2	29
Figure 4-10 Strain development of spigot in longitudinal direction under 140 kips axial force loading condition. (a) Top side of Specimen 1, (b) West side of Specimen 1, (c) Top side of Specimen 2, (d) West side of Specimen 2	30
Figure 4-11 Hoop strain vs. rotation of Specimen 1	31
Figure 4-12 Hoop strain vs. the rotation of Specimen 2.....	31
Figure 4-13 Strain distribution in the circumferential direction of Specimen 1 under 8.3-degree rotation condition. (a) sensor on the bell pipe (b) sensor at the mid location of the bell (c) sensor on top of the locking segments on the bell (d) sensor on the spigot.....	32
Figure 4-14 Strain distribution in circumferential direction under Specimen 2 under 8.3-degree rotation condition. (a) sensor on the bell pipe (b) sensor at the mid location of the bell (c) sensor on top of the locking segments on the bell (d) sensor on the spigot.....	33
Figure 4-15 Joint deformed mechanism in Push Down stage.....	34
Figure 4-16 Strain distribution in the circumferential direction of Specimen 1 under 140 kips loading condition. (a) sensor on the bell pipe (b) sensor at the mid location of the bell (c) sensor on top of the locking segments on the bell (d) sensor on the spigot.....	35
Figure 4-17 Strain distribution in the circumferential direction of Specimen 2 under 140 kips loading condition. (a) sensor on the bell pipe (b) sensor at the mid location of the bell (c) sensor on top of the locking segments on the bell (d) sensor on the spigot.....	36
Figure 4-18 Failure of Bell of Specimen 1 (left) and 2 (right)	37
Figure 5-1 3-D FE model mesh for biaxial tension tests	38

Figure 5-2 FE mesh for bell joint and initial position of the bell and spigot	39
Figure 5-3 Comparison of FEM results and Test-1 results	40
Figure 5-4 The stress contours of the deformed joint of test 1 (Actuator Push Down)	40
Figure 5-5 The stress contours of the deformed joint of test 1 (Pull)	41
Figure 5-6 The stress contours of bell cross-section: (a) initial stage (b) actuator push down (c) pull	42
Figure 5-7 The stress contours of locking segments: (a) initial stage (b) actuator push down (c) pull	42
Figure 5-8 The stress contours of spigot cross-section: (a) initial stage (b) actuator push down (c) pull	43
Figure 5-9 The deformation of the weld bead	43
Figure 5-10 Comparison of circumferential strains (a) Actuator push down (b) Pull to 2.2 inches	45
Figure 5-11 Comparison of longitudinal strains (a) Actuator push down (b) Pull to 2.2 inches ..	45
Figure 5-12 Comparison of FEM results and Test-2 results	46
Figure 5-13 The stress contours of the deformed joint of test 2 (Actuator Push Down)	47
Figure 5-14 The stress contours of the deformed joint of Test 2 (Pull)	47
Figure 5-15 The stress contours of bell cross-section: (a) initial stage (b) actuator push down (c) pull	48
Figure 5-16 The stress contours of locking segments: (a) initial state (b) actuator push down (c) pull	48
Figure 5-17 The stress contours of spigot cross-section: (a) initial state (b) actuator push down (c) pull	49
Figure 5-18 Comparison of circumferential strains (a) actuator push down (b) pull to 2.2 inches	50
Figure 5-19 Comparison of longitudinal strains (a) actuator push down (b) pull to 2.2 inches ...	51
Figure 5-20 Failure mode comparison of Test 1	51
Figure 5-21 The stress contours of S11, S22, S33, S23 for Test 1	52
Figure 5-22 Failure mode comparison of Test 2	52
Figure 5-23 The stress contours of S11, S22, S33, S23 for Test 2	53

LIST OF TABLES

Table 2-1 Test log	15
Table 2-2 Testing procedure	15
Table 3-1 Conventional instrumentation local names	17
Table 3-2 DFOS local names	20
Table 3-3 Location of longitudinal fiber optic cables.....	20
Table 4-1 Summary of the tests	23
Table 5-1 Ductile Iron Pipe properties.....	39

1.Introduction

This report summarizes the experimental and finite element modeling results of the biaxial tension tests performed on 8-inch TR-XTREME™ earthquake-resistant ductile iron pipe specimens manufactured by U.S. Pipe. The pipe is designed to maintain full water service after seismic events to achieve the seismic resiliency of the pipeline systems. The pipe is equipped with a single-restrained bell joint connection, providing 2.9-inch extension capability and 5-degree deflection contraction capacity. The schematic of the bell joint is shown in Figure 1-1. The spigot is designed to be inserted into the bell, passing through a water-prevent rubber gasket, and is equipped with a weld bead to bear against the locking segments, used as a locking mechanism while pulling. The single slot is used for holding the locking segments. Three white stripes on the spigot are used to indicate the installation position. The manufacturer recommends three installation positions: collapsed, midpoint, and extended location, as shown in Figure 1-2. The Option-B-Midpoint installation was used as the start position of the experiments.

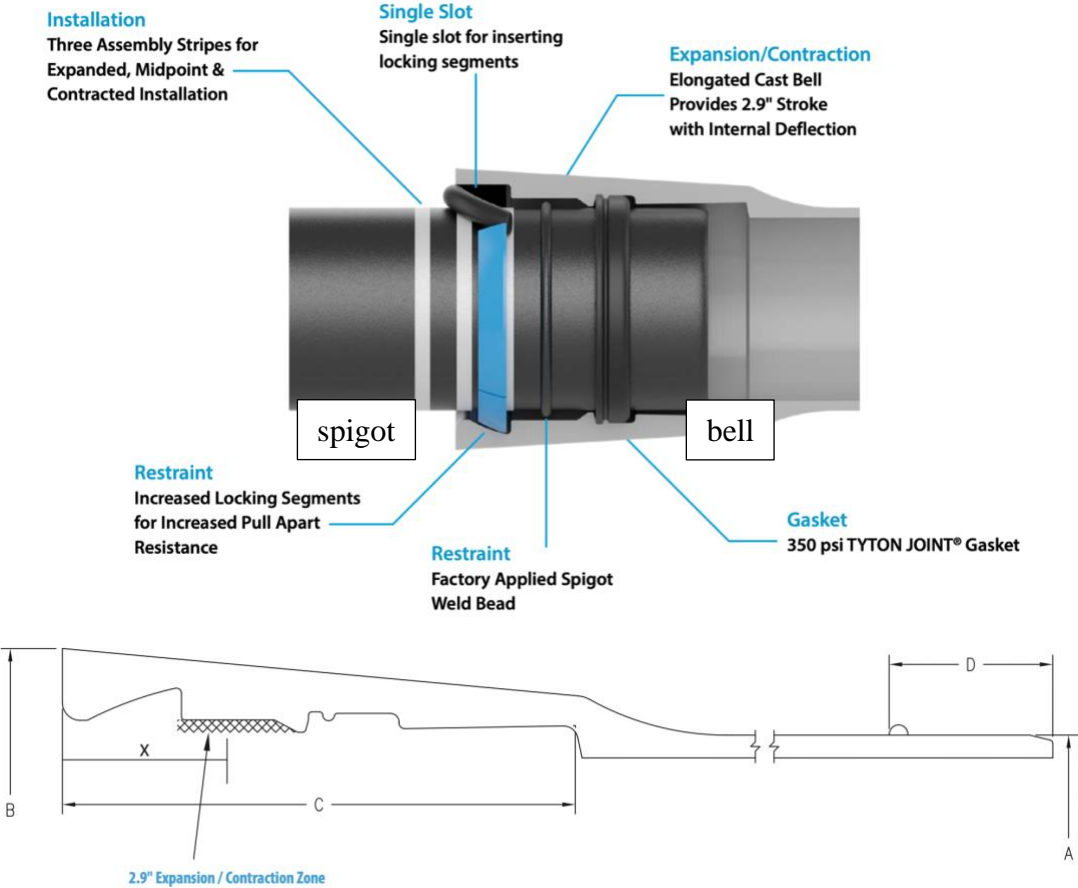
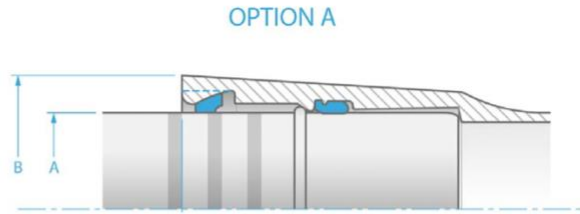
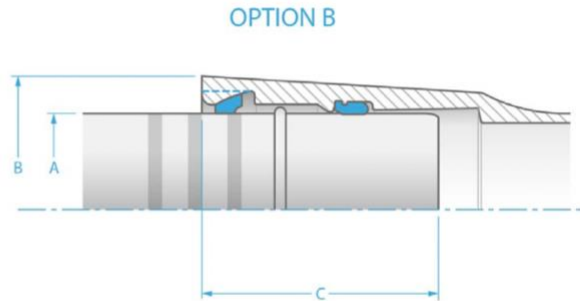


Figure 1-1 Mechanism of TR-XTREME™ joint (U.S. Pipe, 2020)

Option A-Collapsed – Correct assembly is determined when the front edge of the assembly stripe furthest from the spigot tip lines up with the face of the pipe bell as viewed from above, leaving only one assembly stripe shown.



Option B-Midpoint – Correct assembly is determined when the front edge of the middle assembly stripe lines up with the face of the pipe bell as viewed from above, leaving two assembly stripes shown.



Option C-Extended (Restrained) - Correct assembly is determined when the front edge of the assembly stripe closest to the spigot tip lines up with the face of the pipe bell as viewed from above, leaving three assembly stripes shown. This is the proper assembly when immediate joint restraint is required.

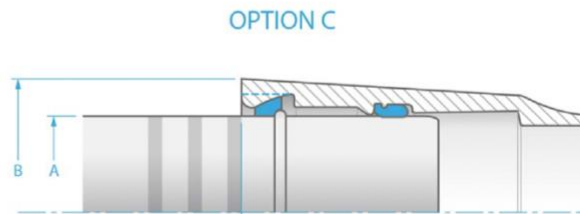


Figure 1-2 Recommended installation positions (U.S. Pipe, 2020)

Two 8-inch TR-XTREME™ pipes with two different orientations of locking segments (the single slot located at 9 o'clock and 12 o'clock, respectively) were used for the biaxial tension tests. A vertical force was first applied to the pipes to push them to an 8-degree deflection contraction. Then, a horizontal axial force was applied in tension until severe pipe damage or water leakage occurred, as shown in Figure 1-3. Figure 1-4 is the cross-section of the joint that demonstrates the behavior of the bell and spigot regarding each stage. The testing objectives are (1) to evaluate the mechanical behavior and capacity of the pipe under combined bending and tension forces and (2) to discuss the effect of the different locking segments' locations on the pipe performance.

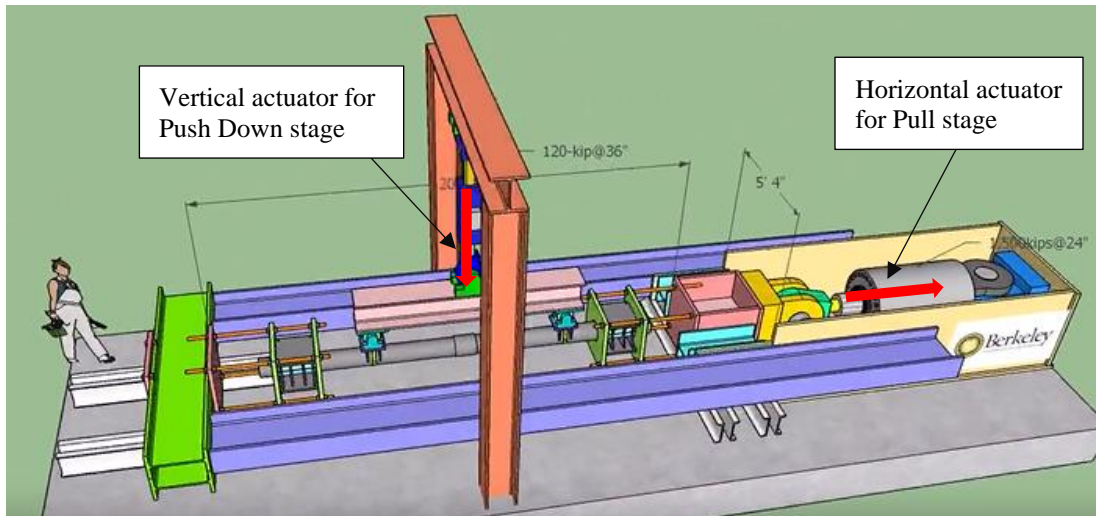
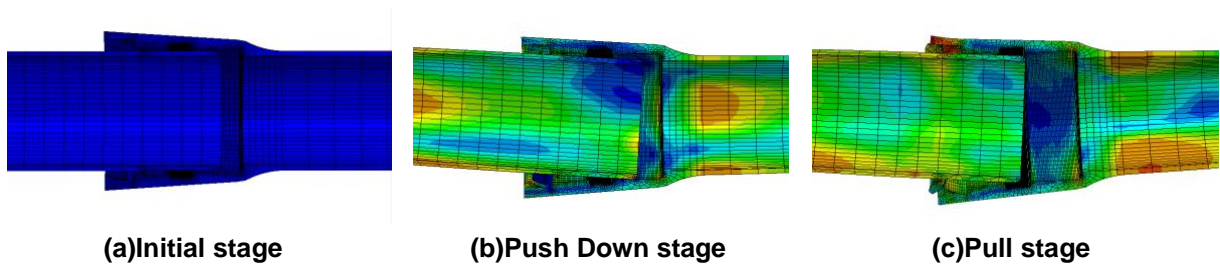


Figure 1-3 Sketch of testing setup and procedure



(a)Initial stage

(b)Push Down stage

(c)Pull stage

Figure 1-4 Cross-section of the joint regarding each stage

In this study, distributed fiber optic sensors (DFOS) were utilized to measure the continuous strain development of the pipeline in the longitudinal and circumferential directions to understand the actual behavior of the pipes under combined bending and tension forces. A series of finite element (FE) analysis was conducted to simulate the behavior of the pipes by utilizing an elastoplastic material model in ABAQUS. The data from DFOS were then used to validate the predicted results from the FE model. The validated FE model can be used for future parametric studies for improved pipe design, if necessary.

2. Test Setup

2.1 Experimental Setup

The experimental setup was developed at the Center for Smart Infrastructure (CSI) of UC Berkeley. The sketch of the entire setup is shown in Figure 2-1. The overview of the actual fully assembled setup of the biaxial tension test is shown in Figure 2-2. Two special jackets were designed and manufactured to hold the pipe ends in place. Two hydraulic actuators with a capacity of 1,500 kips at 24-inch displacement were used for the experiments. One of the actuators was connected to the jacket at the spigot end for tensile force application purposes. The other actuator was used to apply vertical loads. The actuator applied a force on the steel spreader beam, and the beam transferred the force to the bell pipe and spigot via two loading saddles placed on the pipes.

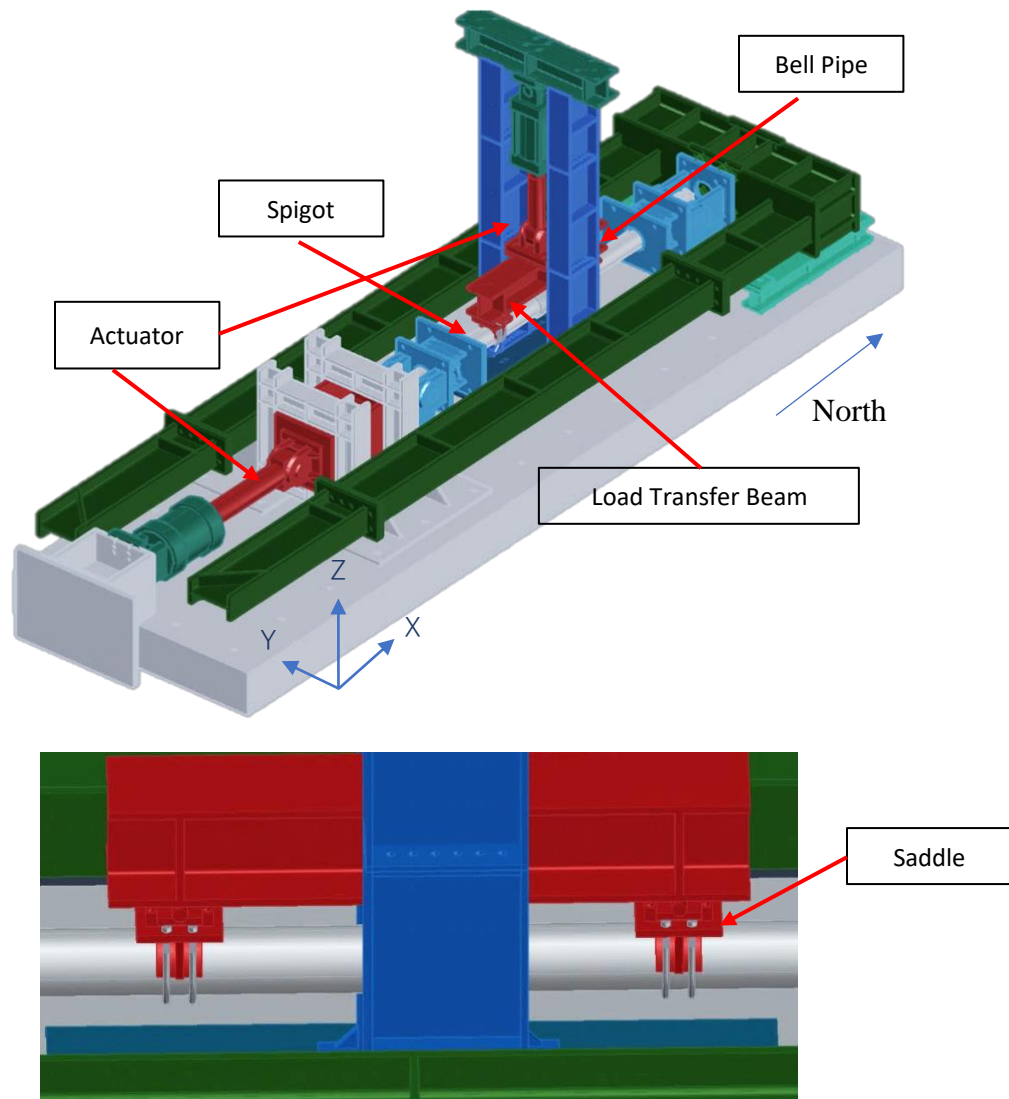


Figure 2-1 Sketch of the experimental setup

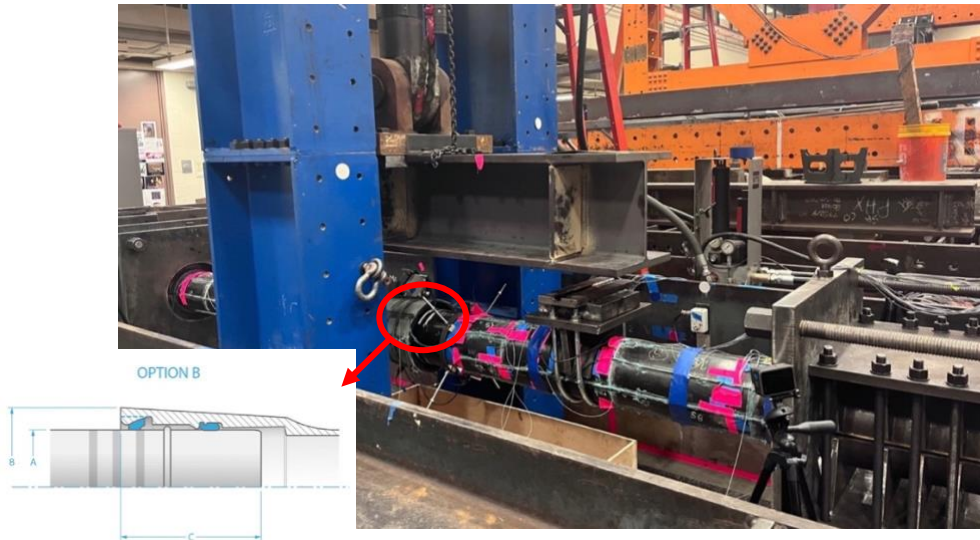


Figure 2-2 Overview of the experimental setup

The 8-inch TR-XTREME™ pipes used in the experiments were manufactured by U.S. Pipe made of ductile iron. Three assembly locations were recommended by the manufacturer, collapsed, midpoint, and extended. The midpoint location (i.e., two white stripes on the spigot are visible) was used as the initial location for the experiments, meaning that the locking segments were not in contact with the weld bead on the spigot, and the spigot was allowed to slide in and out of the bell under vertical loading conditions.

2.2 Specimen List

Two biaxial tension tests were conducted with the same experimental setup but different orientations of the locking segments, as shown in Figure 2-3. For the first test, the single slot was located in the 9 o'clock direction (i.e., at the west side), where the three pieces of the locking segments were placed at the top, east, and bottom sides, respectively. For the second test, the single slot was rotated in the 12 o'clock direction (i.e., at the top side), where the corresponding locking segment locations are west, east, and bottom sides. A rubber gasket was palced at the single slot for both of the specimens. The test log is presented in Table 2-1.

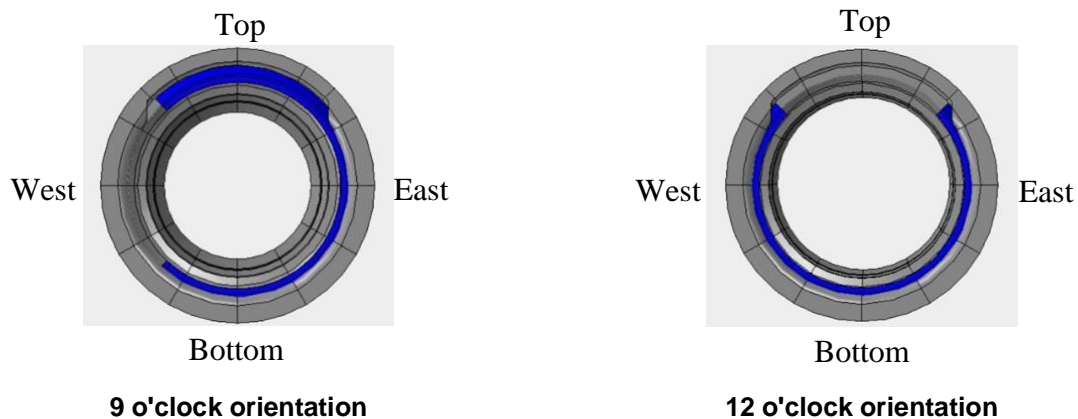


Figure 2-3 Locking segments orientation

Table 2-1 Test log

Test No	Specimen	Test date	Locking segments orientation
1	Specimen 1	9/01/2022	9 o'clock
2	Specimen 2	9/28/2022	12 o'clock

2.3 Test Procedure

The testing procedure included four stages; (i) Self-Weight Moving Down, (ii) Actuator Pushing Down, (iii) Water Pressurization, and (iv) Pull. The loading and boundary conditions varied from each stage. During the first stage (self-weight moving down), the bell-pipe side was restrained only to allow z-direction rotation (i.e., perpendicular to the floor); however, axial movement and z-direction rotation were allowed on the spigot side, meaning that the spigot could slide in and out of the bell. The horizontal actuator was not connected to the hydraulic system, and no external forces were applied during this stage. The bell was moving down due to the self-weight of the pipes, which introduced rotations to the specimen. Once the system achieved static force equilibrium, the actuator was pinned to the hydraulic system to restrain the spigot from further horizontal movement.

Then, a vertical force was applied to further push down the bell until reaching an 8-degrees contraction (4 degrees on both ends). The vertical actuator applied the force to the loading beam, and the loading beam transferred the load to the pipes via the loading saddles. The saddles were placed 33.5 inches away from the mid-point, where the mid-point of the setup was defined to be 3.25 inches away from the bell face. Next, the internal water was pressurized to 50 psi.

Finally, the pipes were pulled until severe pipe damage, and water leakage was observed. The vertical actuator was held to restrain the pipe from moving upward but allowed it to move downward. The minimum contraction of the pipes was 8 degrees throughout this process.

The entire procedure of the testing is summarized in Table 2-2.

Table 2-2 Testing procedure

Test procedure	Loading condition	Boundary condition
Self-weight moving down	Gravity force	Allow z-direction rotation on both ends and x-direction movement on the spigot end.
Actuator pushing down	Vertical actuator force	Allow z-direction rotation on both ends.
Water pressurization	Internal water pressure	Allow z-direction rotation on both ends. Restrain the bell from moving upward.
Pull	Horizontal axial force	Allow z-direction rotation on both ends. Restrain the bell from moving upward.

3. Instrumentation

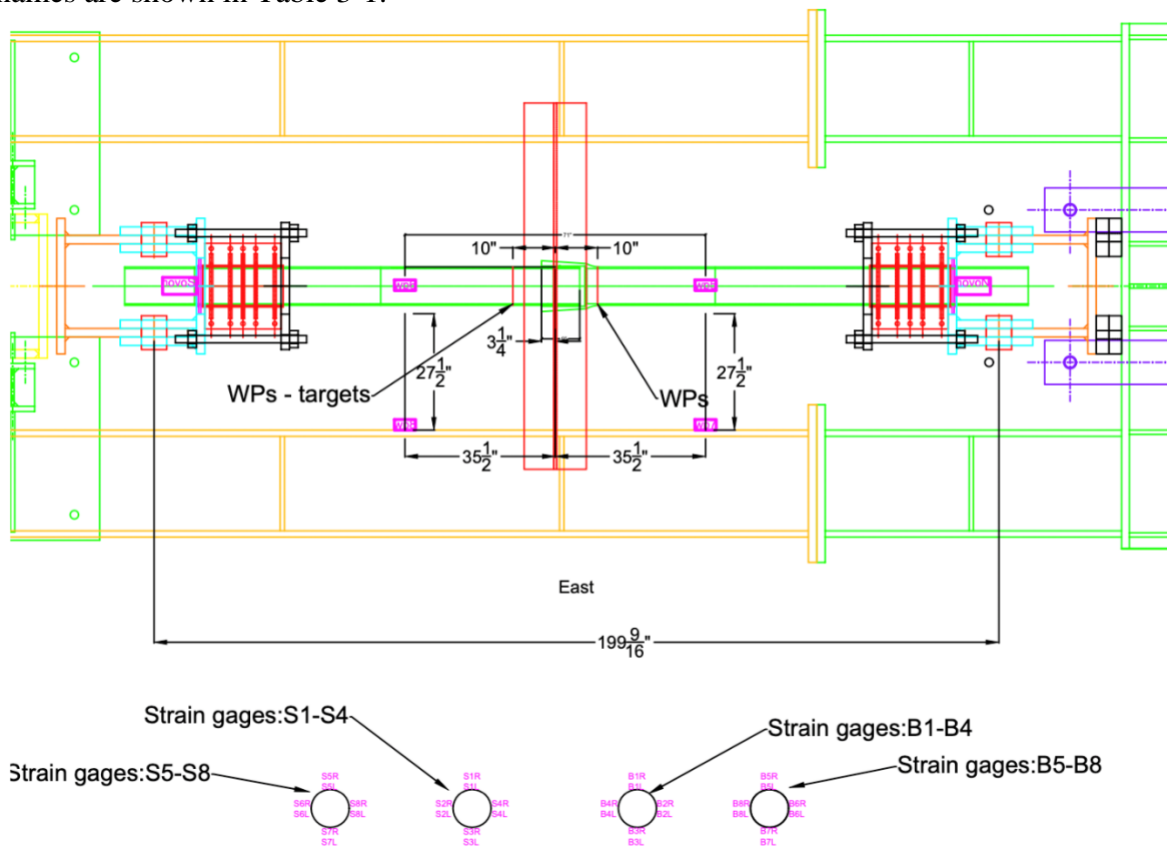
The instrumentation consisted of conventional instruments (strain gauges, string pots) and distributed fiber optic sensors.

3.1 Conventional Instruments

Four strain gauges plane were used; two on the bell pipe and another two on the spigot. Each strain gauge plane consisted of four strain gauge sets. Strain gauge sets were placed at the position of the top, west, bottom, and east sides (i.e., 12, 3, 6, 9 o'clock) on the bell pipe and spigot. Each set of strain gauges included two strain gauges in the perpendicular directions measuring axial and circumferential strains.

Four wire pots were placed on the bell pipe at 45 degrees apart from the quarter points around the circumference and were fixed to the spigot to measure the joint opening. Another four wire pots were used to measure the pipe displacement during the experiment. They were individually mounted to the bell pipe and spigot on the east and bottom sides. The wire pots installed on the bottom sides were used to monitor the vertical displacement, and the ones on the east side aimed to measure the horizontal movement.

The locations of the instruments are shown in Figure 3-1, and the local instrumentation names are shown in Table 3-1.



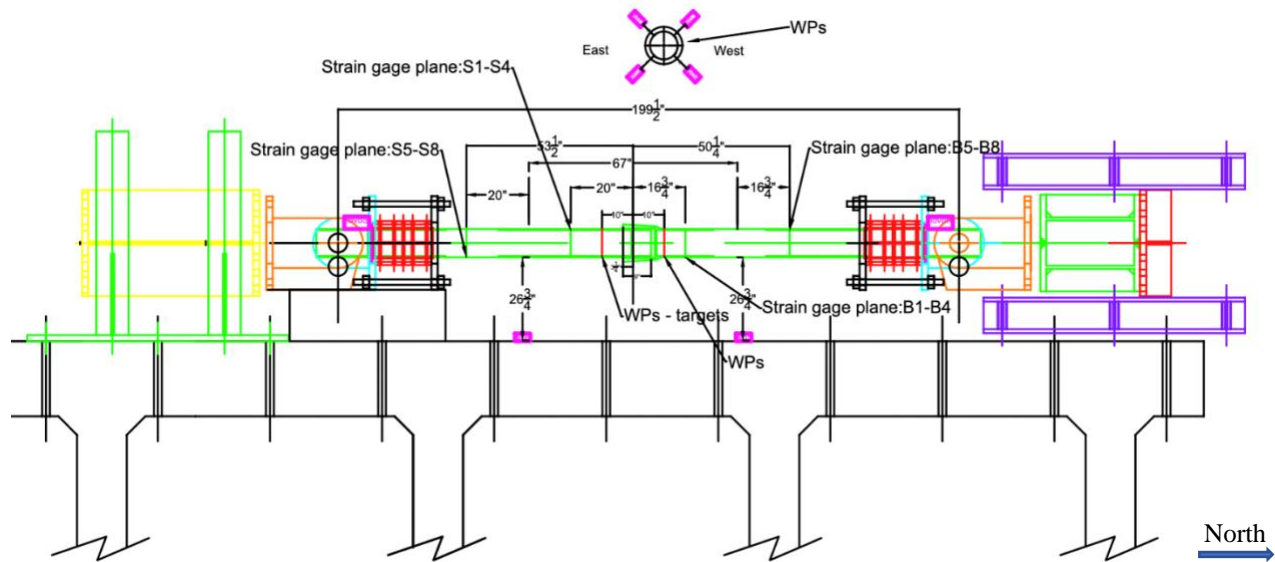


Figure 3-1 Instrumentation plan of conventional instruments

Table 3-1 Conventional instrumentation local names

Instrument	Location	Local Instrument Name
String Pot	Parallel to Axial Direction, North of Bell, Top-west	wp1
	Parallel to Axial Direction, North of Bell, West-bottom	wp4
	Parallel to Axial Direction, North of Bell, Bottom-east	wp2
	Parallel to Axial Direction, North of Bell, East-top	wp3
	Perpendicular to Axial Direction, North of Bell, Bottom	wp5
	Perpendicular to Axial Direction, North of Bell, East	wp7
	Perpendicular to Axial Direction, South of Bell, Bottom	wp6
	Perpendicular to Axial Direction, South of Bell, East	wp8
Strain Gauge	Top of Bell-side Pipe (North), Axial Strain	B5L
	West of Bell-side Pipe (North), Axial Strain	B8L
	Bottom of Bell-side Pipe (North), Axial Strain	B7L
	East of Bell-side Pipe (North), Axial Strain	B6L
	Top of Spigot (North), Axial Strain	S1L
	East of Spigot (North), Axial Strain	S2L
	Bottom of Spigot (North), Axial Strain	S3L
	West of Spigot (North), Axial Strain	S4L
	Top of Bell-side Pipe (North), Circumferential Strain	B5R
	West of Bell-side Pipe (North), Circumferential Strain	B8R
	Bottom of Bell-side Pipe (North), Circumferential Strain	B7R
	East of Bell-side Pipe (North), Circumferential Strain	B6R
	Top of Spigot (North), Circumferential Strain	S1R
	East of Spigot (North), Circumferential Strain	S2R
	Bottom of Spigot (North), Circumferential Strain	S3R
	West of Spigot (North), Circumferential Strain	S4R
	Top of Bell-side Pipe (South), Axial Strain	B1L
West of Bell-side Pipe (South), Axial Strain	B2L	
Bottom of Bell-side Pipe (South), Axial Strain	B3L	

	East of Bell-side Pipe (South), Axial Strain	B4L
	Top of Spigot (South), Axial Strain	S5L
	East of Spigot (South), Axial Strain	S6L
	Bottom of Spigot (South), Axial Strain	S7L
	West of Spigot (South), Axial Strain	S8L
	Top of Bell-side Pipe (South), Circumferential Strain	B1R
	West of Bell-side Pipe (South), Circumferential Strain	B2R
	Bottom of Bell-side Pipe (South), Circumferential Strain	B3R
	East of Bell-side Pipe (South), Circumferential Strain	B4R
	Top of Spigot (South), Circumferential Strain	S5R
	East of Spigot (South), Circumferential Strain	S6R
	Bottom of Spigot (South), Circumferential Strain	S7R
	West of Spigot (South), Circumferential Strain	S8R

3.2 Distributed Fiber Optic Sensors

Two types of fiber optic cables manufactured by NanZee Sensing Technology Co. were used; (a) 5 mm diameter armored cable (NanZee 5mm) and (b) 0.9 mm diameter cable (NanZee 0.9mm). The local instrument names are listed in Table 3-2 and the layouts of the cables are shown in Figure 3-2. 3M SCOTCH-WELD DP8010 epoxy was used to attach the cables to the pipes.

NanZee 5mm cables (blue lines) were used in the longitudinal direction to mimic the use at construction sites. They were attached on both pipes, 45 degrees apart, numbered S9-S25. Though most longitudinal cables start and end at similar locations, some variations are due to the experimental setup's conflicts.

To better understand the deformation mechanism of the pipes and bell section, NanZee 0.9mm (red lines) were used for measuring circumferential strains, numbered S1-S9. Three circumferential sensors with about 18-inch spacing were installed on both pipes. In addition, another three circumferential sensors were attached to the bell, end, and middle of the section, and the location on top of the locking segments (i.e., about 3.5 inches from the bell face).

A Rayleigh-based optical frequency domain reflectometry (OFDR), Luna ODiSI 6100 series, was used in this experiment for data acquisition. The analyzer is capable of measuring up to 50m long fiber optic cable with an accuracy of less than ± 1 micro strain when taking a measurement every 0.65mm. More detail about the cables and analyzer can be found in Appendix A.

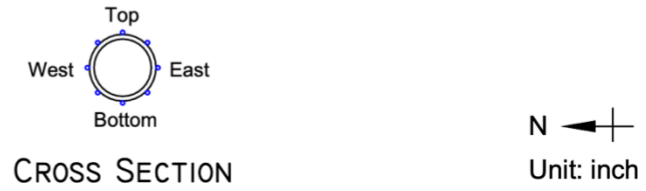
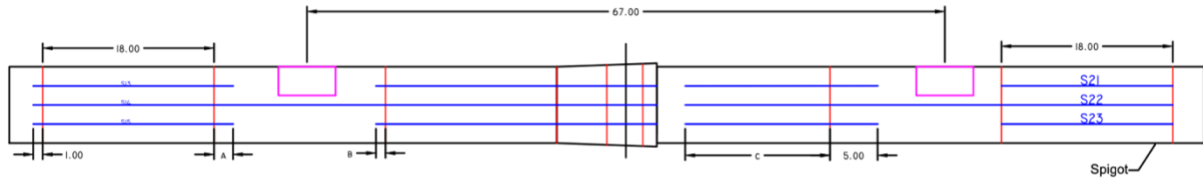
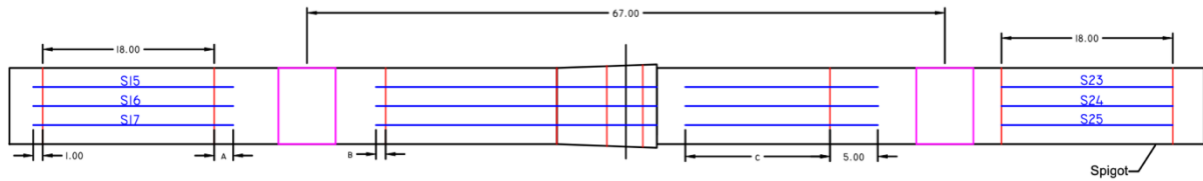
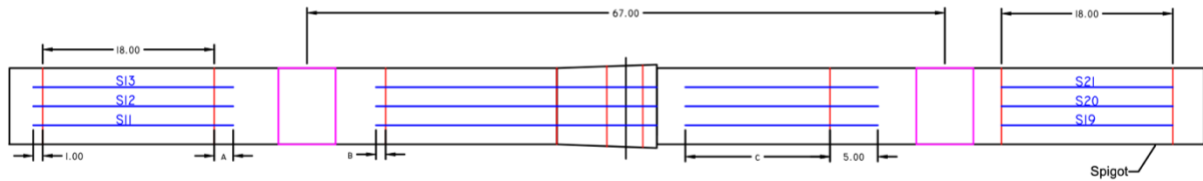
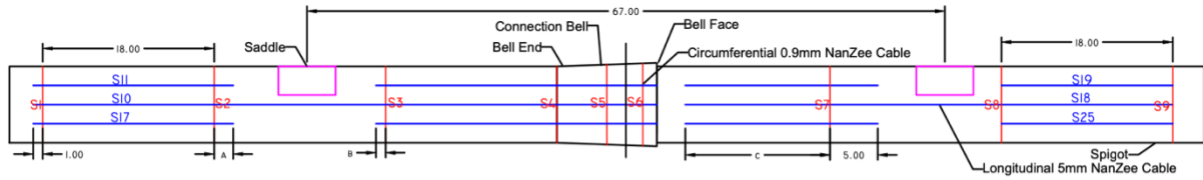


Figure 3-2 DFOS instrumentation plan

Table 3-2 DFOS local names

Instrument	Location	Local Instrument Name
DFOS	64.5 inches north of bell face, Circumferential	S1
	46.5 inches north of bell face, Circumferential	S2
	28.5 inches north of bell face, Circumferential	S3
	Bell end, Circumferential	S4
	Mid location of bell, Circumferential	S5
	3.5 inches north of bell face, Circumferential	S6
	18 inches south of bell face, Circumferential	S7
	36 inches south of bell face, Circumferential	S8
	5 inches south of bell face, Circumferential	S9
	Bell pipe, West, Longitudinal	S10
	Bell pipe, West-top, Longitudinal	S11
	Bell pipe, Top, Longitudinal	S12
	Bell pipe, Top-east, Longitudinal	S13
	Bell pipe, East, Longitudinal	S14
	Bell pipe, East-bottom, Longitudinal	S15
	Bell pipe, Bottom, Longitudinal	S16
	Bell pipe, Bottom-west, Longitudinal	S17
	Spigot, West, Longitudinal	S18
	Spigot, West-top, Longitudinal	S19
	Spigot, Top, Longitudinal	S20
	Spigot, Top-east, Longitudinal	S21
	Spigot, East, Longitudinal	S22
	Spigot, East-bottom, Longitudinal	S23
	Spigot, Bottom, Longitudinal	S24
	Spigot, Bottom-west, Longitudinal	S25

Table 3-3 Location of longitudinal fiber optic cables

Sensor	Test 1			Test 2		
	A	B	C	A	B	C
S11	2"	0"	10"	2"	1"	5"
S12	2"	1"	10"	2"	1"	5"
S13	2"	1"	10"	2"	1"	5"
S15	2"	1"	10"	2"	1"	5"
S16	0"	1"	10"	2"	1"	5"
S17	4"	1"	10"	2"	1"	5"
S19	2"	1"	10"	2"	1"	5"
S20	2"	1"	10"	2"	1"	5"
S21	2"	1"	10"	2"	1"	5"
S23	2"	1"	10"	2"	1"	5"
S24	2"	1"	10"	2"	1"	5"
S25	2"	1"	10"	2"	1"	5"

4. Test Results

All test results are discussed in this section. In addition, a summary of the observed failure mode and the performance of the 8 inches U.S. Pipe TR-XTREME™ joint under combined bending and tensile force is described.

4.1 Calculation Approach

The approaches to calculating the rotation and moment are discussed herein. The pipes are assumed to be rigid bodies, and the rotations of the pipes are calculated using equations (1) – (3). The vertical displacements of the pipes were measured by the vertical wire pots (VWP) located beneath the pipes. θ_{Bell} and θ_{Spigot} are the rotations of the bell pipe and the spigot, respectively. The overall rotation, θ_{Total} , of the joint is defined as the sum of the two side angles.

$$\theta_{Bell} = \tan^{-1}\left(\frac{\text{vertical displacement of bell pipe}}{\text{distance between VWP and the end support}}\right) \quad (1)$$

$$\theta_{Spigot} = \tan^{-1}\left(\frac{\text{vertical displacement of spigot}}{\text{distance between VWP and the end support}}\right) \quad (2)$$

$$\theta_{Total} = \theta_{Bell} + \theta_{Spigot} \quad (3)$$

The system is considered to be a simple-supported beam. The self-weight, including the pipe's and water's weight, is assumed to be evenly distributed, and hence the moment introduced by self-weight is calculated based on equation (4), where w is the uniform load due to the self-weight, and l is the length of the pipe. The additional moment applied to the central portion of the pipe is calculated using equation (5), where P is the actuator load, and L is the distance between the support and the loading location.

$$M_{distrib} = \frac{wl^2}{8} \quad (4)$$

$$M_{central} = \frac{PL}{2} \quad (5)$$

4.2 Experimental Data Analysis

As mentioned in Chapter 2, four stages (self-weight moving down, actuator pushing down, water pressurization, and pull) were conducted for the two biaxial tension tests. This section discusses the performance of the pipes under different loading and boundary conditions using experimental data.

4.2.1 Moment and Rotation

The measured moment-rotation relationships of the two specimens are shown in Figure 4-1. The pipes were first moving downward due to the gravity forces. The equilibrium point was achieved when the specimens reached about 3.58-degree and 3.94-degree deflection contraction, respectively, with a moment of about 22.4 kip-in.

Next, a vertical force was applied to push the pipe down until reaching a total rotation of 8.36 degrees. The specimens reached the targeted deflection contraction with moments of about 1042.3 kip-in and 880.3 kip-in, respectively.

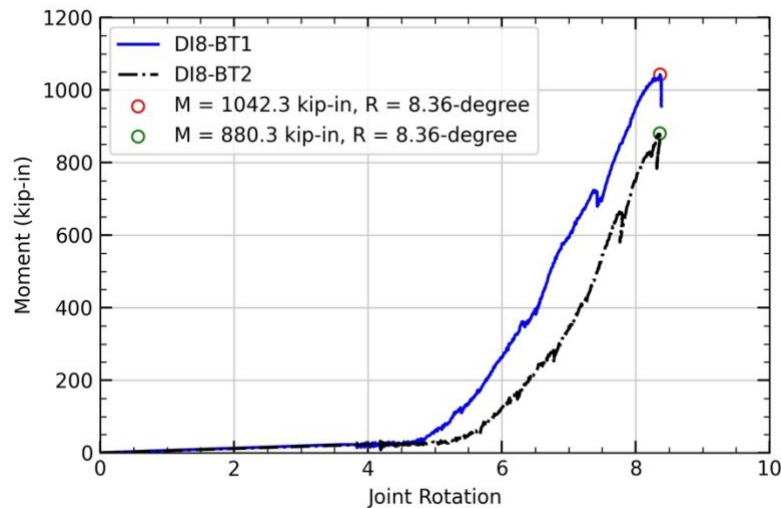


Figure 4-1 Moment vs. Rotation

As shown in Figure 4-1, Specimen 1 constantly requires a larger moment to achieve the desired rotation, due to the difference in the locking segments' orientations. For Specimen 1, the spigot needs to overcome the locking segment located on the top while deflecting relatively to the bell in the joint to achieve the given deflection angle. Instead of having a locking segment at the top side (12 o'clock) location, Specimen 2 has a rubber gasket to seal the single slot, which allows a larger displacement. Therefore, Specimen 2 tends to have a larger deflection with a similar applied moment. In addition, while comparing the stress developed at the bottom edge of the spigot (highlighted in purple), the concentrated stresses are higher than that from Specimen 2. The mechanism is shown in Figure 4-2.

After the specimens reached an 8.36-degree rotation, a monotonic axial force was applied to the specimen. During this stage, the vertical actuator remained in place to force the pipes to maintain an 8.36-degree rotation while being pulled.

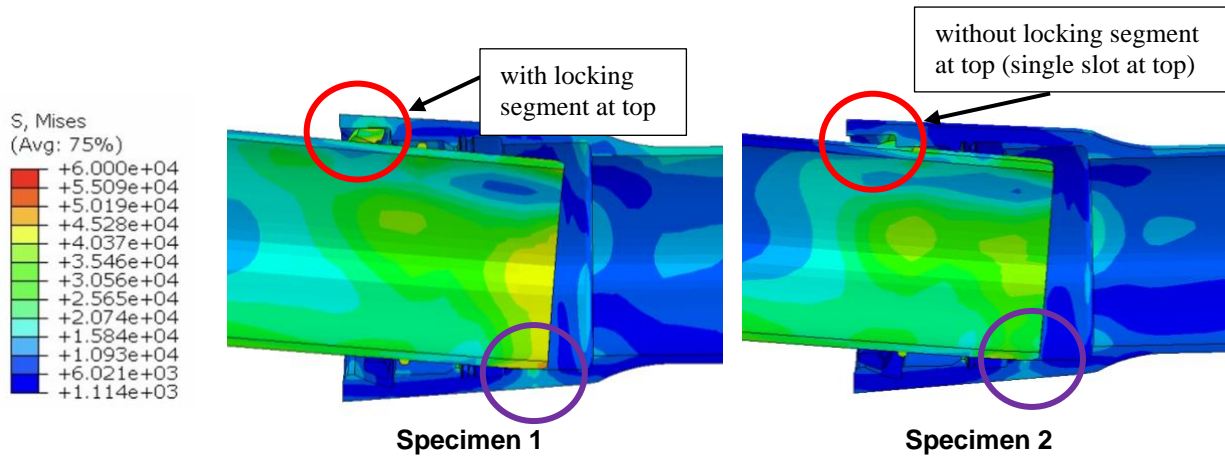


Figure 4-2 Sketch of the bell after Push Down stage

4.2.2 Axial Force and Joint Opening

Specimens were pulled with a minimum 8.36-degree deflection contraction until a severe failure occurred. Figure 4-3 shows the load and joint opening curve of the specimens. The peak values are about 171 kips and 145 kips, individually. The average joint opening at maximum force is about 2.3 inches (Specimen 1) and 2 inches (Specimen 2). The difference is again due to the locking segment’s orientations.

Figure 4-4 demonstrates the stress distribution of the bell after being pulled. As shown in the plots, the stress distributions and the deformation of the bell varies. While being pulled, frictions were developed between the spigot and the locking segments located at 3, 9, and 12 o’clock (west, east, top) sides. Since the pipes were bent, the locking segment located at the bottom side (6 o’clock) was not well-contacted with the spigot, resulting in a smaller frictional force (i.e., smaller stress was developed at the bottom side). Due to the locking segment located at the top position of Specimen 1 but not of Specimen 2, the frictional force that Specimen 1 was overcoming was greater than that of Specimen 2. Besides, the deformed shapes of the bell of the two specimens are different. A symmetric deformation can be observed in Specimen 2. Because of the different force transfer and deformation mechanisms, the ultimate capacities vary between the specimens.

The results of the two tests are summarized in Table 4-1.

Table 4-1 Summary of the tests

	Locking Segments Orientation	Max. Axial load (kips)	Max. Ave. Joint Opening (in.)	Total Rotation (degree)
Specimen 1	9 o'clock	171	2	8.36
Specimen 2	12 o'clock	145	2.3	8.36

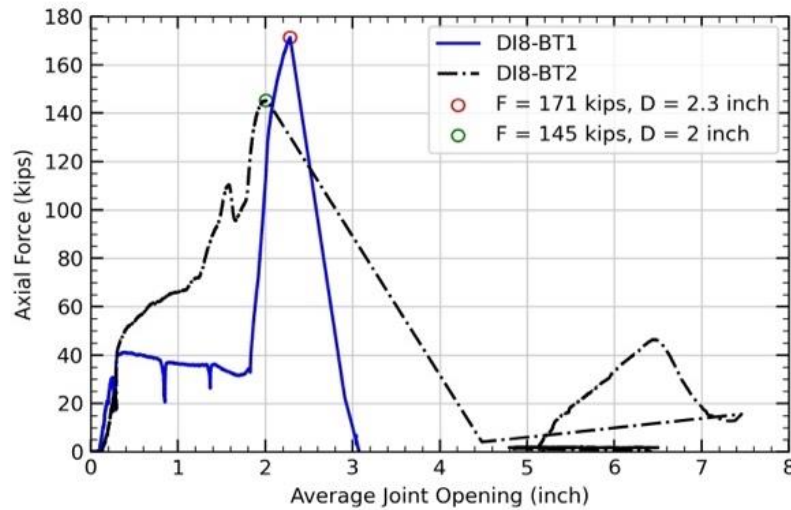


Figure 4-3 Axial force vs. average joint opening

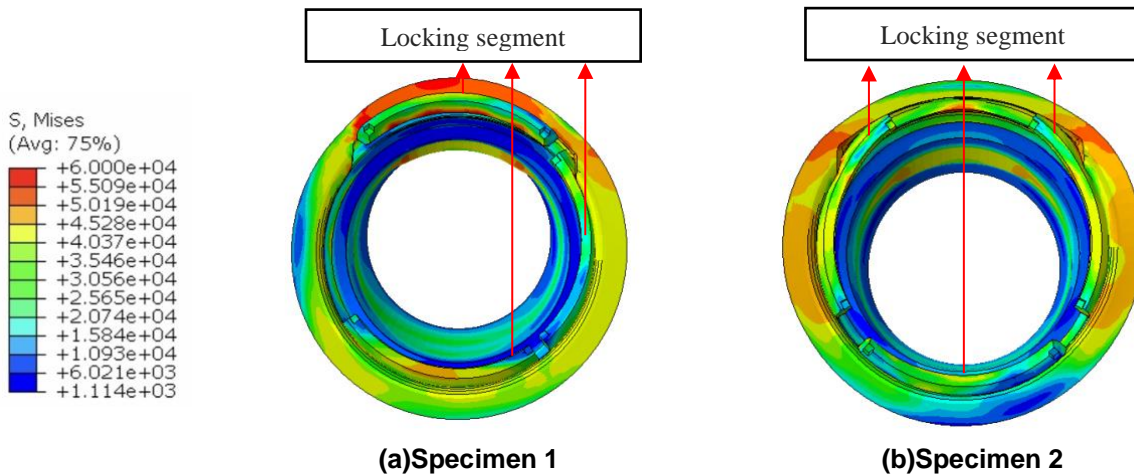


Figure 4-4 Stress distribution of the cross-section of the bell under the Pull stage

4.2.3 Axial Strain

General

The axial strain results measured by the strain gauges are shown in Figure 4-5 and Figure 4-6 for the two specimens, respectively. Looking at the Self-Weight Moving Down and Actuator Pushing Down stages, one can observe a clear pattern: the top side (12 o'clock) is generally under compression due to bending, and the bottom side (6 o'clock) is mainly under tension from both of the specimens. However, the magnitude of the strains of the east side (3 o'clock) and west side (9 o'clock) differ between the specimens. This is because Specimen 1 has a non-symmetric configuration of the locking segments (i.e., locking segments were placed on the west side but not on the east side). Since the locking segment provides a better constraint than the rubber gasket, the pipe tends to move out more on the rubber gasket side, resulting in a bending moment. Hence, for Specimen 1, tensile strains were developed at the west side (9 o'clock), and compressive strains were developed at the east side (3 o'clock).

On the contrary, since the locking segments were placed at both the east and west sides of Specimen 2, the above-mentioned phenomenon is not observed. Theoretically, the axial strains at the east side (3 o'clock) and west side (9 o'clock) of Specimen 2 would be close to zero. However, the strain gauges might not be located exactly at the east and west locations due to installation errors, resulting in non-zero strains on both sides. During the Pull stage, tensile strains were developing in both specimens' directions.

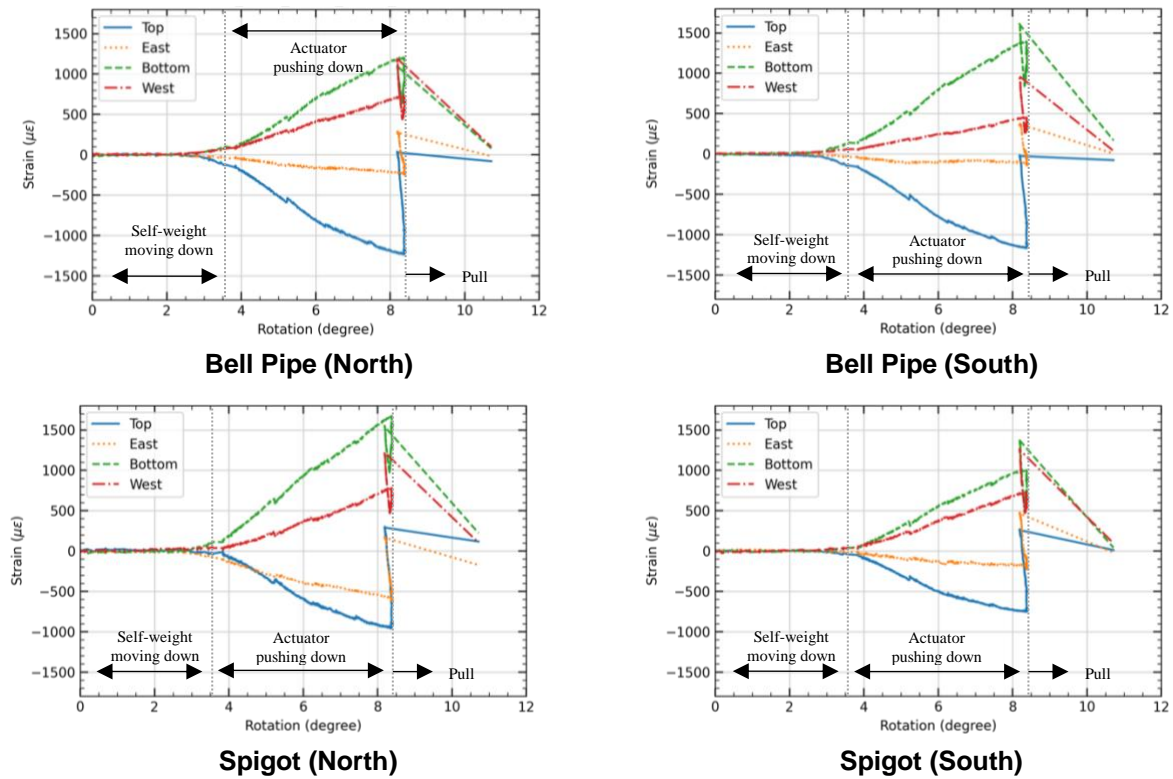


Figure 4-5 Axial strain vs. rotation of Specimen 1

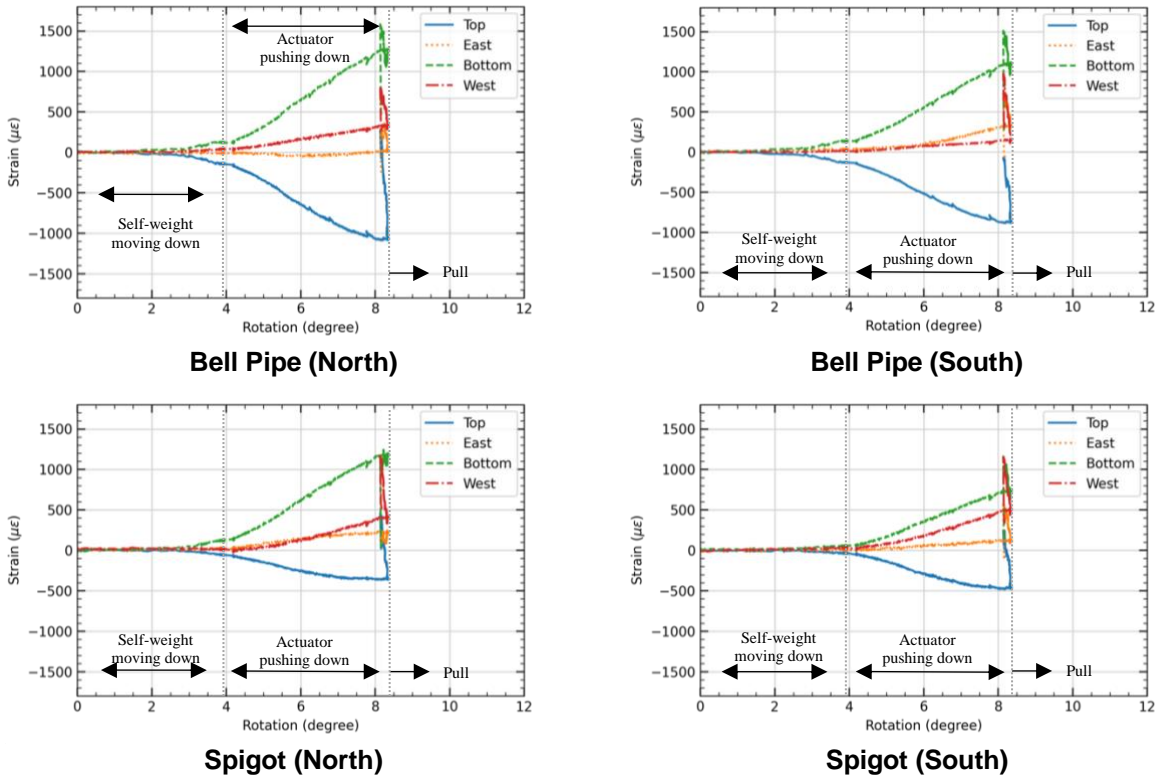


Figure 4-6 Axial strain vs. rotation of Specimen 2

Bending stage

Figure 4-7 and Figure 4-8 show the axial strain distribution when the pipe first achieved the targeted deflection contraction (i.e., 8.36-degree rotation, which occurred at the end of the Actuator Pushing Down stage) measured by the fiber optic sensors placed on specimens. The strain gauge data are also plotted to show the two data sets are compatible with each other. All the strain distribution of the sensors is plotted from the north to the south. Due to experimental setup conflict, the fiber optic cables were not attached to the locations where the saddles were placed, resulting in missing values in the middle section of the plots. Since the pipes are being pushed down, most of the sections of the pipes on the top side (12 o'clock) are under compression. However, smaller compressive strains close to the saddle can be found on the top side (12 o'clock). The saddles are transferring a large force pointing downward to the pipe, and due to the Poisson's effect, tensile strains in the axial direction are developing. Hence, the strains close to the saddle are the combination of strains introduced by both bending and Poisson's effect.

At this stage, the specimen can be treated as experiencing pure bending forces. Hence, the axial strains at the west side (9 o'clock) remain small and close to zero. The slight difference between the strain gauges and fiber optic sensor results are due to the offset between each other.

More fiber optic sensor results can be found in Appendix B.

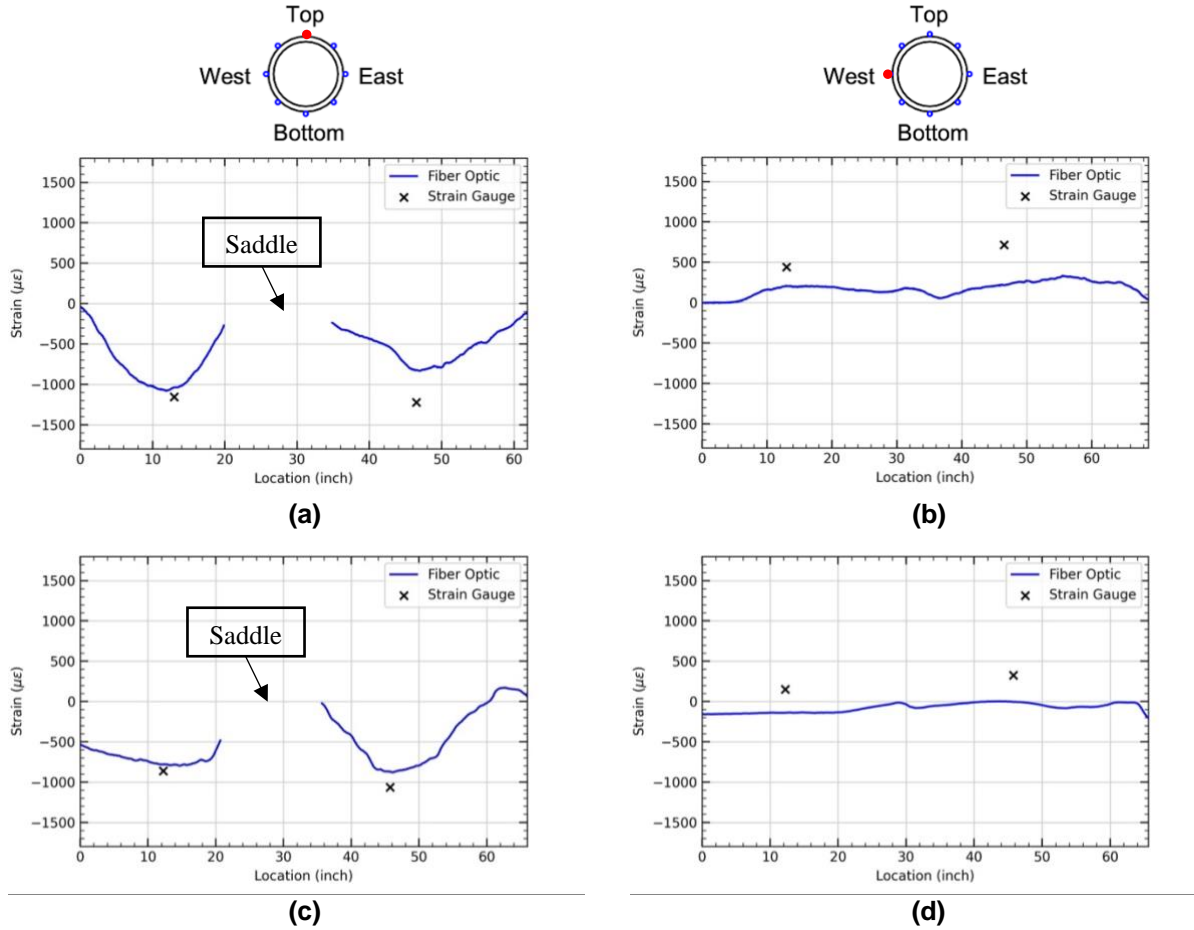
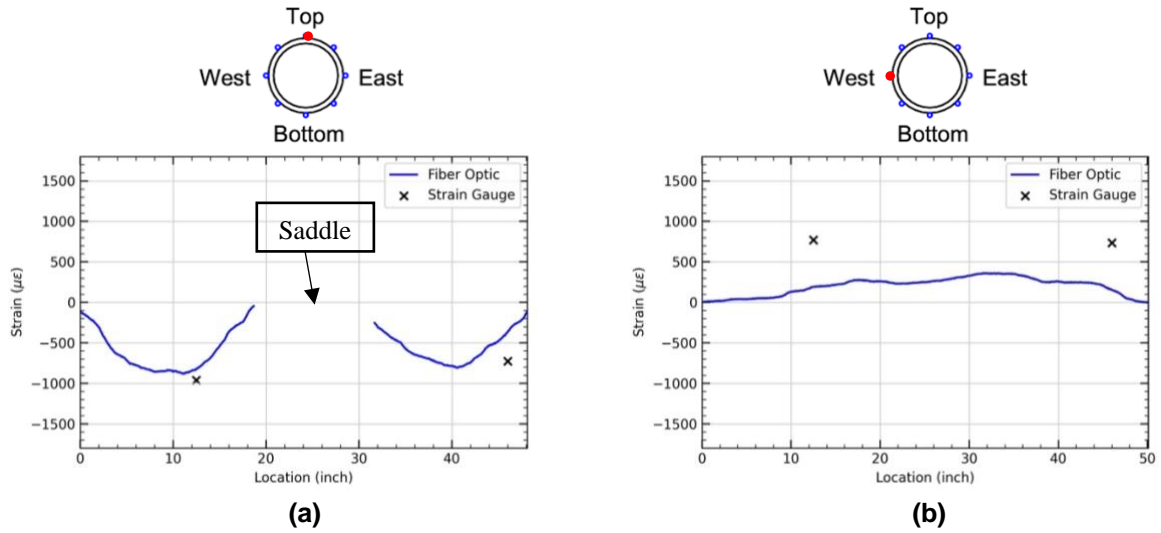


Figure 4-7 Strain development of bell pipe in the longitudinal direction under 8.36-degree rotation. (a) Top side of Specimen 1, (b) West side of Specimen 1, (c) Top side of Specimen 2, (d) West side of Specimen 2



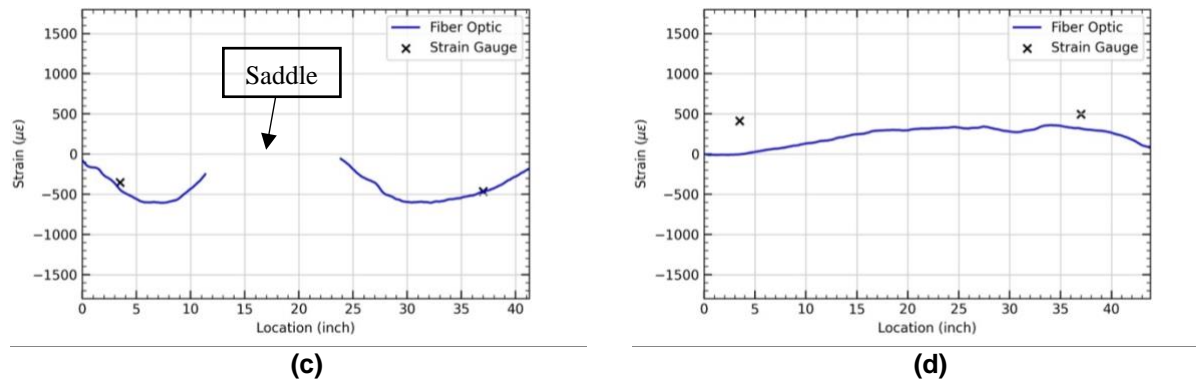


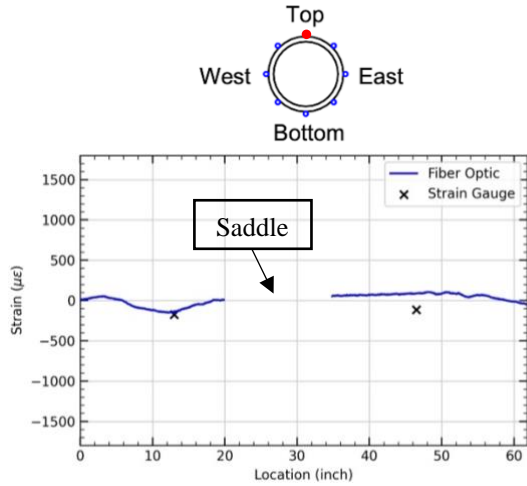
Figure 4-8 Strain development of spigot in the longitudinal direction under 8.36-degree rotation condition. (a) Top side of Specimen 1, (b) West side of Specimen 1, (c) Top side of Specimen 2, (d) West side of Specimen 2

Pulling stage

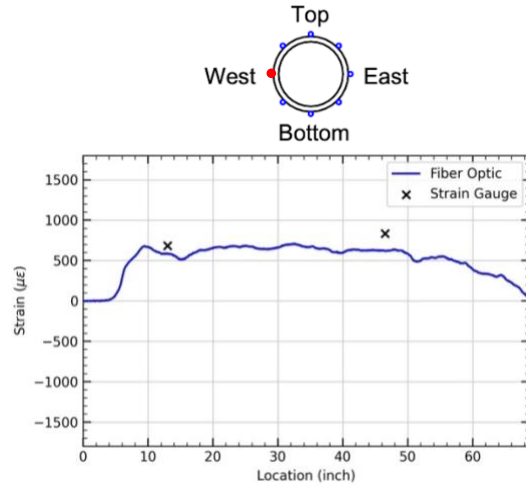
Figure 4-9 and Figure 4-10 show the strain distribution results at the Pull stage with 140 kips axial force. A different pattern can be observed from the bell pipe of the two specimens. Take the results from the west side (9 o'clock), for example. Most of the sections are under tension because of the axial force. However, a large compression section close to the locking segment can be found in Specimen 2. A moment was introduced on the surface as the bell expanded. At the same time, the locking segments were being pulled out, resulting in a significant compression strain on the surface near the locking segment. Since no locking segment was placed at the west side (9 o'clock) of Specimen 1, the sensor did not capture the phenomenon observed in Specimen 2.

Looking at the results from the top side (12 o'clock) of Specimen 2, one can observe a larger tensile strain close to the bell. This might be the reason that as the locking segments on the sides (3 and 9 o'clock) were pulled out, the thickness of the bell on the top decreased, resulting in a larger tensile strain close to the bell section. A detailed discussion can be found in Section 5.

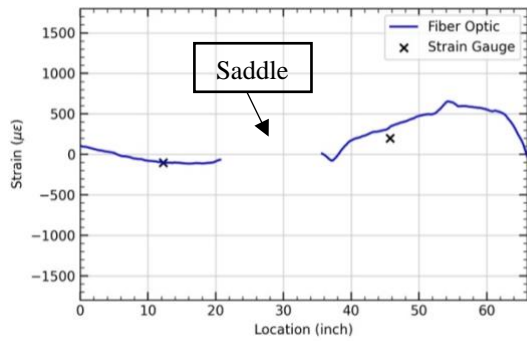
The spigot's strain distribution is similar between the two specimens. Since the specimens were bent to the desired deflection angle, the top sides of the specimens were under compression, and the bottom side was under tension. During the pulling stage, although tensile strains were developed at all the faces, the ultimate tensile strains at the top side were the smallest, and those at the bottom side were the largest. The axial strain results of the top and west sides of the two specimens are shown in Figure 4-9 and Figure 4-10 (c)-(d). All the axial strain results measured by fiber optic sensors are listed in Appendix B.



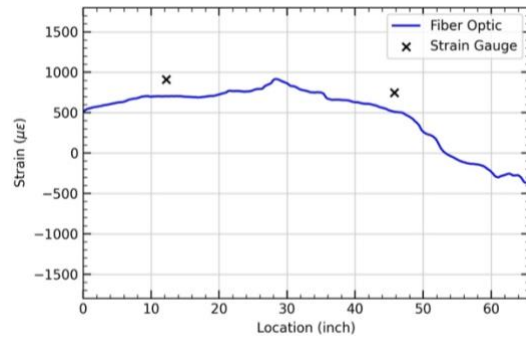
(a)



(b)

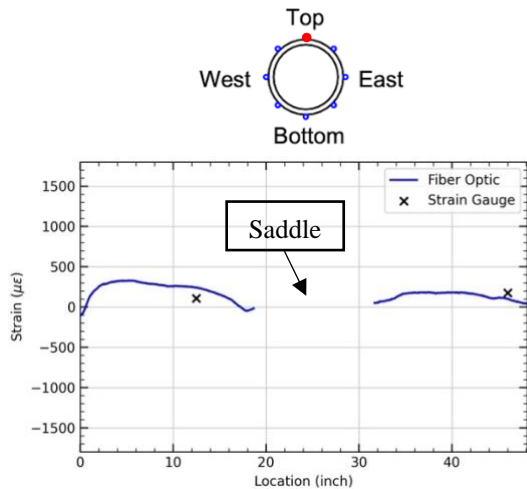


(c)

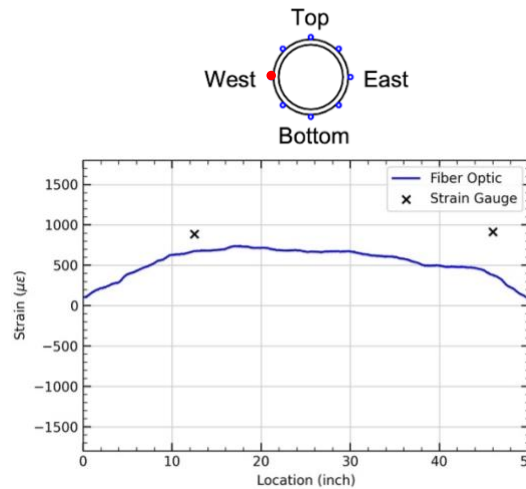


(d)

Figure 4-9 Strain development of bell pipe in longitudinal direction under 140 kips axial force loading condition. (a) Top side of Specimen 1, (b) West side of Specimen 1, (c) Top side of Specimen 2, (d) West side of Specimen 2



(a)



(b)

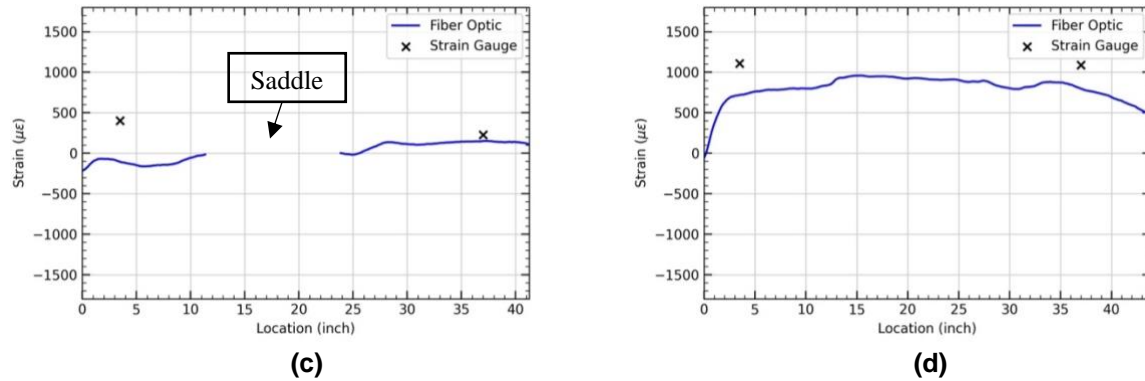


Figure 4-10 Strain development of spigot in longitudinal direction under 140 kips axial force loading condition. (a) Top side of Specimen 1, (b) West side of Specimen 1, (c) Top side of Specimen 2, (d) West side of Specimen 2

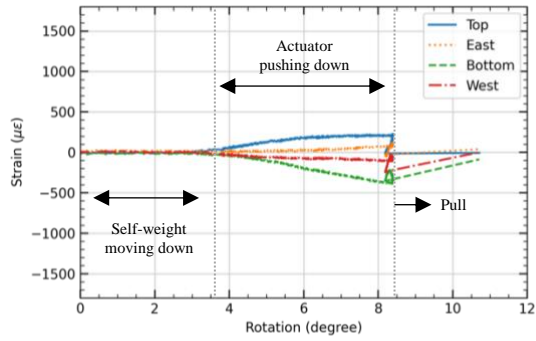
4.2.4 Hoop Strain

General

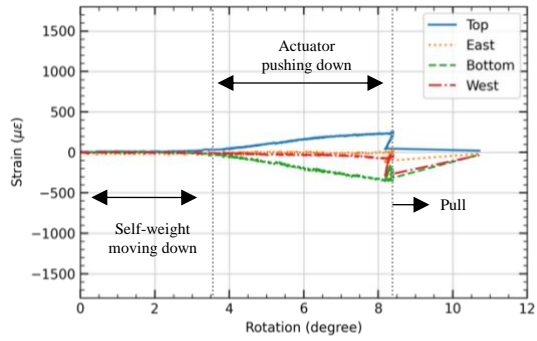
The relationships between the hoop strains, measured by strain gauges with total rotation, are plotted in Figure 4-11 and Figure 4-12 for Specimens 1 and 2, respectively. The Actuator Pushing Down stage is close to pure bending conditions; hence, compressive axial strain can be found at the top side (12 o'clock), and tensile axial strain can be observed at the bottom side (6 o'clock), as discussed in the previous section. Due to Poisson's effect, the strains in the circumferential direction are mainly opposite to those in the longitudinal direction. Tensile hoop strains can be observed at the top side (12 o'clock), and compressive hoop strains occur at the bottom side (6 o'clock). The strains at the west and east (3 and 9 o'clock) sides are generally small and close to zero.

During the Pull stage, the mechanism of the pipes is similar to the previous stage, meaning that expansion can be found on the top side, compression is observed at the bottom side, and small deformation develops at the other two sides. However, the mechanism of the bell differs between the two locking segment orientations. As the locking segments tend to be pulled out, the bell tends to shrink on the location where the single slot locates and expand on the other sides to allow the locking segments to come out.

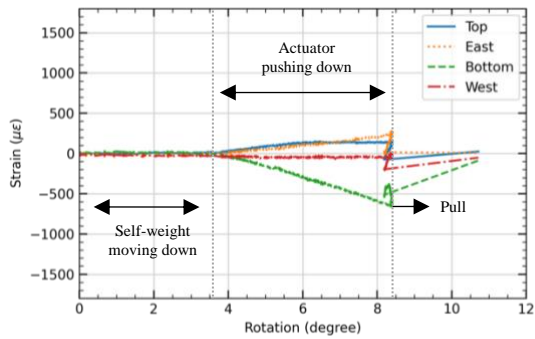
The detailed mechanism of the pipe deformation will be discussed using the fiber-optic sensing results in the following sections regarding each stage.



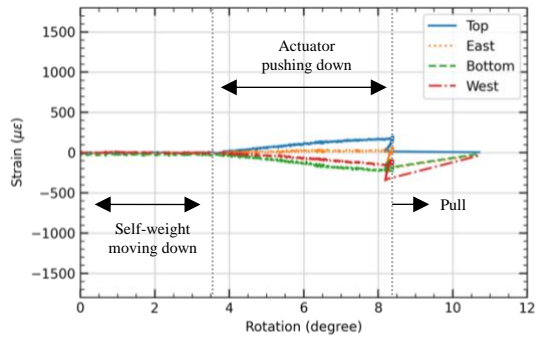
Bell Pipe (North)



Bell Pipe (South)

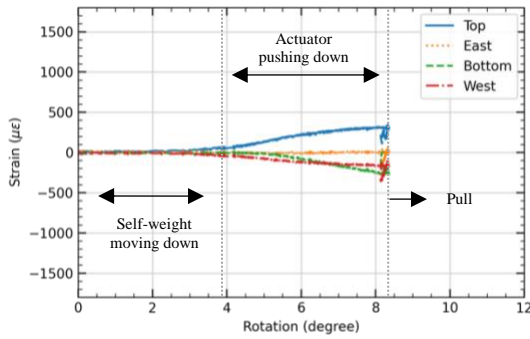


Spigot (North)

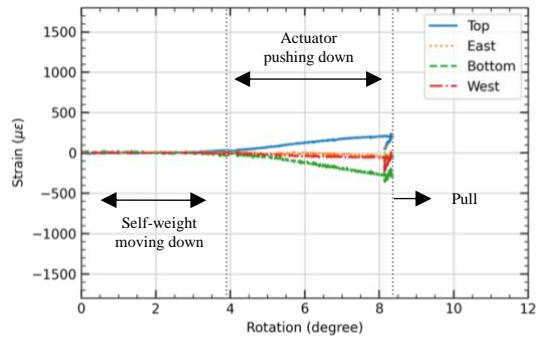


Spigot (South)

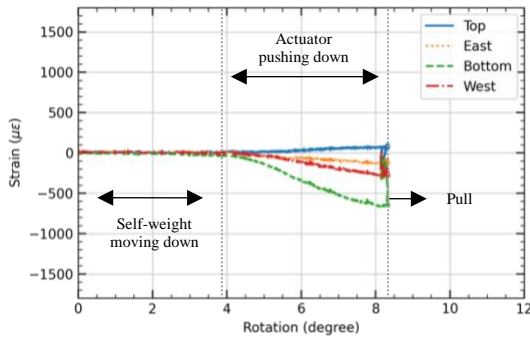
Figure 4-11 Hoop strain vs. rotation of Specimen 1



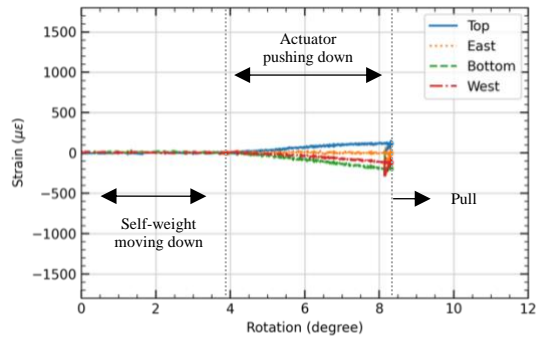
Bell Pipe (North)



Bell Pipe (South)



Spigot (North)



Spigot (South)

Figure 4-12 Hoop strain vs. the rotation of Specimen 2

Bending stage

The fiber optic results of the hoop strains close to the connection bell sections when the pipe first achieved the targeted deflection contraction (i.e., 8.36-degree rotation, which occurred at the end of the Actuator Pushing Down stage) in Specimen 1 are plotted in Figure 4-13.

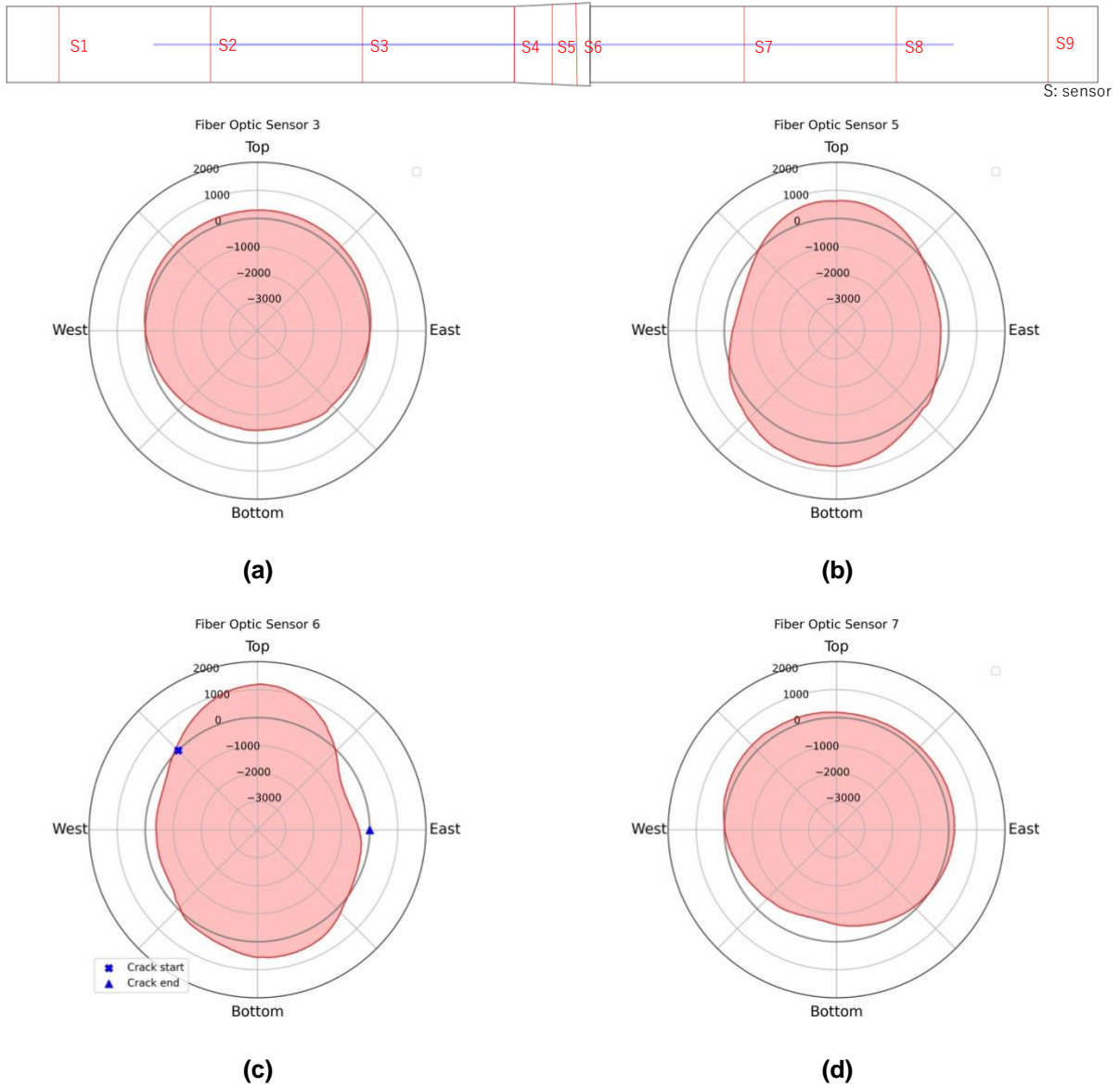


Figure 4-13 Strain distribution in the circumferential direction of Specimen 1 under 8.3-degree rotation condition. (a) sensor on the bell pipe (b) sensor at the mid location of the bell (c) sensor on top of the locking segments on the bell (d) sensor on the spigot

During the bending stage, the strain distribution pattern of the two specimens is similar. Tensile hoop strains are observed on the top side (12 o'clock) and compressive strains on the bottom (6 o'clock) of the pipes, which indicates that the pipes are squashing, as shown in Figure 4-13(a and d) and Figure 4-14(a and d).

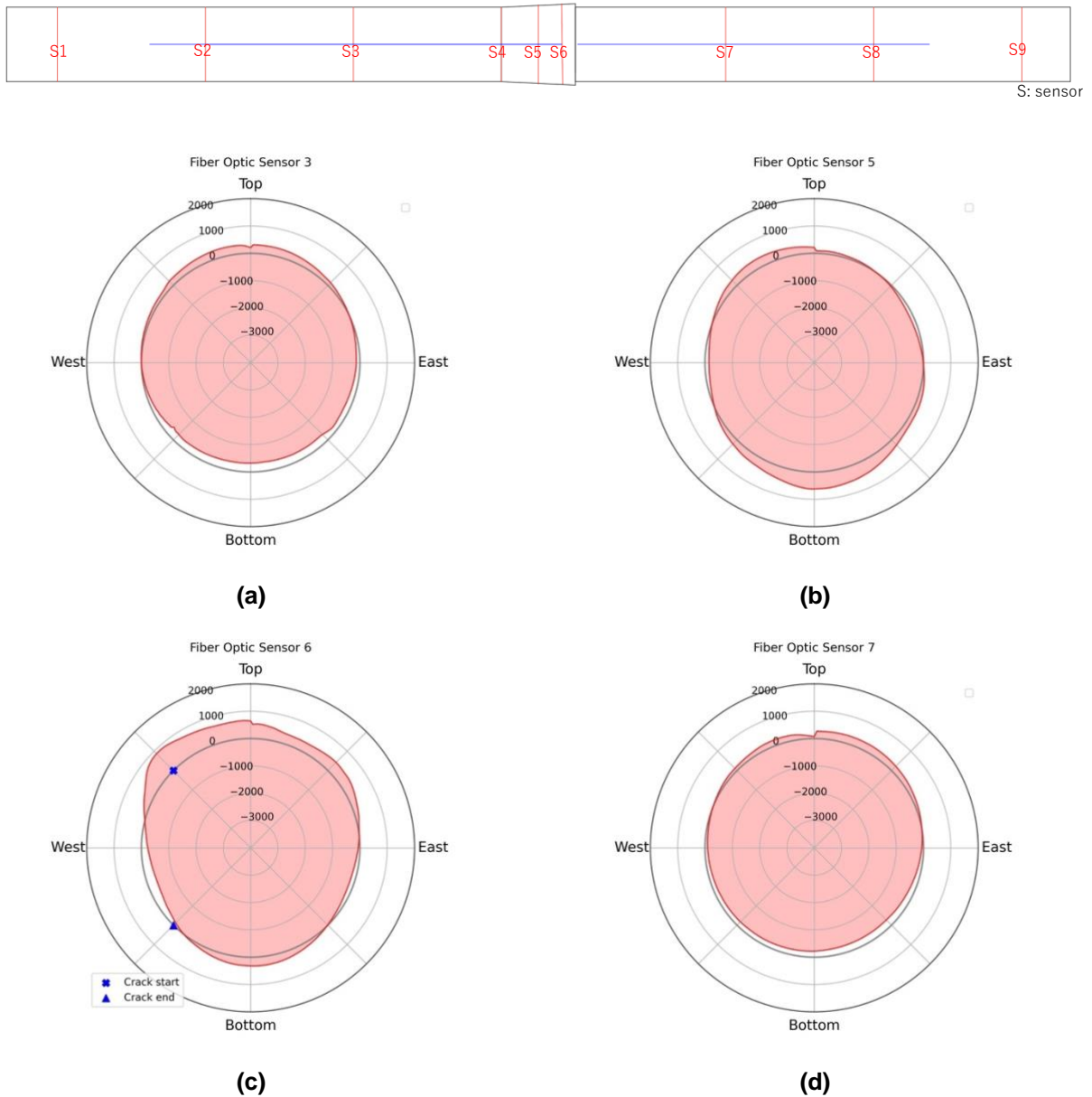


Figure 4-14 Strain distribution in circumferential direction under Specimen 2 under 8.3-degree rotation condition. (a) sensor on the bell pipe (b) sensor at the mid location of the bell (c) sensor on top of the locking segments on the bell (d) sensor on the spigot

On the other hand, the bells were expanding on the top and bottom sides (6 and 12 o'clock) and compressing on the east and west sides (3 and 9 o'clock), as shown in Figure 4-13(c) and Figure 4-14(c). The spigot contacted the top and bottom sides of the bell, which expanded the bell on both sides and resulted in compression on the other two sides, as shown in Figure 4-15.

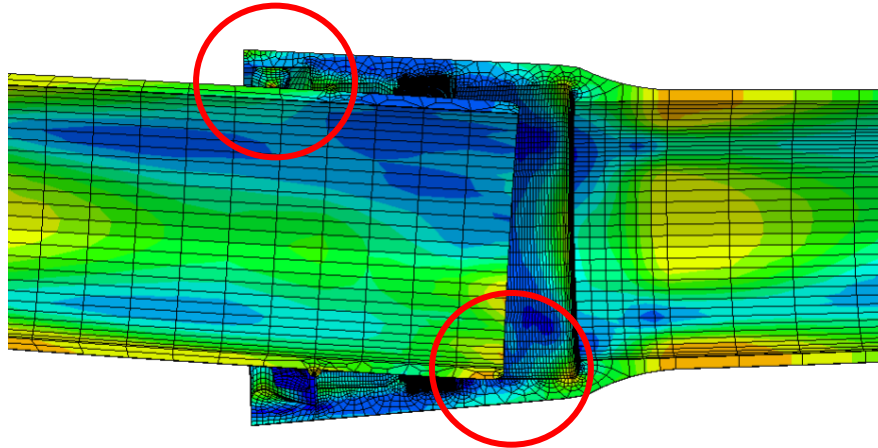


Figure 4-15 Joint deformed mechanism in Push Down stage

Pulling stage

Figure 4-16 and Figure 4-17 demonstrate the hoop strain results under 140 kips axial force conditions measured by fiber optic sensors for both specimens. Similar to the previous stage, the pipes experienced circumferential tensile strain on the top (12 o'clock) and compressive strain on the bottom sides (6 o'clock).

Due to the different orientations of the locking segments, the bells of the two specimens reacted differently. While being pulled, the locking segments in the bell section were in contact with the weld bead on the spigot. The locking segments tended to expand the bell to be pulled out. For Specimen 1, instead of a locking segment, a rubber gasket was placed on the west side (9 o'clock). Hence, the bell tends to shrink on the west and east (3 and 9 o'clock) sides and expand on the top and bottom (6 and 12 o'clock) sides, which allows the locking segments to be pulled out. Similarly, since the rubber gasket was placed on the top side (12 o'clock) of Specimen 2, the bell tends to compress on the top and bottom (12 and 6 o'clock) and expand on the west and east sides (9 and 3 o'clock).

The pipes failed because of cracks in the bells. Although the cracks propagated differently, the start points of the cracks are similar. They are at the mid-point of the top and west sides, where the boundary of the single slot and locking segments is located. For Specimen 1, the cracks started from the mid-point of the top and west sides through the top to the east. For Specimen 2, a shorter crack was observed. The cracks propagated from the mid-point of the top and west sides to the mid-point of the west and bottom sides. The start and end points of the cracks are marked on the plots of Sensor 6 in Figure 4-16 and Figure 4-17, which is located on top of the locking segments.

B. All the hoop strain results measured by the fiber optic sensors are presented in Appendix

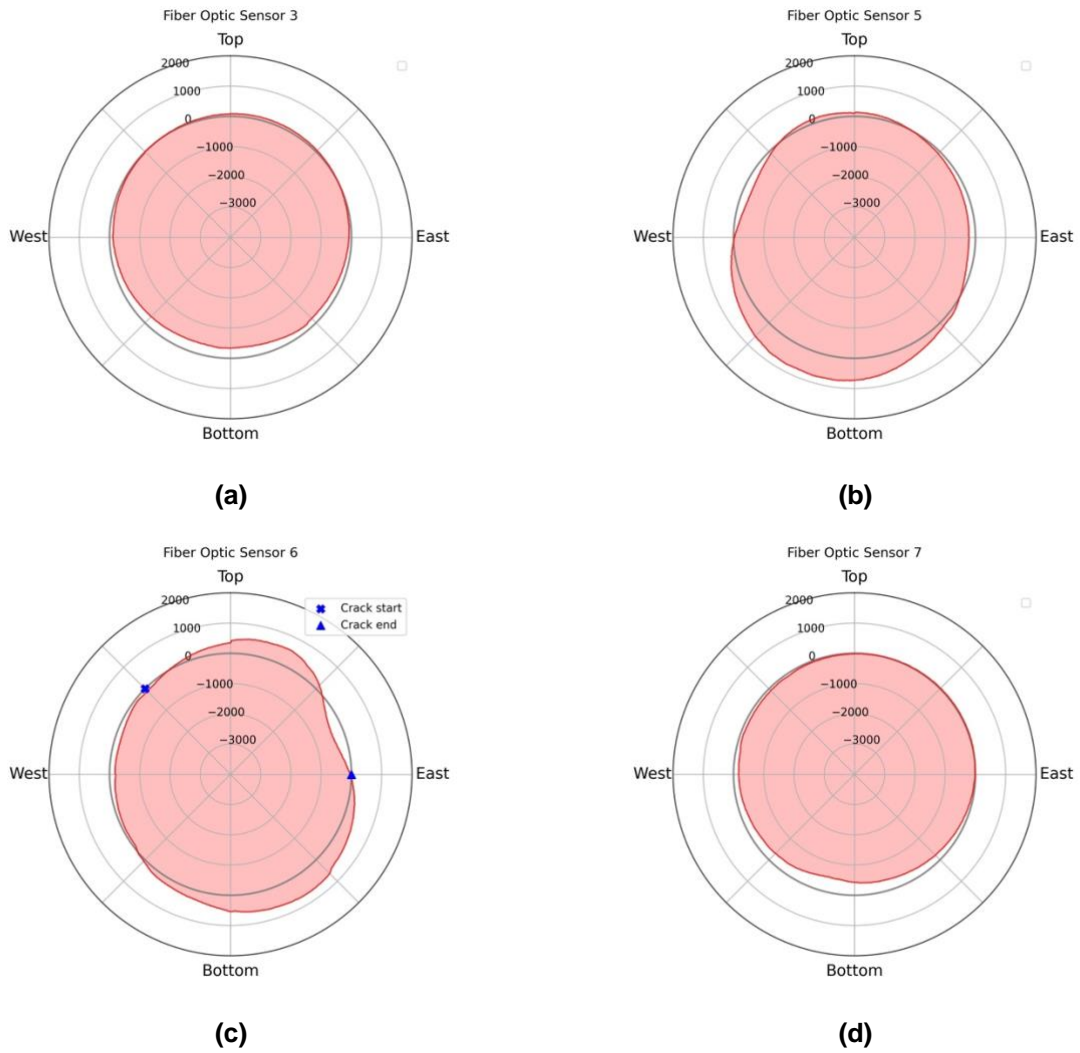
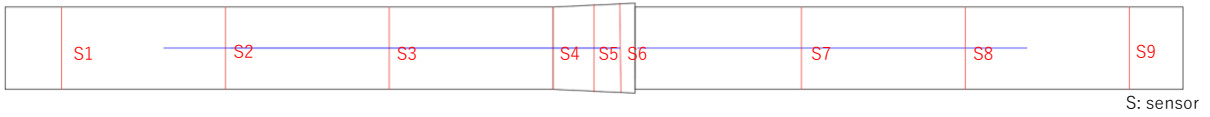
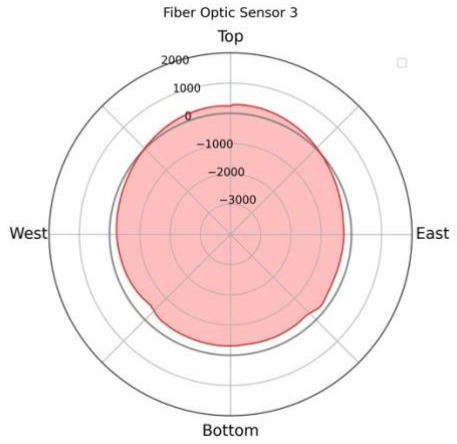
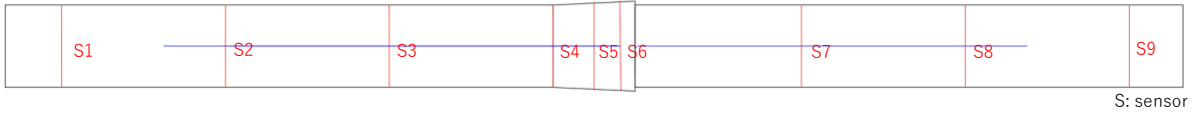
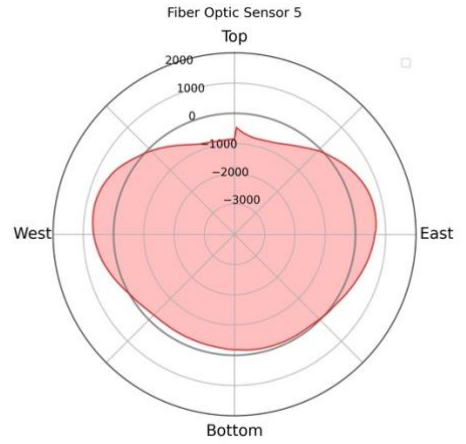


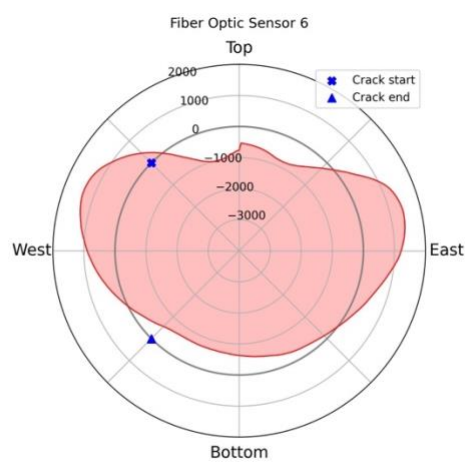
Figure 4-16 Strain distribution in the circumferential direction of Specimen 1 under 140 kips loading condition. (a) sensor on the bell pipe (b) sensor at the mid location of the bell (c) sensor on top of the locking segments on the bell (d) sensor on the spigot



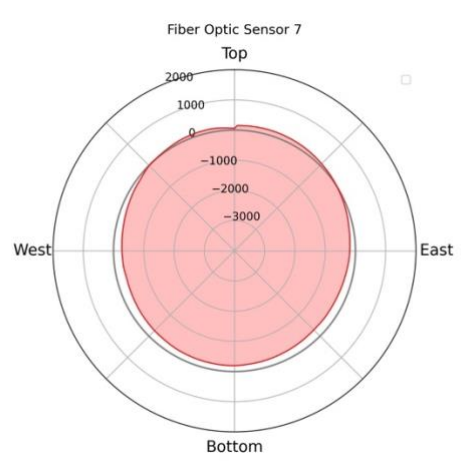
(a)



(b)



(c)



(d)

Figure 4-17 Strain distribution in the circumferential direction of Specimen 2 under 140 kips loading condition. (a) sensor on the bell pipe (b) sensor at the mid location of the bell (c) sensor on top of the locking segments on the bell (d) sensor on the spigot

4.3 Failure Modes

The experiments were designed to test up to a pipe failure or a significant water leakage resulting in a large water pressure drop. The tests were stopped due to the pipe failing at the bell near the location of the locking segments, as shown in Figure 4-18. The pipe failed with severe water leakage when the tensile forces reached 171 kips with 2.3 inches displacement and 145 kips with 2 inches displacement, respectively, meaning that the orientation of the locking segments would be influential to the seismic capacity of the pipe.

Although the cracks on the bell propagated differently, they both started from the mid-point of the west and top position, where the boundary of the single slot and locking segments is located. This would be the weak point of the bell.

The crack on Specimen 1 started from the boundary of locking segments and the single slot, located at the mid-point of the top and west sides, through the top to the east. The crack propagated from the edge to the middle of the bell. A diagonal crack can be observed, as shown in Figure 4-18, meaning that combined shear and tensile stresses dominated the failure. On the other hand, the crack along the circumference of the bell can be found in Specimen 2, indicating that tensile stress was governing the failure. The start point of the crack is similar to the location of Specimen 1, and the crack propagated to the mid-point of the west and bottom.



Figure 4-18 Failure of Bell of Specimen 1 (left) and 2 (right)

5. Finite Element Analysis

5.1 Overview of numerical model

To examine the pipeline behavior due to biaxial tension force, two three-dimensional (3D) full-scale finite element (FE) models were developed by using ABAQUS. The geometry and material of the pipe and joint models were carefully designed to be consistent with the experiments. The only difference between the two FE models is the orientation of the locking segments (9 o'clock and 12 o'clock).

In the models, the pipelines are simplified into three main parts: a spigot, a bell pipe, and three pieces of locking segments. FE meshes used for the analysis are shown in Figure 5-1, where the isotropic 3D solid continuum elements (C3D8R) are used. Especially the finer mesh at the bell section is defined to ensure strain development can be accurately determined. The number of elements and nodes in the finite element model are 124,779 and 157,117, respectively.

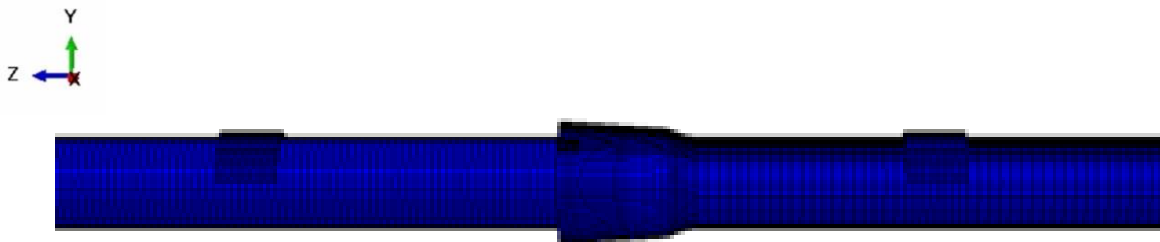


Figure 5-1 3-D FE model mesh for biaxial tension tests

The loading conditions and boundary conditions are briefly summarized as follows. At the bell joint, the interaction between the pipe and the locking segments is set to be contacted and allowed to slip into each other. The normal behavior of the interaction is set to behave as the hard contact in ABAQUS, and the friction coefficient of the tangential behavior is set as 0.8 according to the standard friction coefficient between materials of ductile iron and steel. To simulate the pipeline subjected to bending moment, two ends were set to allow deflection while being bent. In the simulation, the bending force is applied on the loading saddles, similar as the experimental setup. In order to model the situation well, a couple of uniform nonlinear pressure results was applied on the two 6-in-width loading saddles. At the pulling stage, the spigot end is allowed to move horizontally up to 5 inches displacement, same as the experiment. In addition, 50 psi water pressure is applied on the inside surface of the pipes.

The analysis is performed in three stages. The initial position of the bell and spigot is located the same as in the experiment, as shown in Figure 5-2. A vertical displacement of 2.34 inches is first applied to the pipe, which corresponds to 8 degrees of rotation. The vertical loading location on the pipes is set to be the same as those in the lab tests. Then the axial force is applied to the spigot until the bell joint breaks.

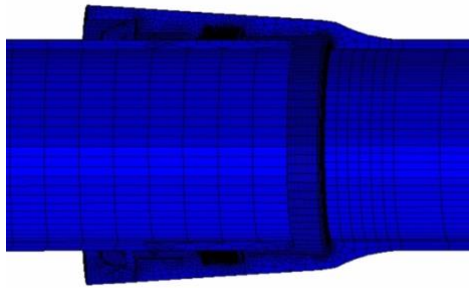


Figure 5-2 FE mesh for bell joint and initial position of the bell and spigot

5.2 Determination of Pipe Parameters

Figure 5-2 presents the material properties provided by U.S. Pipe for the ductile iron pipe and locking segments used in the tests. The plastic properties are included in the simulation to accommodate some parts of the pipe reaching the yielding stress of the material, resulting in plastic deformation.

Von Mises stress is a value used to determine if a given material yields or fractures in shear. It is mostly used for ductile materials. For the tested US pipes, when the value of Mises stress exceeds the yield stress (42,000 psi), the pipe generates plastic strains with irreversible deformation. The properties utilized in this FE model align with those used for the Tension test finite element method.

Table 5-1 Ductile Iron Pipe properties

Part	Density (lb/in ³)	Young's Modulus (psi)	Poisson's Ratio	Yield Strength (psi)	Ultimate Strength (psi)	Elongation
Ductile Iron Pipe (plastic)	0.28	23,500,000	0.29	42,000	60,000	10%
Locking segments (plastic)	0.3	24,000,000	0.26	42,000	60,000	10%

5.3 FEM Results of Test 1

5.3.1 Overview of FE analysis

Figure 5-3 depicts a comparison of the moment-rotation and axial force-average joint opening relationships obtained from FE analysis and the experimental results of Test 1.

As shown in the moment-rotation plot, the trends and peak values are similar between the results from FE analysis and the experimental result. Both FEM analyses and experimental results demonstrate approximately 5 degrees of flexible rotation with minimal moment generation. Then,

the spigot starts to establish internal contact with the bell, which results in moment generation until the joint achieves an orientation of approximately 8 degrees.

Looking at the plot of axial force and average joint opening, test results demonstrate that the average joint opening increases from 0 to 1.8 inches with a smaller axial force, corresponding to the Push Down stage. Subsequently, the spigot was subjected to axial force until the locking segments were pulled out from the bell with maximum joint opening around 2.25 in.

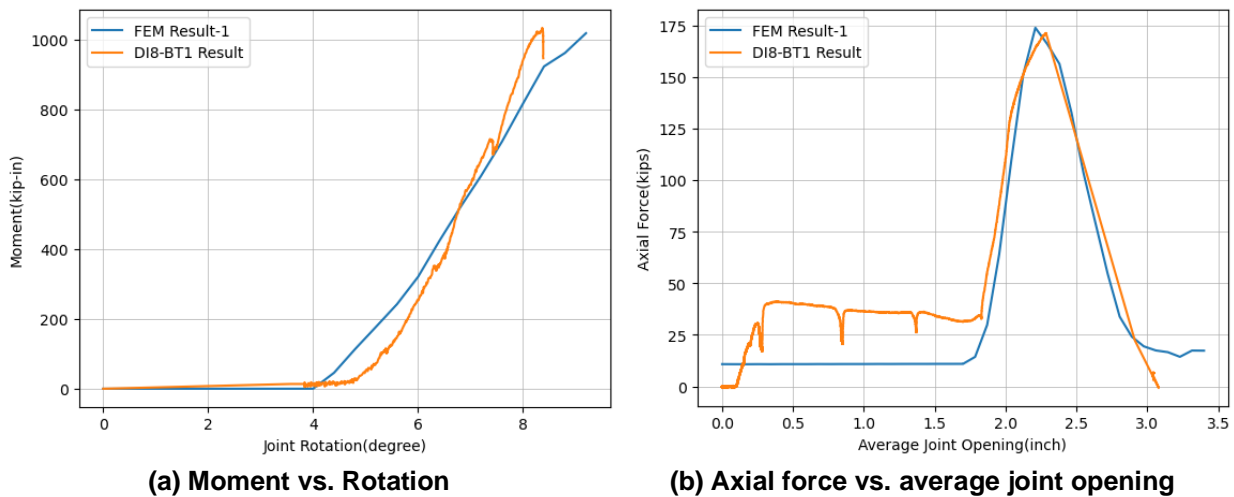


Figure 5-3 Comparison of FEM results and Test-1 results

Figure 5-4 shows the Mises stress contour and deformation of the bell pipe and spigot when a vertical displacement of 2.34 inches is applied. This corresponds to around 8 degrees of rotation. Because of the rotation, a significant stress concentration can be found at the bottom of the spigot inside the bell, where the spigot bears against the bell.

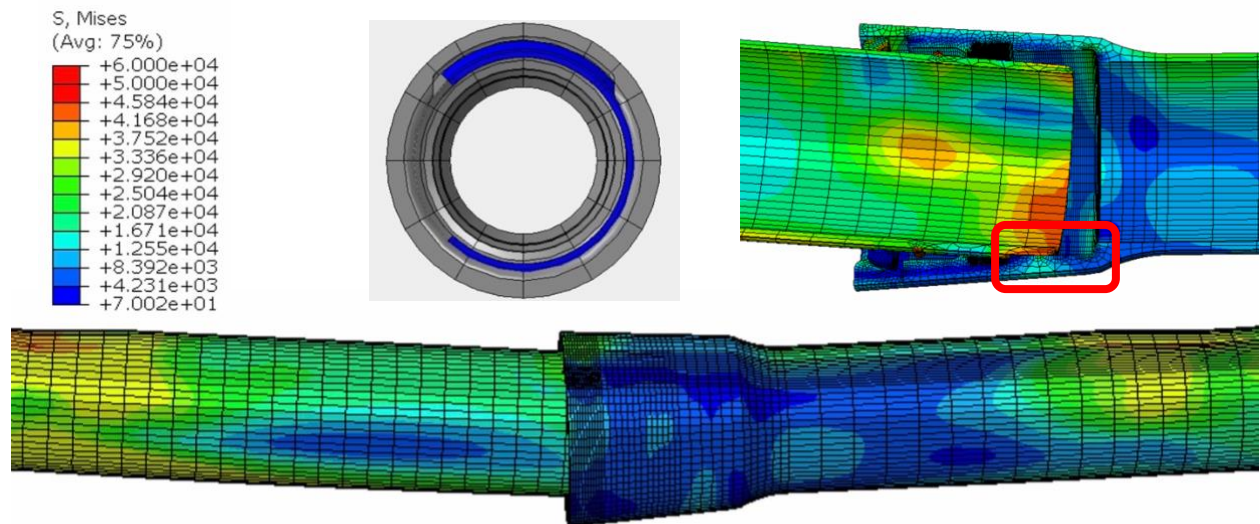


Figure 5-4 The stress contours of the deformed joint of test 1 (Actuator Push Down)

Figure 5-5 shows the Mises stress contour and deformation of the bell pipe and spigot when the spigot is pulled to around 2.2 inches, corresponding to about 140 kips axial force. While being pulled, the bell joint is restrained from moving up (i.e., the rotation remains at least 8 degrees), and the locking segments are allowed to slip out of the bell, the same as in the lab test. The spigot made contact with the bell invert, resulting in significant deformation at the bottom of the spigot and the crown of the bell edge.

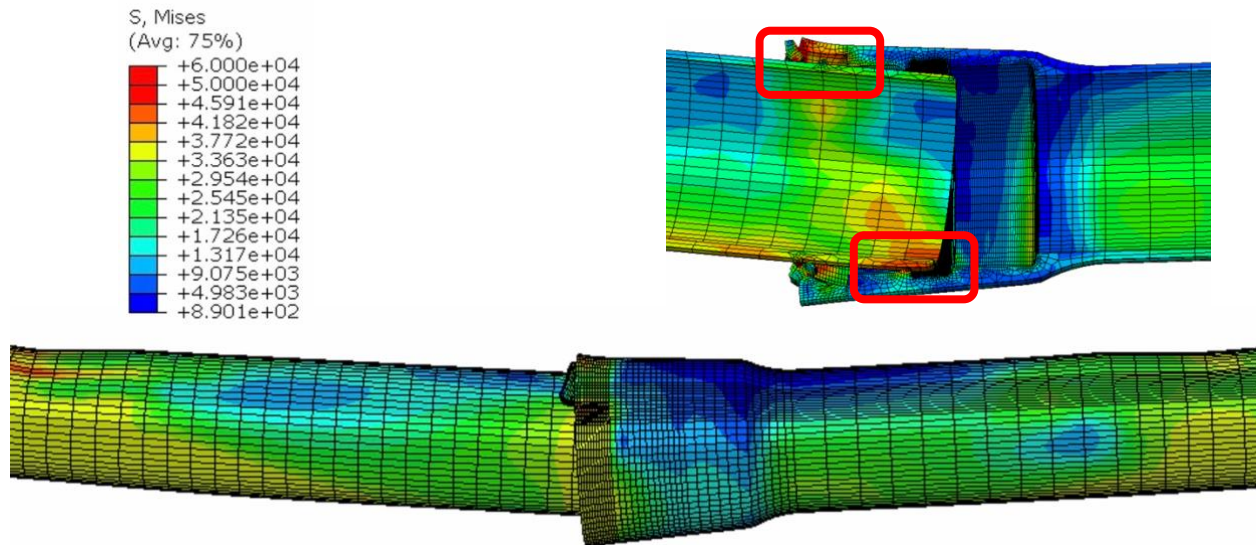


Figure 5-5 The stress contours of the deformed joint of test 1 (Pull)

5.3.2 Bell deformation

Figure 5-6 shows the Mises stress distribution of the bell cross-section at the initial, Actuator Push Down, and Pull stages, respectively. During the Actuator Push Down stage, the shape of the bell remains almost unchanged. After the axial displacement reaches 2.2 inches, the bell cross-section deformed to an ellipse with irrecoverable deformation. A thinner geometry at the crown can be found. This is because of the locking segments being pulled out and expanding the sides of the bell, resulting in decreasing the thickness of the top of the bell.

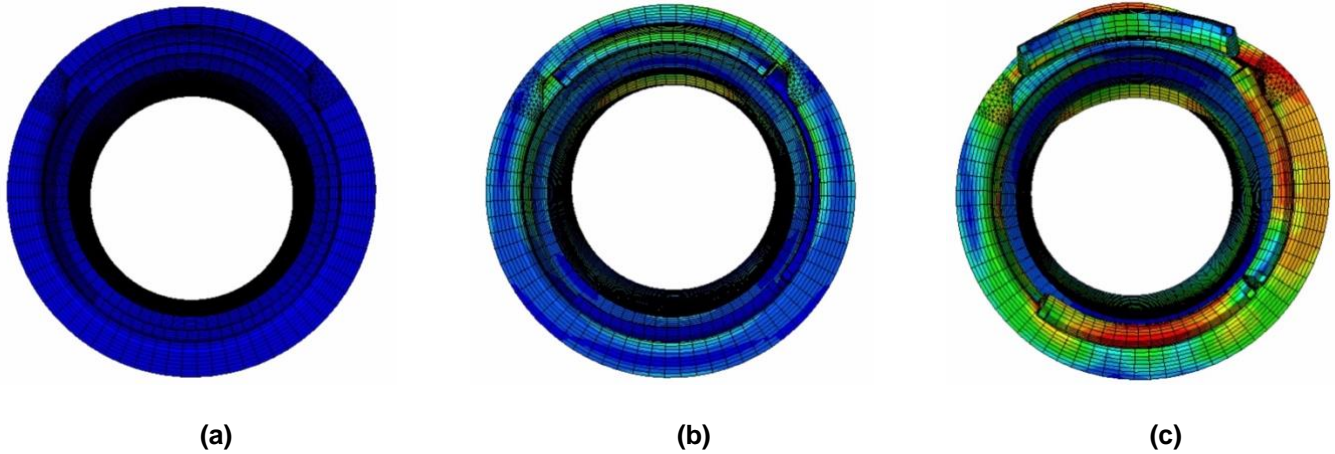


Figure 5-6 The stress contours of bell cross-section: (a) initial stage (b) actuator push down (c) pull

Figure 5-7 shows the corresponding locations of the locking segments at the three stages, respectively. They started to be detached during the Actuator Push Down stage. As the axial loading increases, the locking segments try to slip out from the bell, resulting in higher stress.

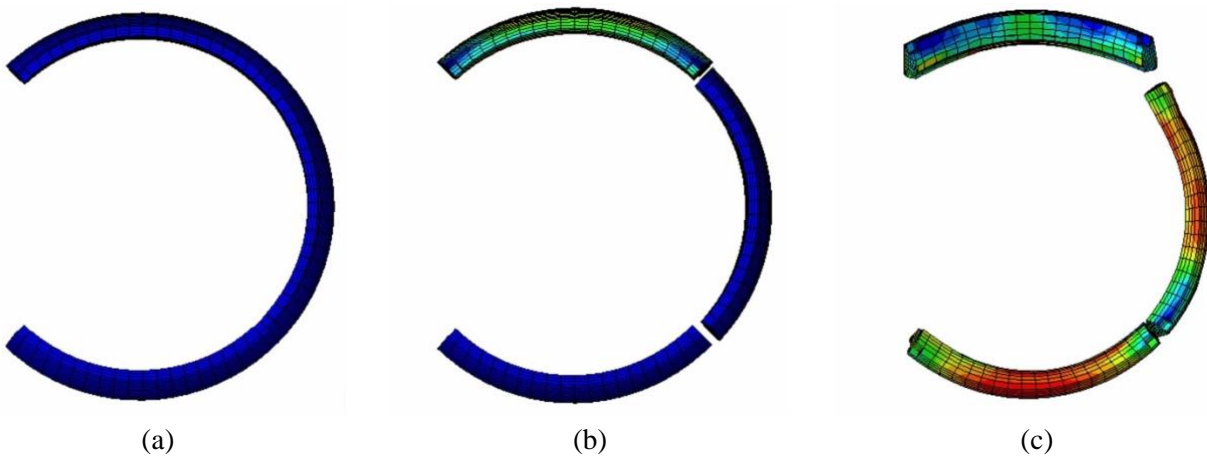


Figure 5-7 The stress contours of locking segments: (a) initial stage (b) actuator push down (c) pull

5.3.3 Spigot deformation

Figure 5-8 shows the Mises stress distribution of the spigot internal cross section at the three stages. During the Actuator Push Down stage, the invert of the spigot shows significant concentrated stresses. The spigot cross section is squeezed into an ellipse. The weld bead deforms at the area where it bears against the locking segments, as shown in Figure 5-9.

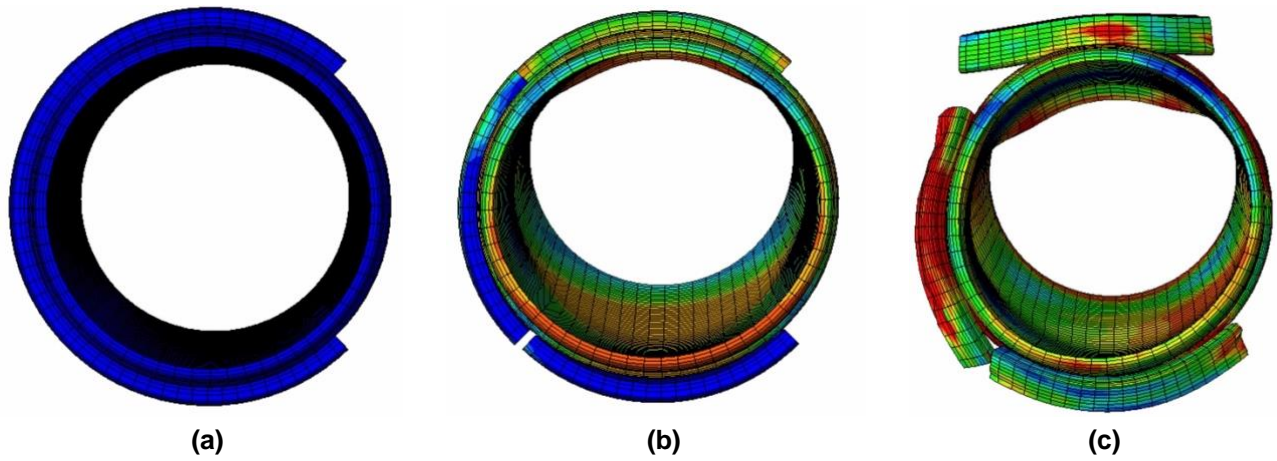


Figure 5-8 The stress contours of spigot cross-section: (a) initial stage (b) actuator push down (c) pull

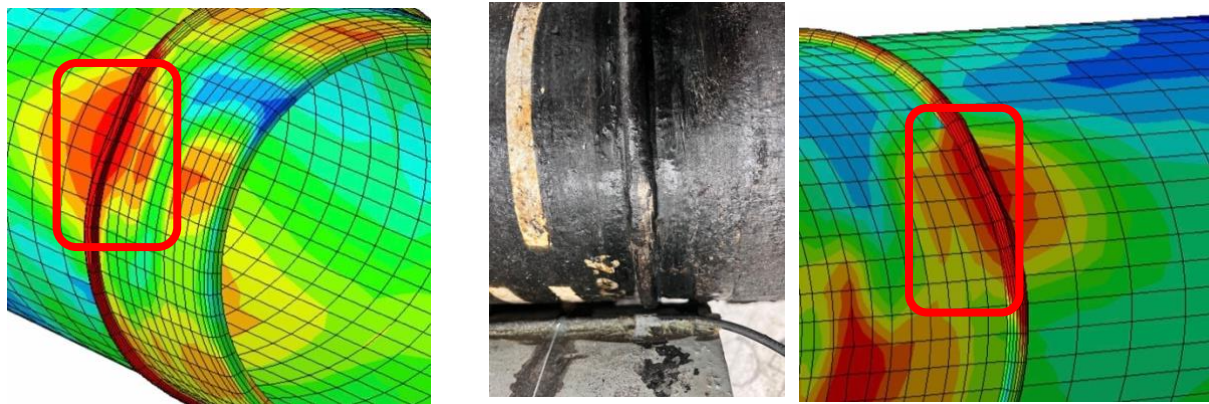
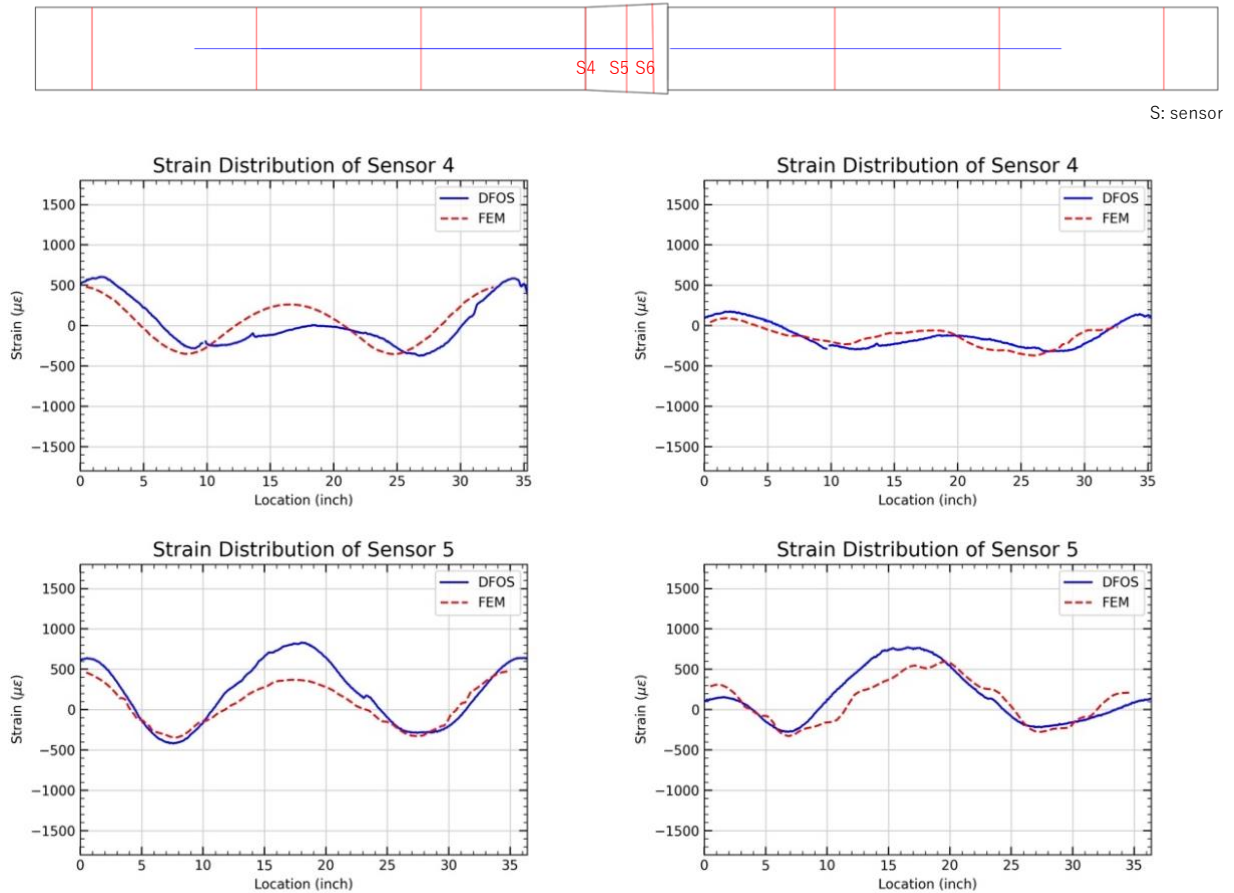


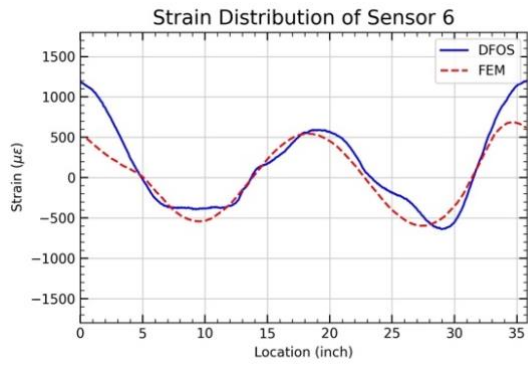
Figure 5-9 The deformation of the weld bead

5.3.4 Strain comparison of the FE Model and Experimental Data

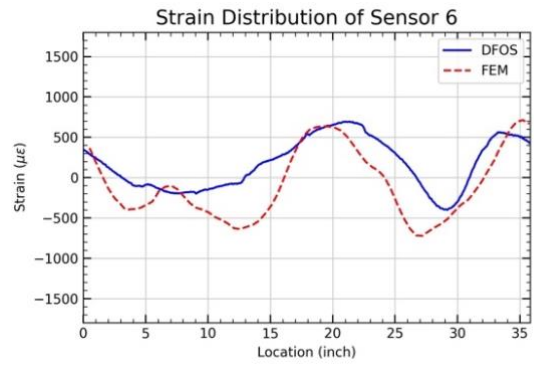
Figure 5-10 and Figure 5-11 show the comparison of the longitudinal strain distribution on the pipe from the FE analysis and the experiments. The FE simulation results show good agreement with the pipeline behavior observed in the lab test. The data from Sensor 4, Sensor 5, and Sensor 6 in Figure 5-10 indicate the circumferential strains at the bell joint (bell end, mid-point, and top of the locking segments, respectively). The circumferential results from the FE models match well with the DFOS data, meaning that the FE models are capable of predicting the behavior of the bell under both bending and pulling conditions.

The data from Sensor 14 and Sensor 16 in Figure 5-11 correspond to the longitudinal strains at the east (3 o'clock) and bottom (6 o'clock) sides. The gaps in the DFOS data are the loading saddle locations. The results between the FE model and the DFOS experimental data match well for Sensor 16. However, Sensor 14 shows little difference. Therefore, in the model, it is assumed that the areas where the force is transferred are the largest possible contact areas between the loading saddle and the pipe, which might not be exactly the same as in the lab test.





(a)



(b)

Figure 5-10 Comparison of circumferential strains (a) Actuator push down (b) Pull to 2.2 inches

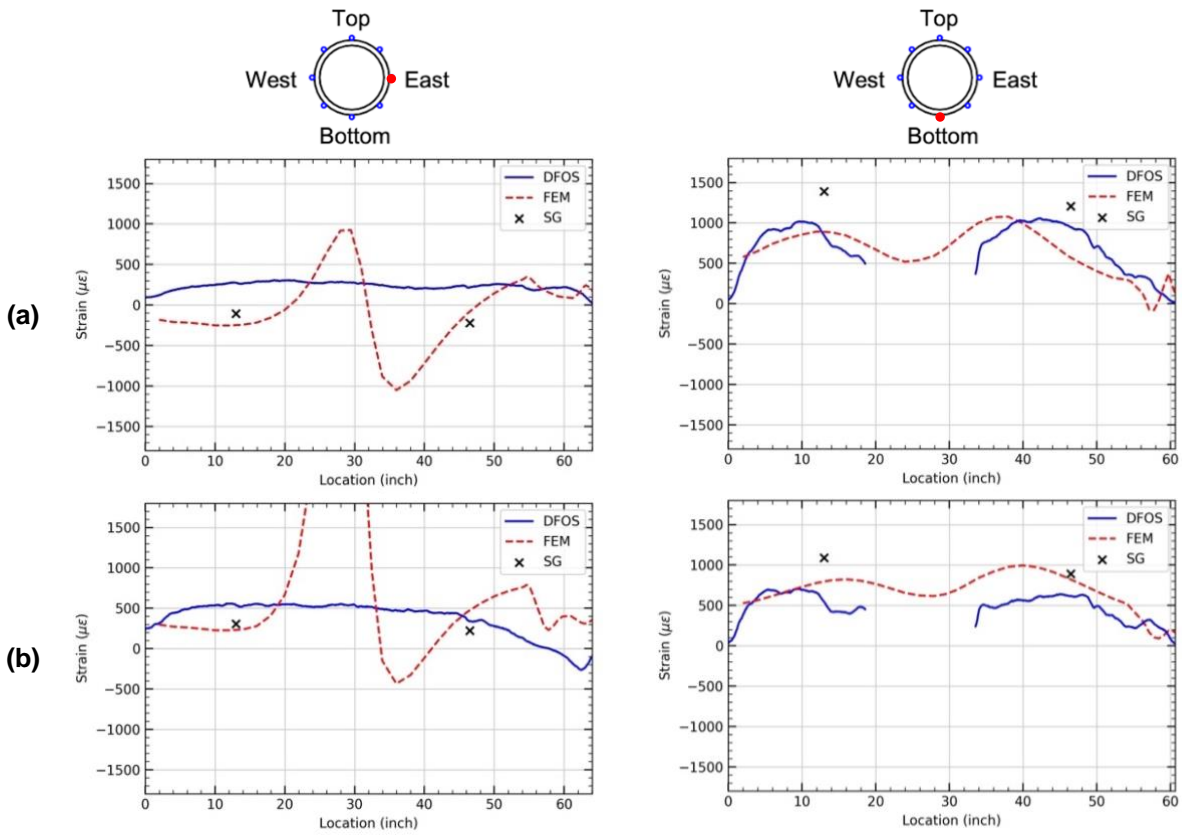


Figure 5-11 Comparison of longitudinal strains (a) Actuator push down (b) Pull to 2.2 inches

5.4 FEM Results of Test 2

5.4.1 Overview of FE analysis

Figure 5-12 depicts a comparison between the moment-rotation and axial force-average joint opening relationships obtained from FE analysis and the experimental results of Test 2.

Looking at the moment-rotation plot, one can observe that, although the ultimate moment and rotation has a little difference between the result from the experiment and the FE analysis, a good trend between the FE analysis and experimental results matches well. Similar to Test 1, results demonstrate approximately 5 degrees of flexible rotation with minimal moment generation and then spigot started to contact to bell until 8 degree.

On the other hand, the trend and maximum capacity of the average joint opening and axial force show good agreement between the FE analysis and experimental result, as shown in Figure 5-12(b). Initially, the average joint opening increases nonlinearly from 0 to 1 inch as the axial force rises up to about 50 kips, corresponding to the Push Down stage. Subsequently, both the FEM and experimental results demonstrate a nearly linear relationship between axial force and average joint opening up to about 2 inches, indicating the Pull stage.

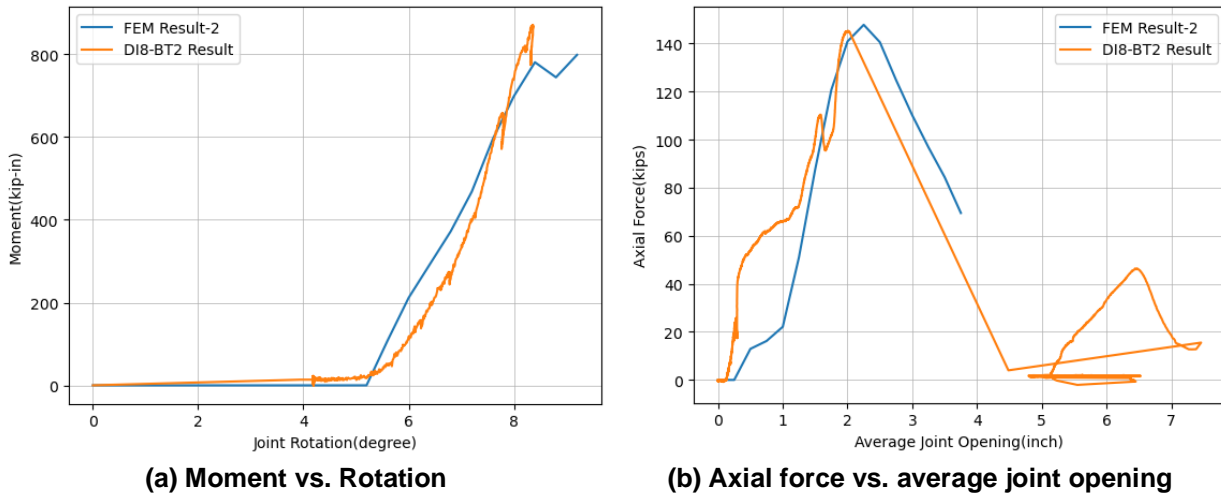


Figure 5-12 Comparison of FEM results and Test-2 results

The FE results of Test 2 (i.e., 12 o'clock locking segments orientation) are discussed herein. Figure 5-13 shows the Mises stress contour and deformation of the bell pipe and spigot when a vertical displacement of 2.34 inches is applied. This corresponds to around 8 degrees of rotation. Similar to Test 1, concentrated strains on the bottom of the spigot can be observed.

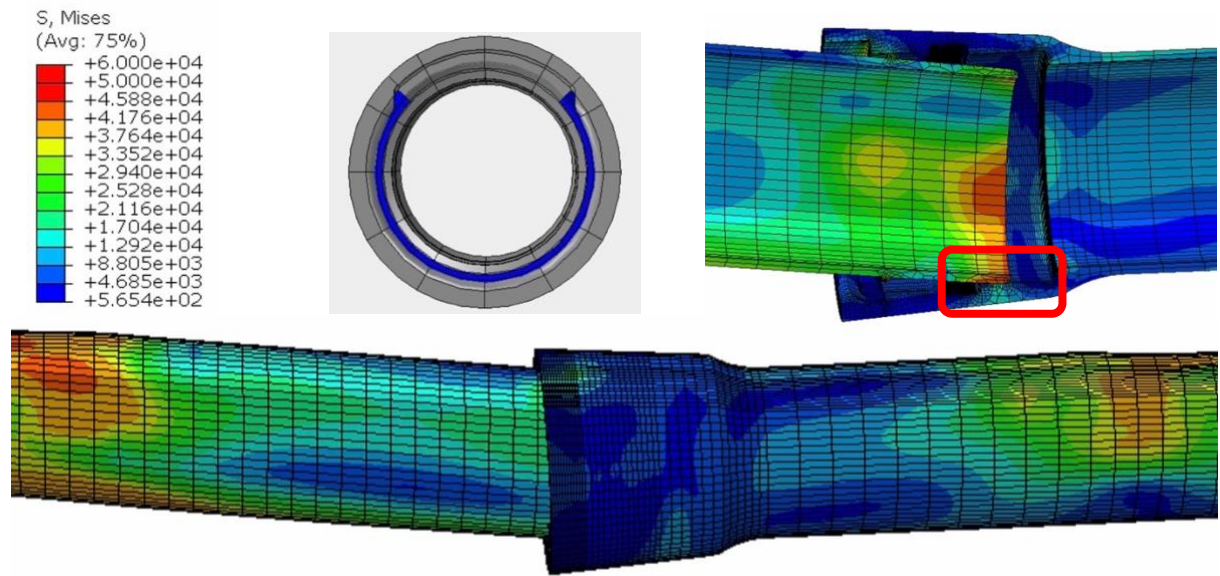


Figure 5-13 The stress contours of the deformed joint of test 2 (Actuator Push Down)

Figure 5-14 shows the Mises stress contour and deformation of the bell pipe and spigot when the spigot is pulled to around 2.2 inches. Similar to the boundary condition set for Test 1, during the Pull stage, the bell joint is restrained to 8 degrees of rotation. As shown in the figure, the spigot makes contact with the bell invert, resulting in significant deformation of the bottom of the spigot and the crown of the bell edge.

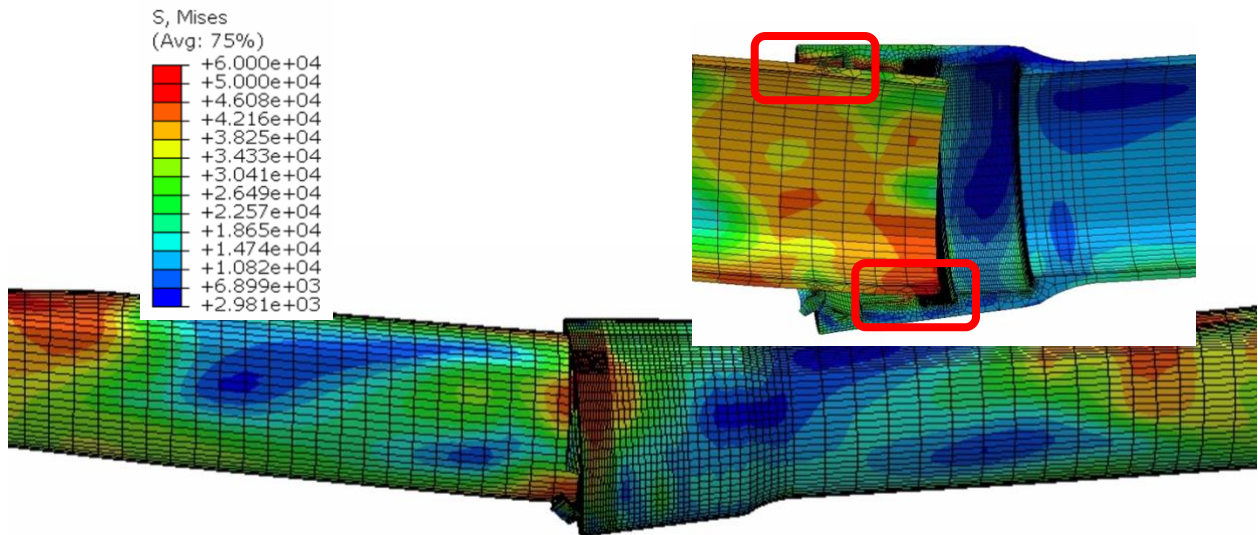


Figure 5-14 The stress contours of the deformed joint of Test 2 (Pull)

5.4.2 Bell deformation

Figure 5-15 shows the Mises stress distribution of the bell cross-section at the initial, Actuator Push Down, and Pull stages, respectively. Same as Test 1, it can be seen that, during the Actuator Push Down stage, the shape of the bell merely changed. The bell cross-section deforms while being pulled. Unlike Test 1, which shows the non-symmetric stress and deformation distribution, the stress and deformation of Test 2 are symmetric due to the symmetric of the locking segments in the direction of the vertical load.

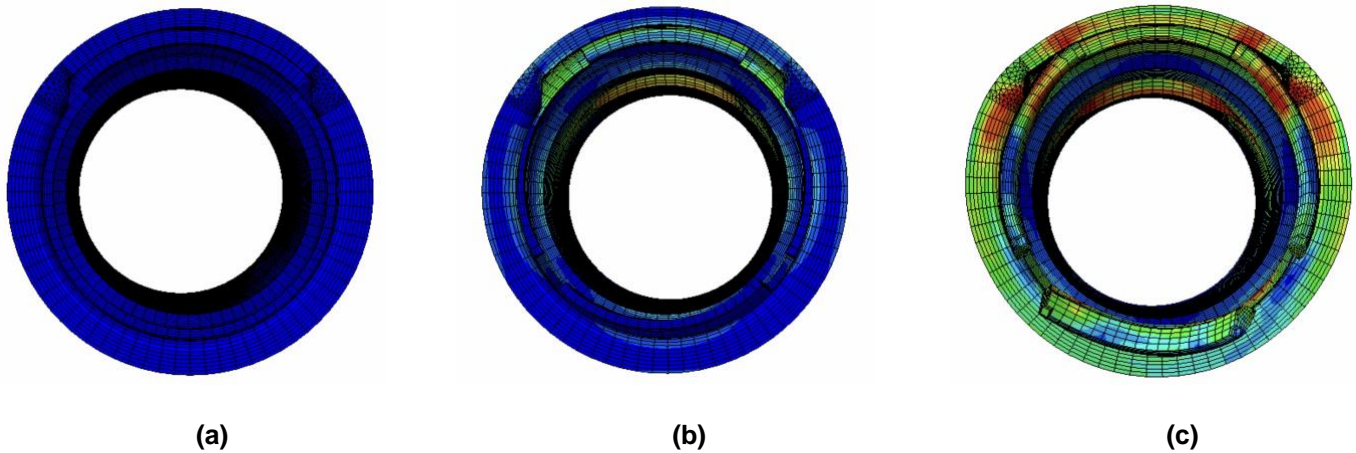


Figure 5-15 The stress contours of bell cross-section: (a) initial stage (b) actuator push down (c) pull

Figure 5-16 shows the corresponding locations of the locking segments at the three stages, respectively. Similar to the observation made from Test 1, the locking segments start to detach when the vertical force is applied. When the axial load increases, the locking segments slip out from the bell, resulting in higher stress.

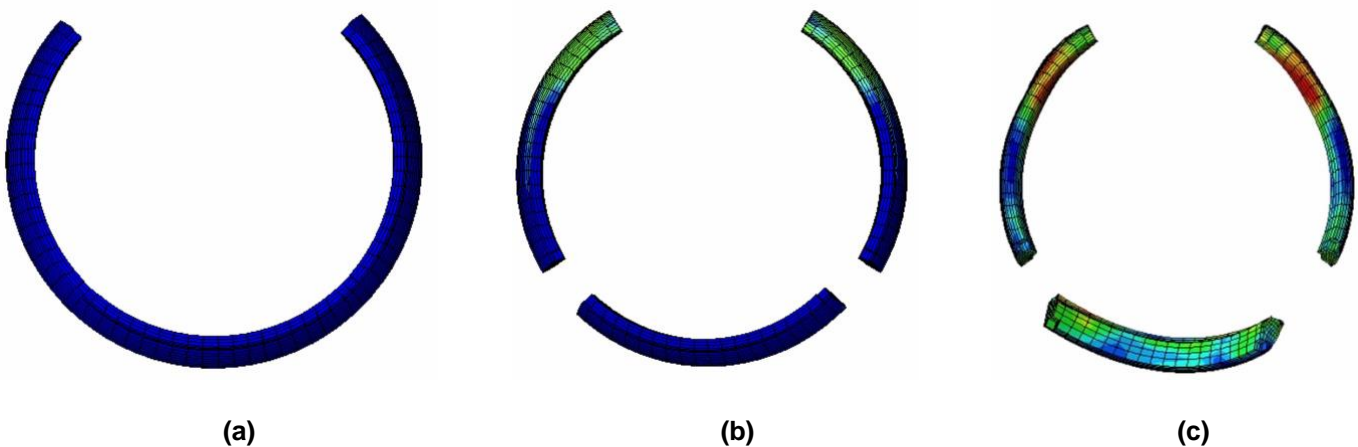


Figure 5-16 The stress contours of locking segments: (a) initial state (b) actuator push down (c) pull

5.4.3 Spigot deformation

Figure 5-17 shows the Mises stress distribution of the internal spigot cross-section at the three stages, respectively. Compared to the deformation of Test 1, the spigot exhibits symmetrical stress distribution and deformation. The invert of the spigot shows significant concentrated stress.

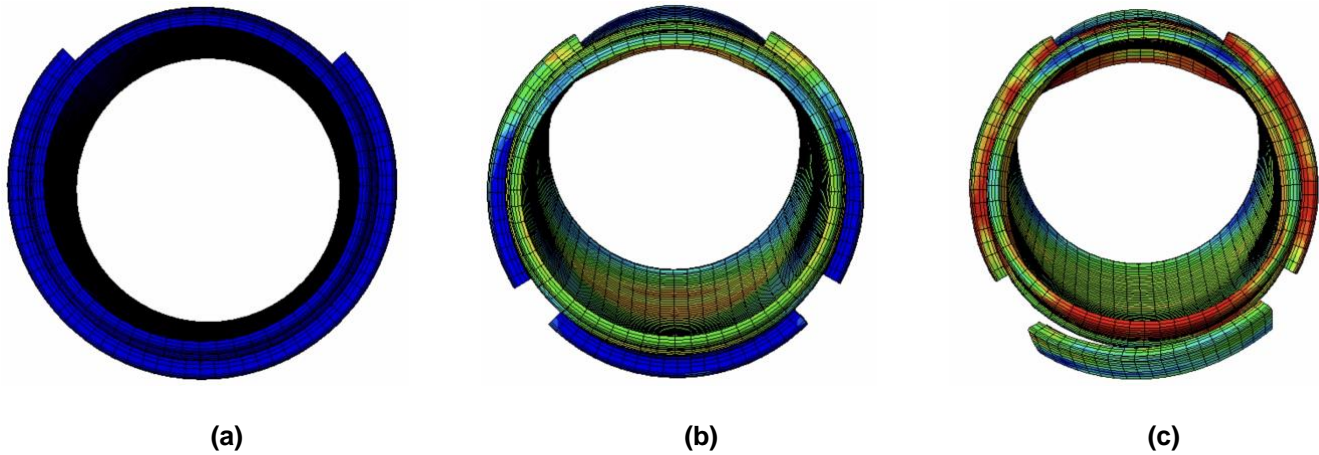
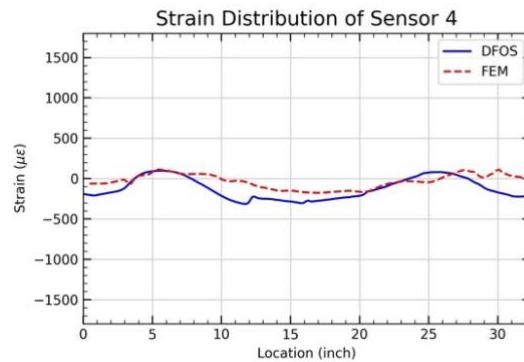
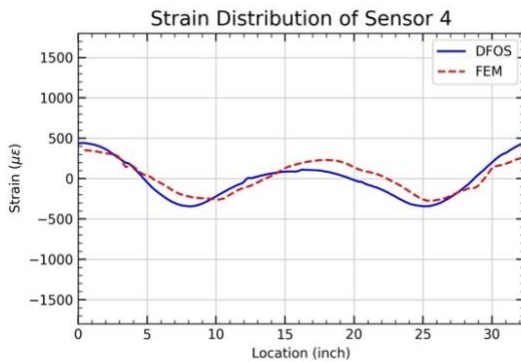


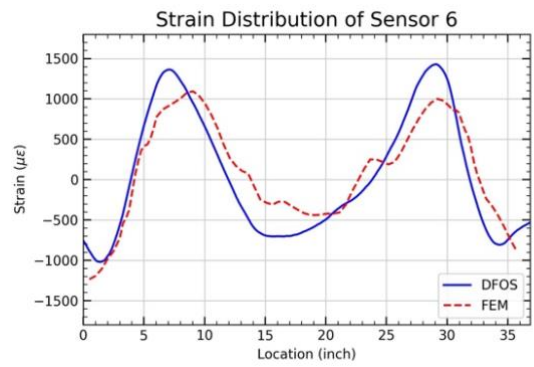
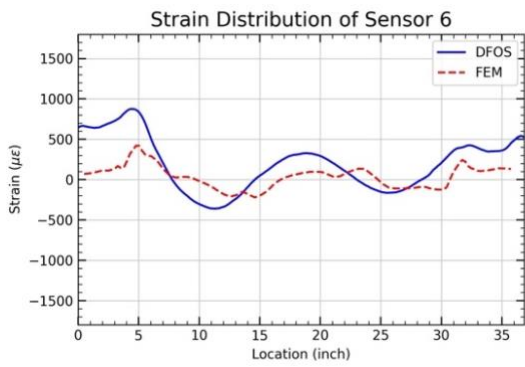
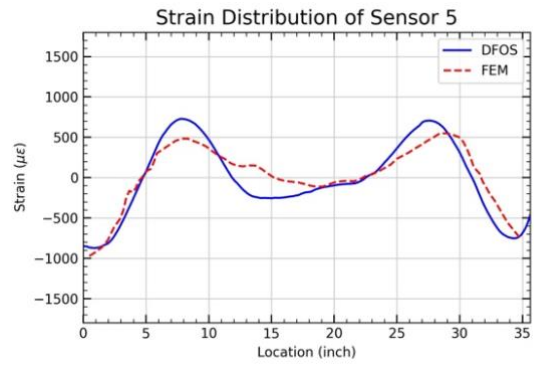
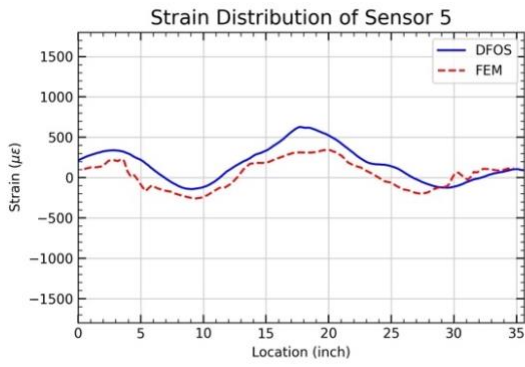
Figure 5-17 The stress contours of spigot cross-section: (a) initial state (b) actuator push down (c) pull

5.4.4 Strain comparison of the FE Model and Experimental Data

The FE simulation results show good agreement with the experimental data of the pipeline behavior observed from the lab test. The data from Sensors 4, Sensor 5, and Sensor 6 in Figure 5-18 indicate circumferential strain distribution at the bell joint, while the data from Sensor 14 and Sensor 16 in Figure 5-19 indicate longitudinal strain distribution at the bottom (6 o'clock) and east (3 o'clock) of the bell pipe.

Sensor 5 and Sensor 6 show different strain mechanisms compared to those of Test 1, while Sensor 14 and Sensor 16 show similar strain distributions. This indicates that the locking segments orientation influences the circumferential strain distributions more than the axial strain.

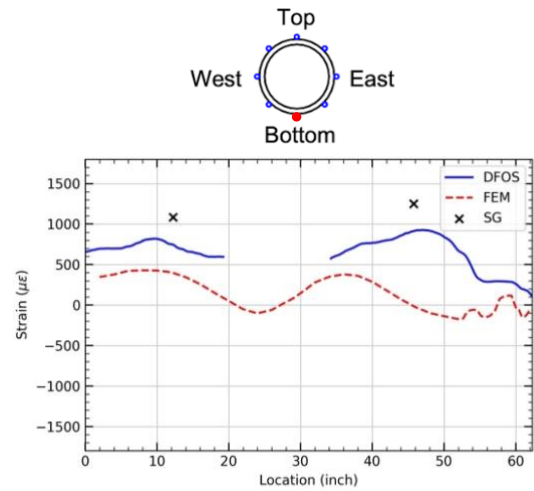
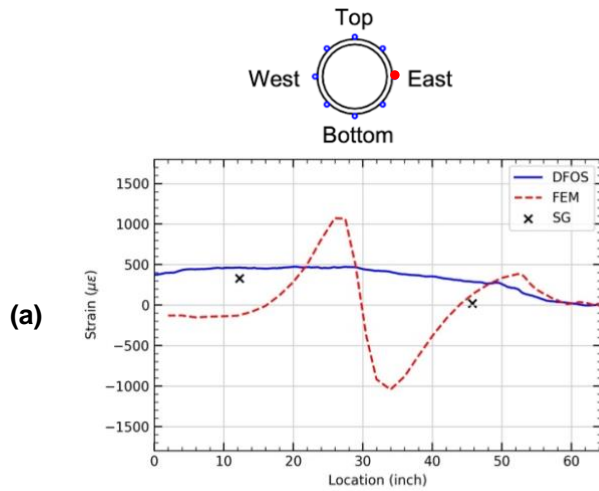




(a)

(b)

Figure 5-18 Comparison of circumferential strains (a) actuator push down (b) pull to 2.2 inches



(a)

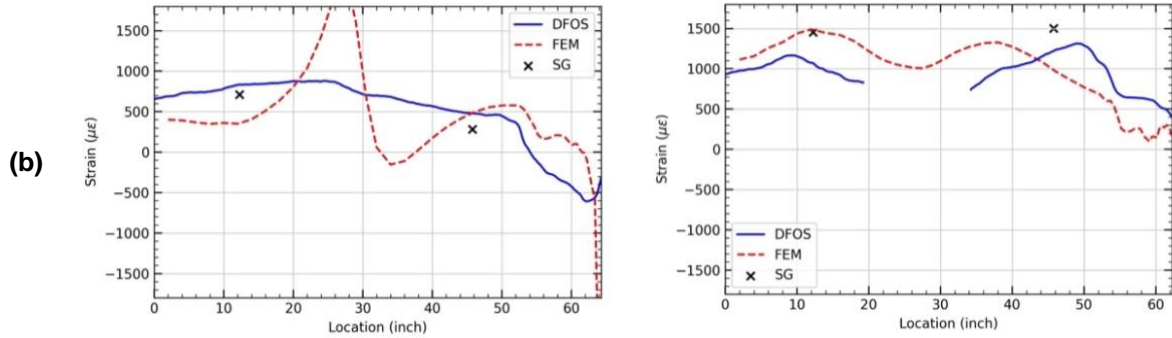


Figure 5-19 Comparison of longitudinal strains (a) actuator push down (b) pull to 2.2 inches

5.5 Failure mode comparison between FEM and experiments

Figure 5-20 and Figure 5-21 compare the simulated joint deformation with 3D distributions of Mises stress while the spigot is pulled to 2.2 inches during the Pull stage. Note that the pipes were restrained to maintain 8 degrees of rotation at this stage. The cylindrical coordinates in Abaqus, S11, S22, S33, and S23 represent the radial stress, circumferential stress, longitudinal stress, and shear stress, respectively. The lab tests show that both specimens failed at the mid-point of the west and top position, where the boundary of the single slot and locking segments located.

In Test 1, although the FE results (Mises stress distribution) do not show a consistent crack path with the experimental result, the FE model shows the same location of crack initiation. The vulnerable area is around the crown of the bell joint. The reason may be due to the contact pressure between the locking segment on the top and the bell crown. That is, the thinner geometry at the crown may result in failure. Figure 5-21 shows the circumferential tensile stress (S22), which is the dominant stress that causes cracks.

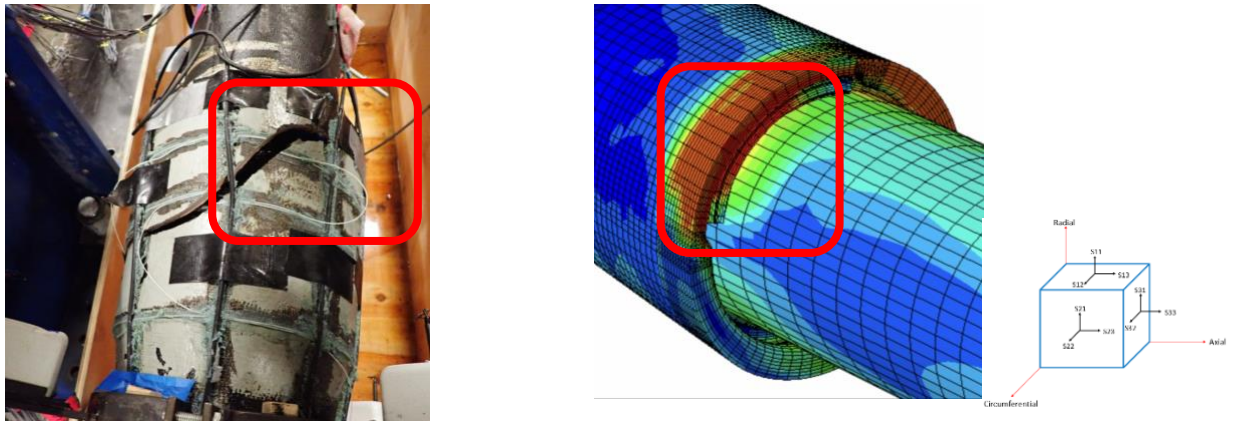


Figure 5-20 Failure mode comparison of Test 1

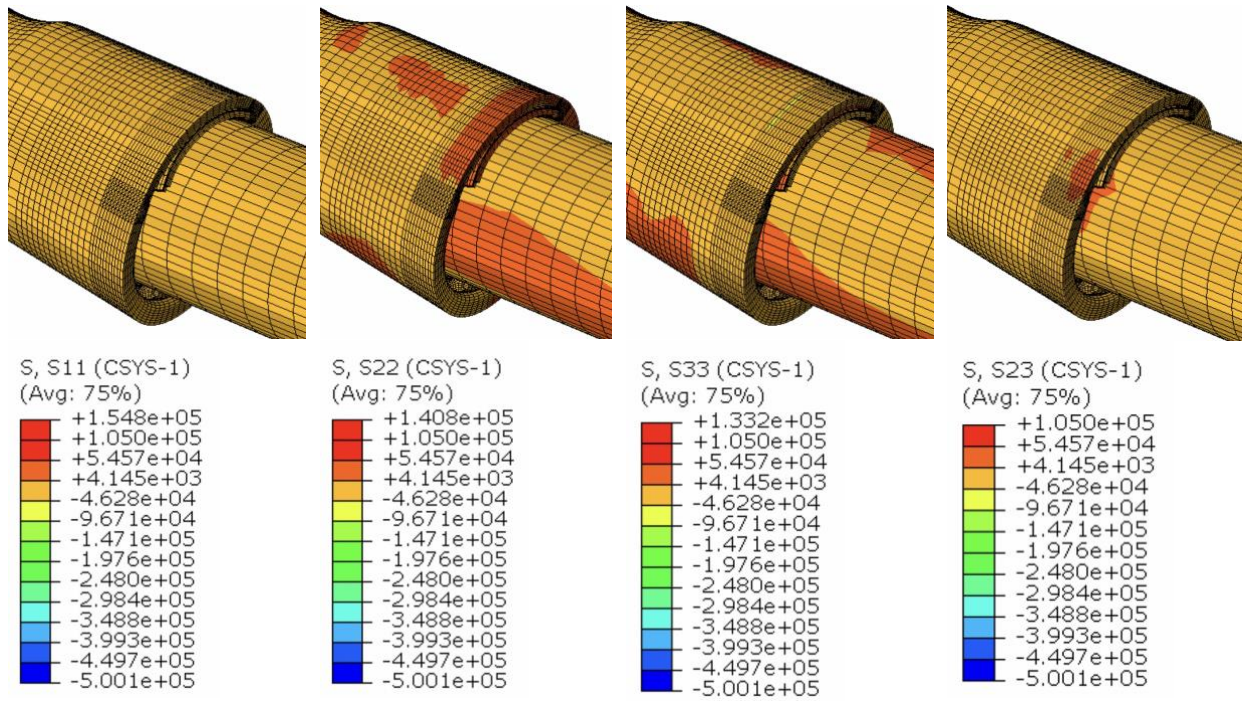


Figure 5-21 The stress contours of S11, S22, S33, S23 for Test 1

In Test 2, the Mises stress distribution shows that the crack starts from the mid-point of the west and top position and propagates down to the bottom of the pipe. This matches the failure mode observed from Test 2, as shown in Figure 5-22. The failure mode in Test 2 is different from that of Test 1, mainly due to the orientation of locking segments. Similar to Test 1, the circumferential tensile stress (S22) dominates the failure, as shown in Figure 5-23.



Figure 5-22 Failure mode comparison of Test 2

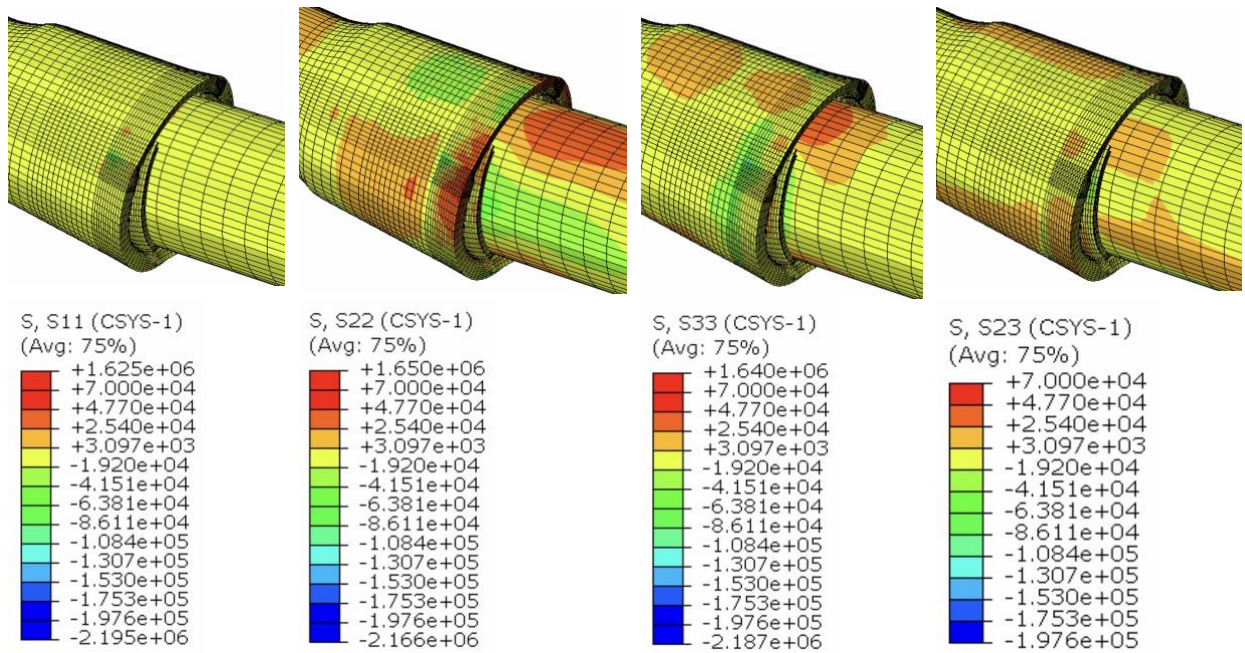


Figure 5-23 The stress contours of S11, S22, S33, S23 for Test 2

6. Conclusion

This report describes the results of the experiments focused on the performance of bell joints under biaxial tension forces (combined bending and tension force). The performance of two pipes with different locking segment orientations is discussed.

It was found that the weak area was likely to be the edge between the locking segments and the single slot for both specimens. However, the way the cracks propagated were different between the two specimens. For Specimen 1 (9 o'clock orientation), the crack propagated diagonally to the top of the bell, indicating a combined shear and tensile failure mechanism. For Specimen 2 (12 o'clock orientation), the crack propagation was along the circumferential direction, meaning that tensile stress governs the failure. In addition, Specimen 1 had a larger moment and axial force capacity with similar joint deflection and average joint opening compared to Specimen 2, indicating that the orientation of the locking segments has a great influence on the moment and rotation capacity.

The experimental results were used to validate the FE model. The strain distribution and patterns match well between the experiments and the simulation, especially in the bell area. This indicates that the proposed FE model is capable of predicting the behavior of the pipes under combined bending and tensile forces. The FE model results show the weakest location is within 2.2 inches from the edge of the bell, propagating upward to the crown in Test 1 and downward to the bottom in Test 2. The FE model results also show the bottom of the spigot inside the bell may be another potential failure location. The proposed model can be used for future parametric studies and as a reference for additional pipe design guidance.

7. Reference

- U.S. Pipe. (2020). TR XTREME [Brochure]. https://www.uspipe.com/wp-content/uploads/2020/12/USP_TR_XTREME_Brochure_03-03-2020-for-web.pdf?fbclid=IwAR2n950mDSY8OQ39WFCoVzV8WWoNmk_ae88eCPNjQym1okpuRK7mLp6absE
- LUNA inc. (2022). ODiSI 6000 Series Optical Distributed Sensor Interrogators. Retrieved from <https://lunainc.com/sites/default/files/assets/files/data-sheet/Luna%20ODiSI%206000%20Data%20Sheet.pdf>
- Wu, J., Jiang, H., Su, J., Shi, B., Jiang, Y., & Gu, K. (2015). Application of distributed fiber optic sensing technique in land subsidence monitoring. *Journal of Civil Structural Health Monitoring*, 5(5), 587-597.

Appendix A: Distributed Fiber Optic Sensing

Using the physical properties of light, fiber-optic sensing can detect changes in temperature, strain, and other parameters when light travels along a fiber, which uses fiber-optic cables as sensors and can measure over long distances at 100 to 1000s of points on a single cable or multiplexed cables depending on the analyzer used. Compared to the other sensing technologies, fiber-optic sensing has distinct advantages such as small size, light weight, and strong resistance to corrosion and water. Distributed fiber optic sensing consists of two main components, an analyzer, and fiber-optic cables. LUNA ODiSI 6000 series interrogator was used as the analyzer, and NanZee Sensing Technology Co manufactured the fiber-optic cables in the experiments.

LUNA Interrogator




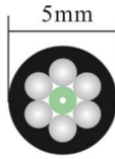
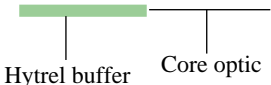
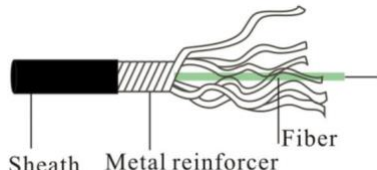
Figure A-1. LUNA ODiSI 6000 Series optical distributed sensor interrogator (LUNA, 2022)

LUNA ODiSI 6104 is an optical distributed sensor interrogator that can provide thousands of strain or temperature measurements per meter of a single high-definition fiber sensor. High-Definition H.D.D) Sensors - Strain & Temperature (HD-SC) temperature sensors utilize an advanced interrogation mode of the ODiSI to increase the accuracy of measurements when the sensors are subjected to strain, such as in embedded and surface-mount installations. It can achieve a sensor gauge pitch (the distance between two measurement points) as small as 0.65 mm, a sensor length of up to 50 m, and a measurement rate of up to 250 Hz with an accuracy of less than ± 1 microstrain.

Fiber-optic Cable

Two types of fiber optic cables manufactured by NanZee Sensing Technology Co. were used; (a) 5 mm diameter armored cable (NanZee 5mm) and (b) 0.9 mm diameter cable (NanZee 0.9mm). Table A-1 lists the information on the cables. The difference between the two cables is the thickness and material of the coating. NanZee, a 5mm cable, provides a sheath layer and steel reinforcement, resulting in better protection to the optical core; hence, it can be used for the actual field application. The coating of NanZee 0.9mm cable is thinner than NanZee 5mm cable. NanZee 0.9mm cable has less protection, but a more sensitive strain response is achieved.

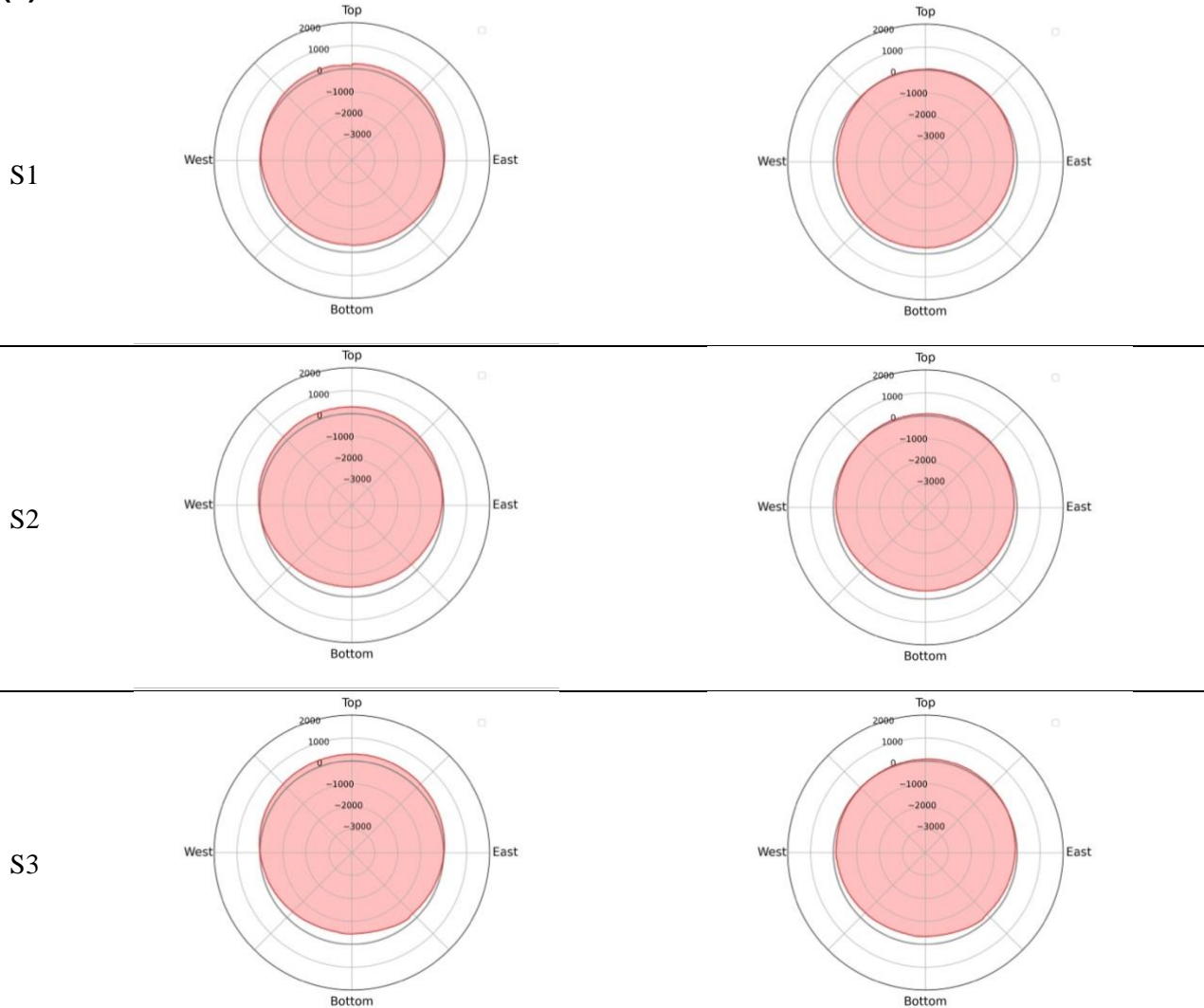
Table A-1 Schematic illustration of the selected strain sensor cable (Wu et al., 2015)

Brand	NanZee Sensing Technology Co.	NanZee Sensing Technology Co.
Model	NZS-DSS-C07	NZS-DSS-C02
Cross section		
Side view		

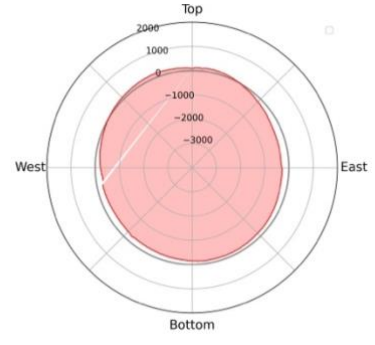
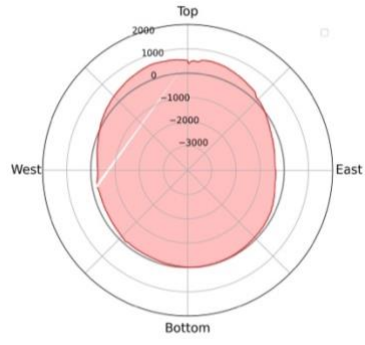
Appendix B: Distributed Fiber Optic Sensors Result

The results from the distributed fiber optic sensors are demonstrated herein. Plot (a) shows the strain distribution of the beginning state of the Pulling stage (i.e., the specimen first reaches the maximum rotation, 8.3 degrees). Plot (b) shows the strain distribution under 140 kips axial force condition.

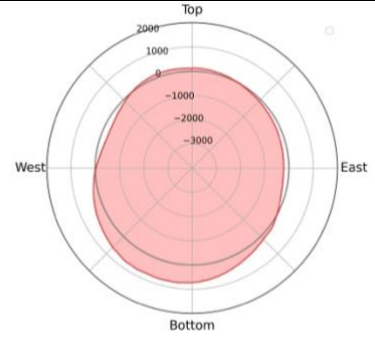
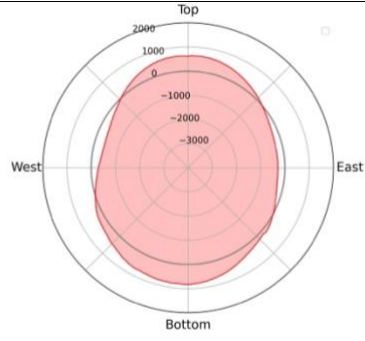
(a) Test 1



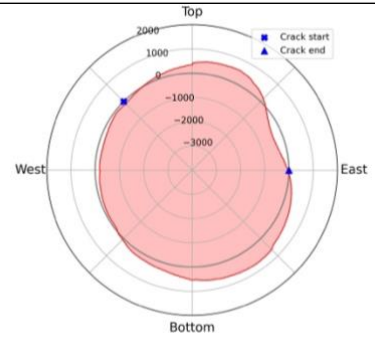
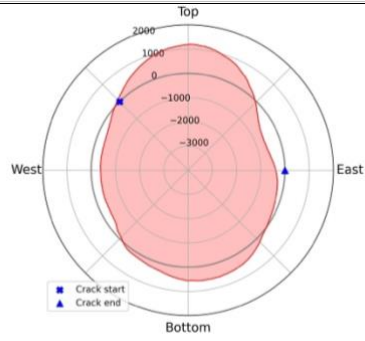
S4



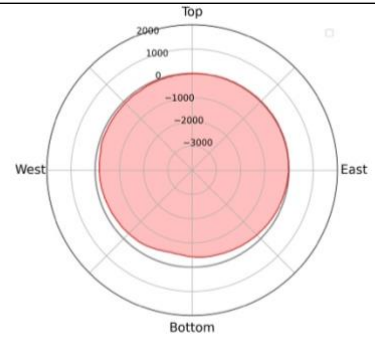
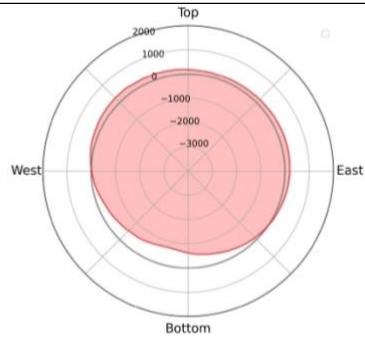
S5



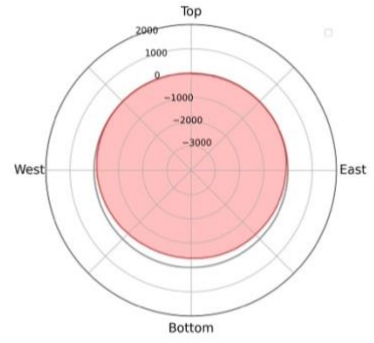
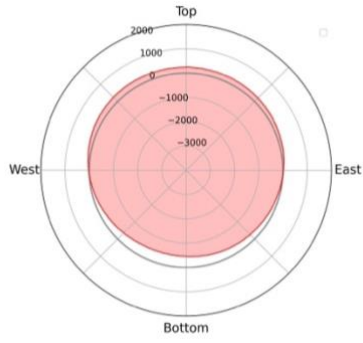
S6



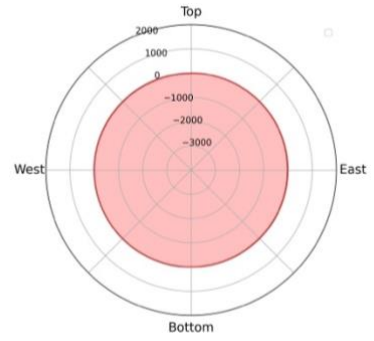
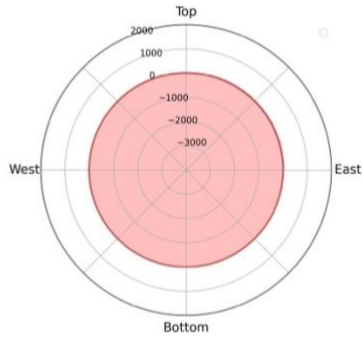
S7



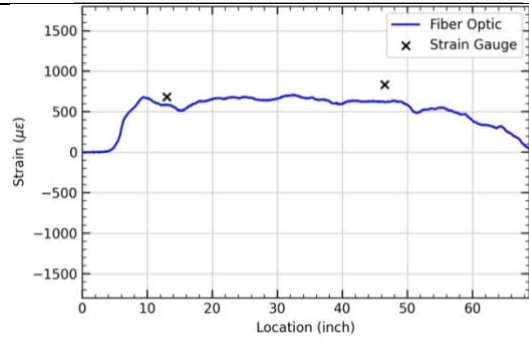
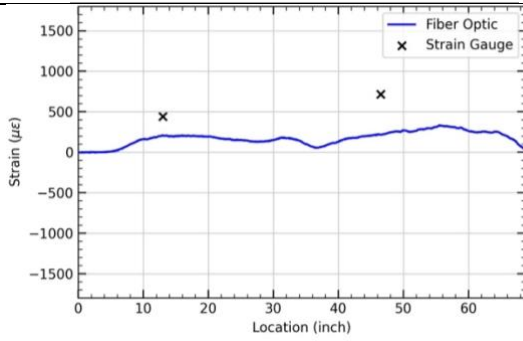
S8



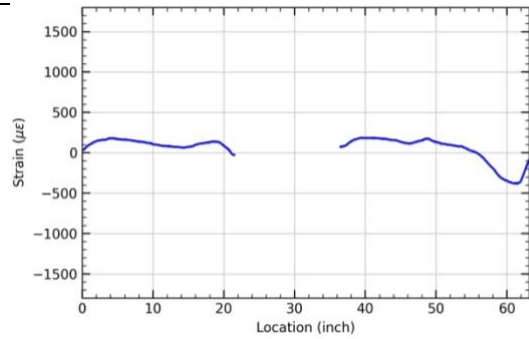
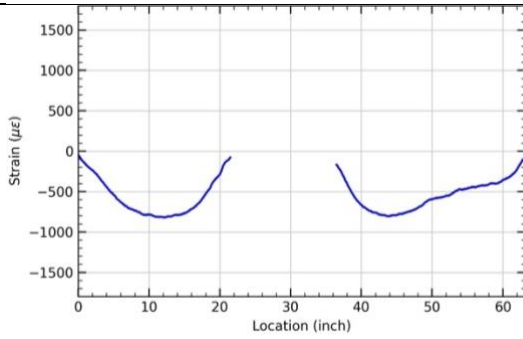
S9



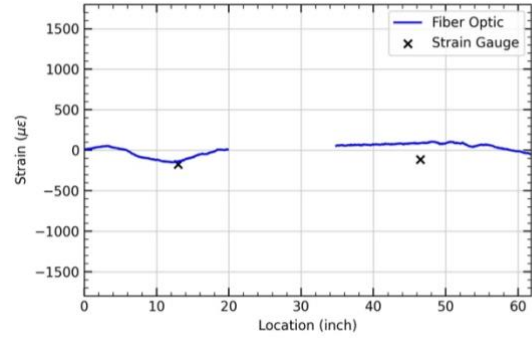
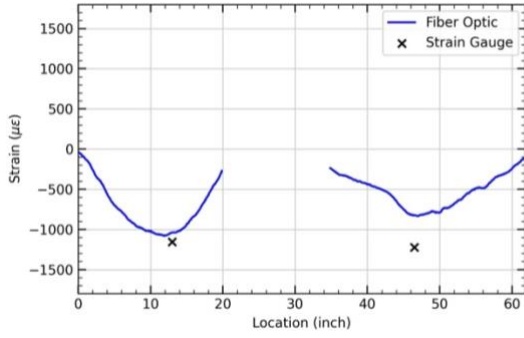
S10



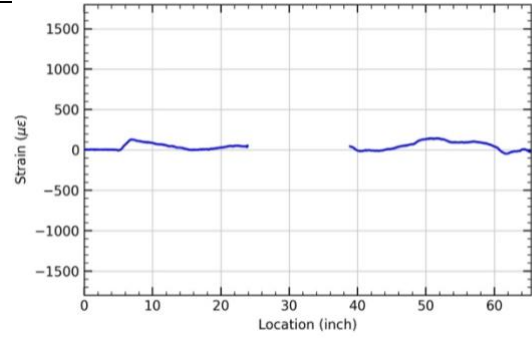
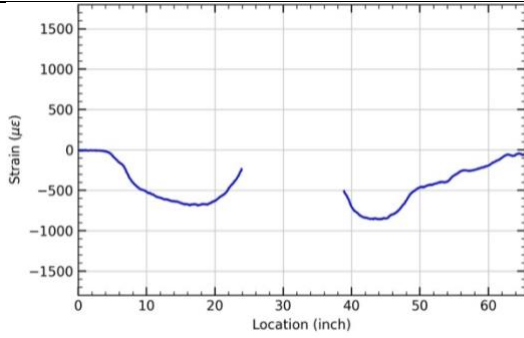
S11



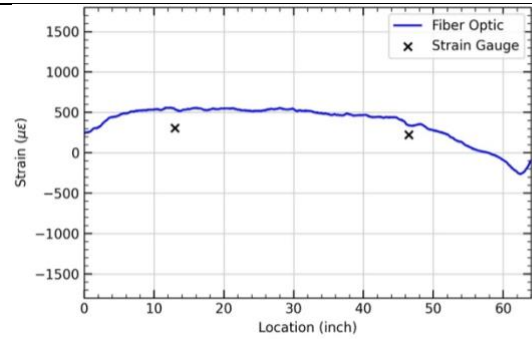
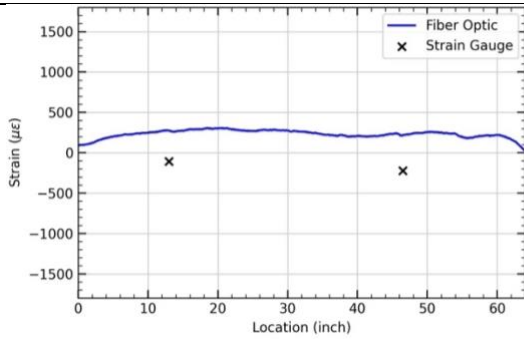
S12



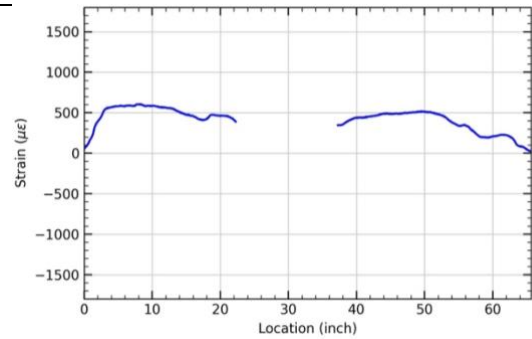
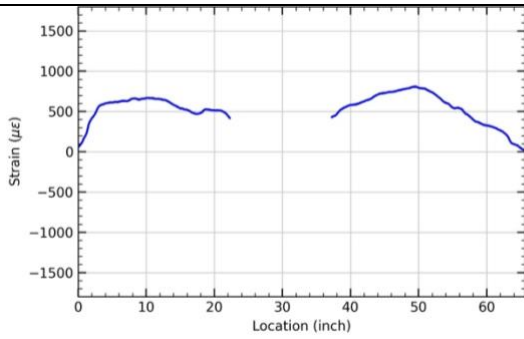
S13



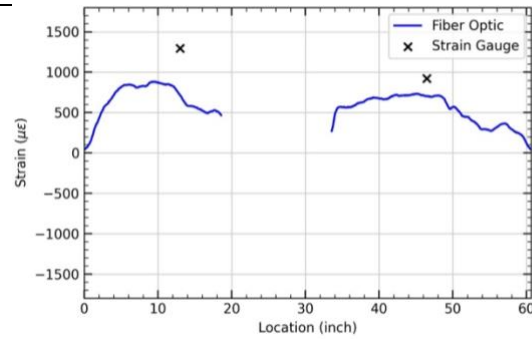
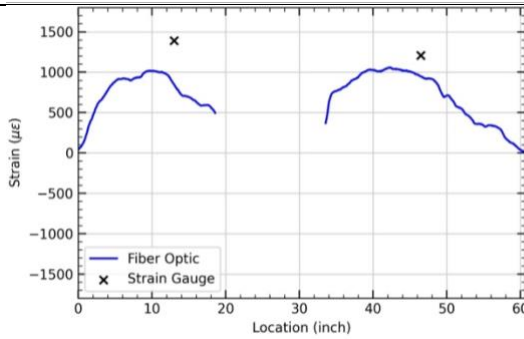
S14



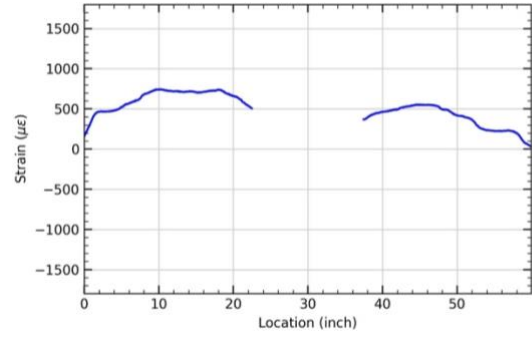
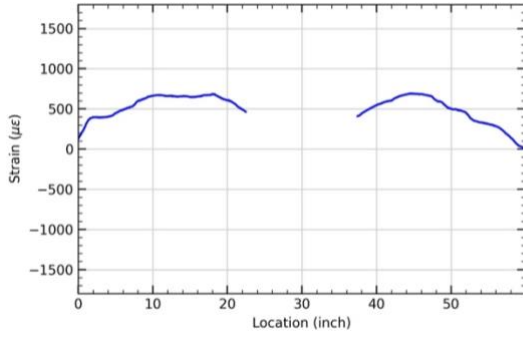
S15



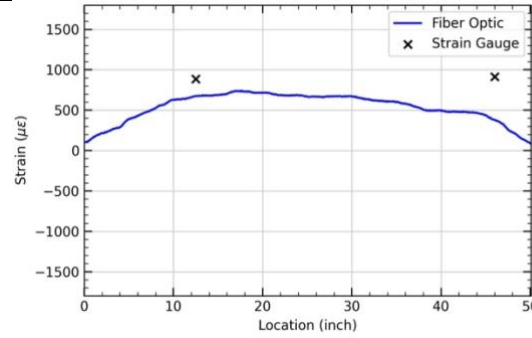
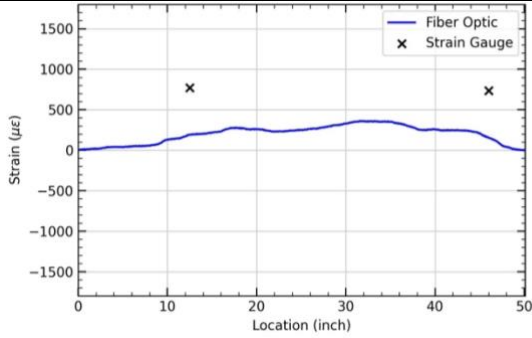
S16



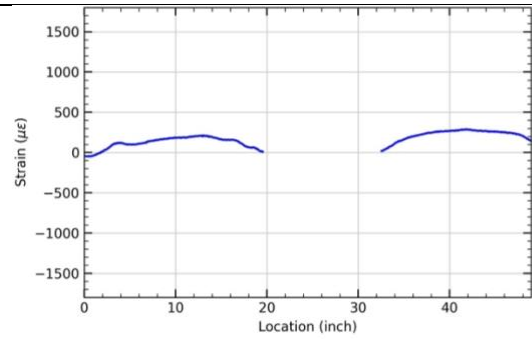
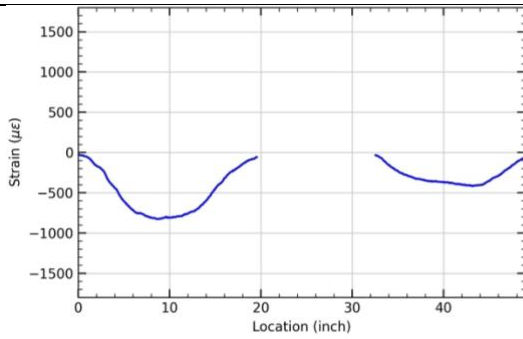
S17



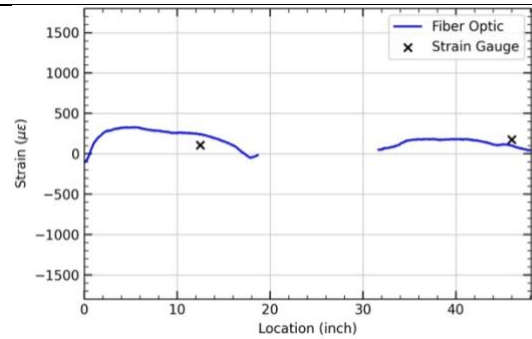
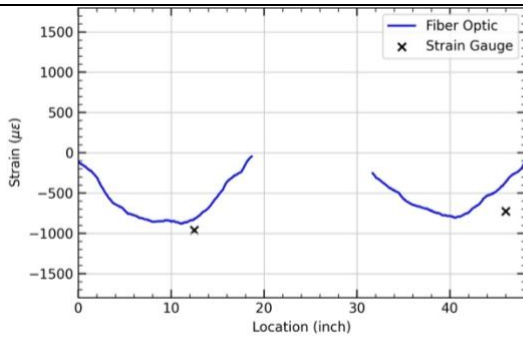
S18



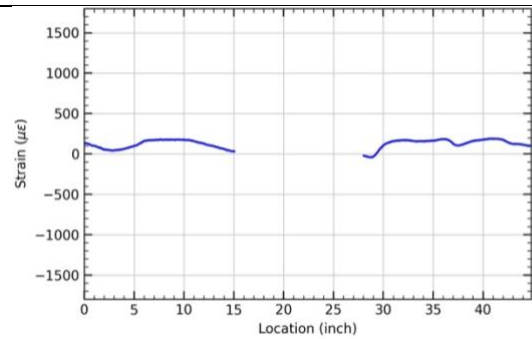
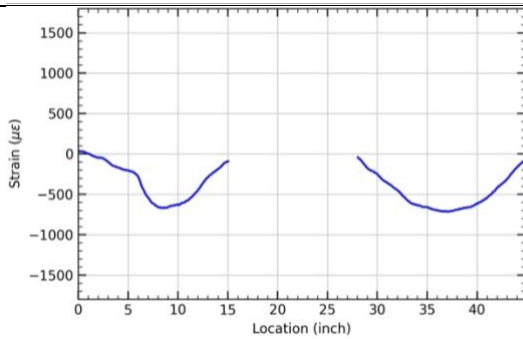
S19



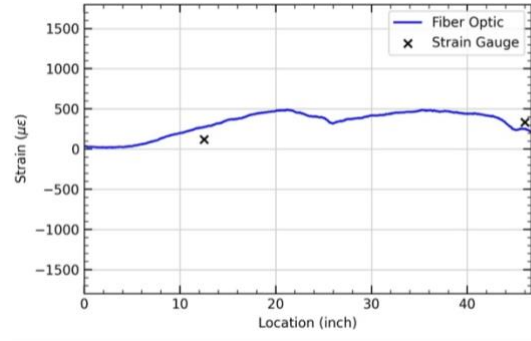
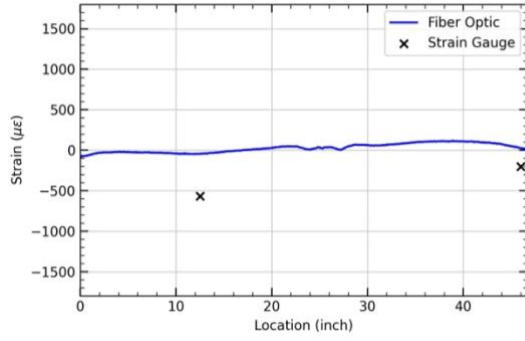
S20



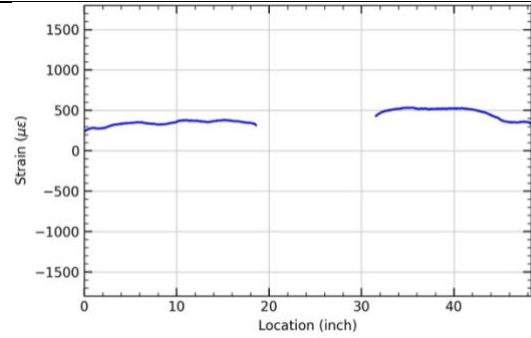
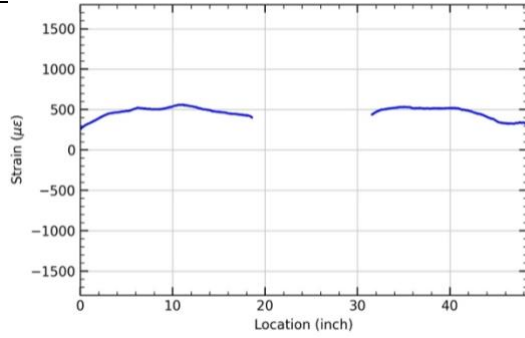
S21



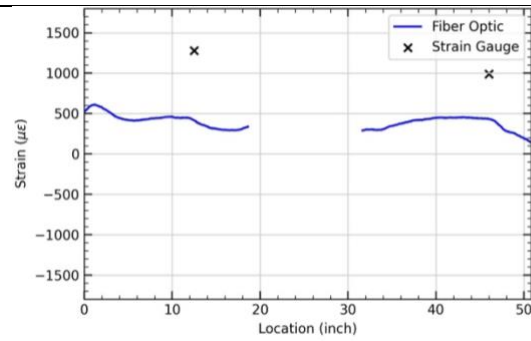
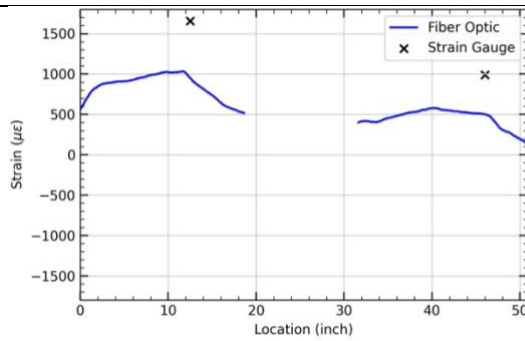
S22



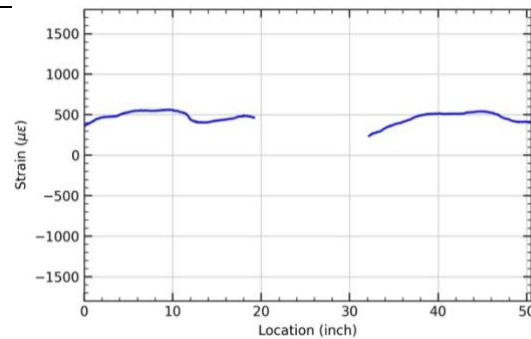
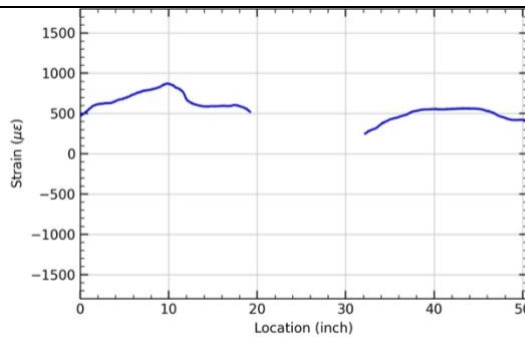
S23



S24



S25

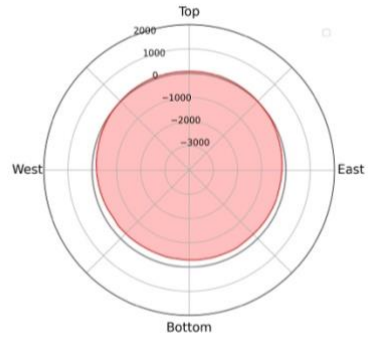
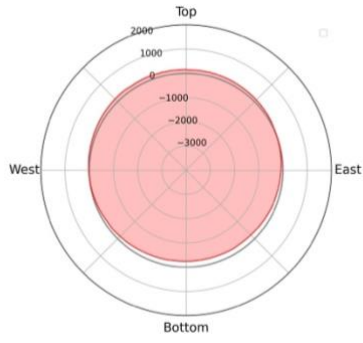


(a) Strain distribution under 8.3-degree rotation condition

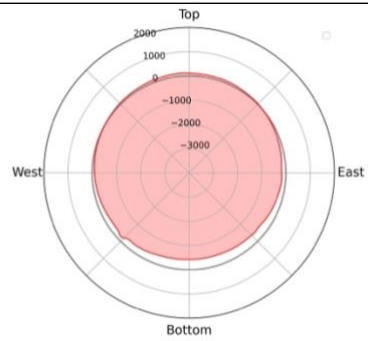
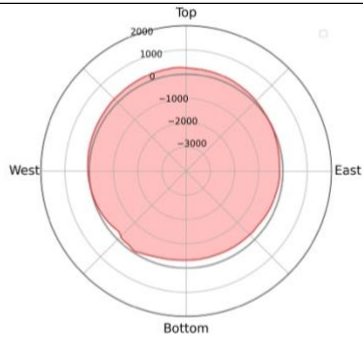
(b) Strain distribution under 140 kips axial force condition

(b) Test 2

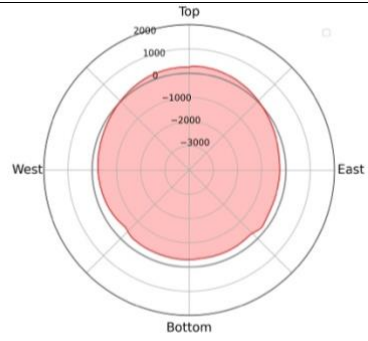
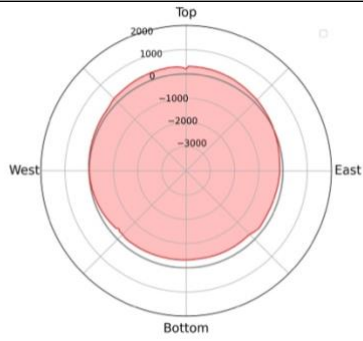
S1



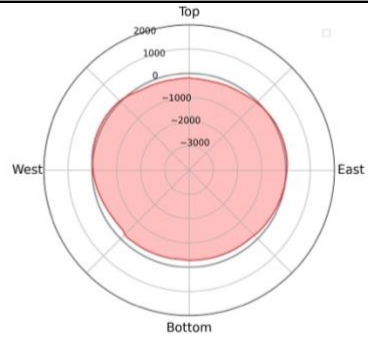
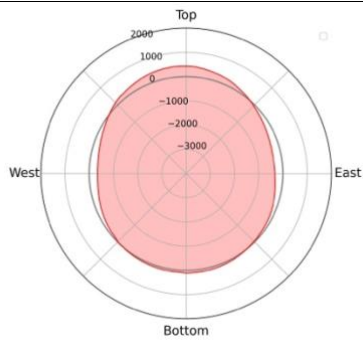
S2



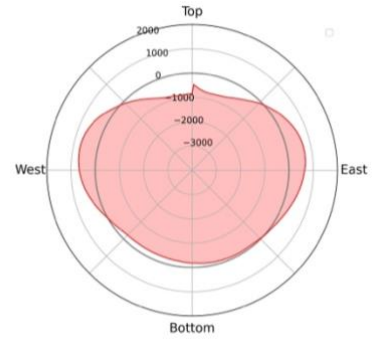
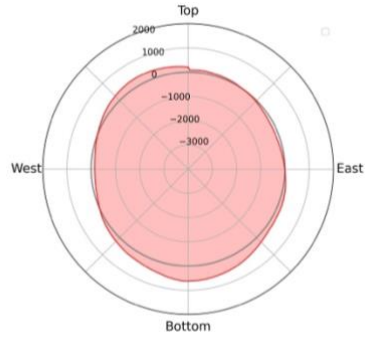
S3



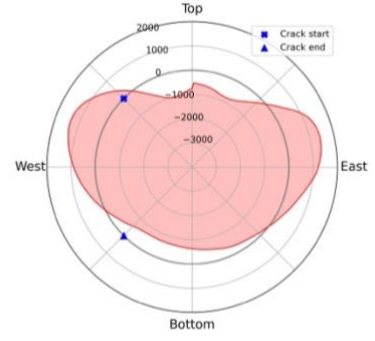
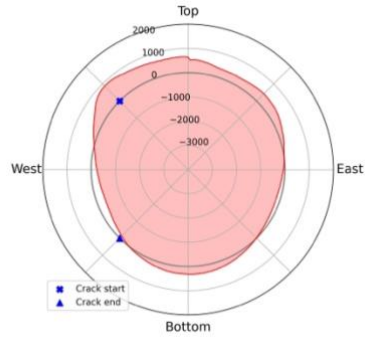
S4



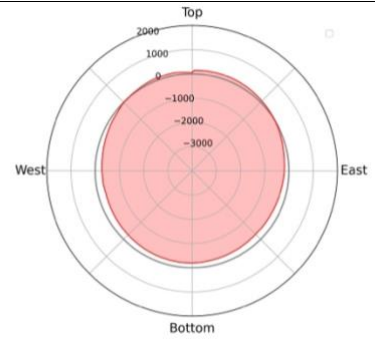
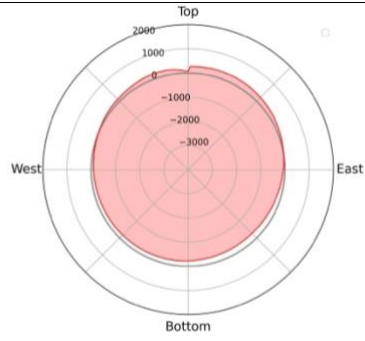
S5



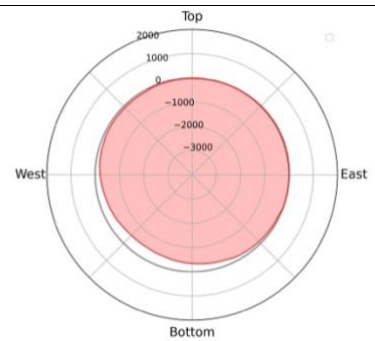
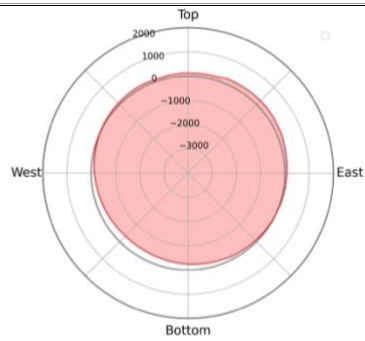
S6



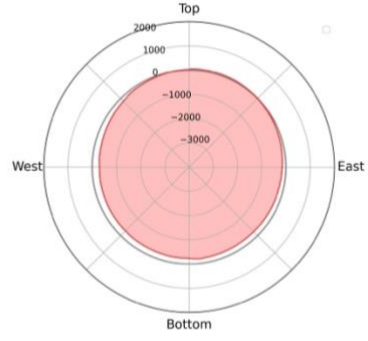
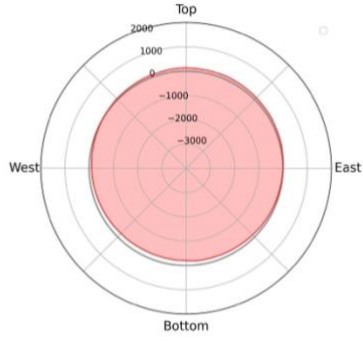
S7



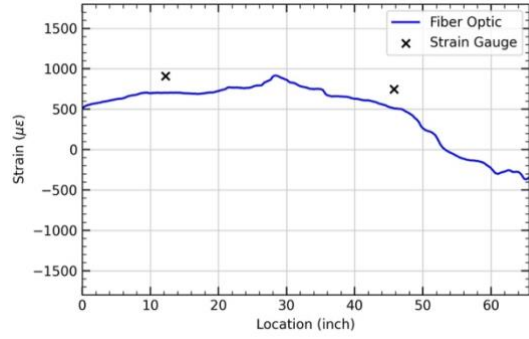
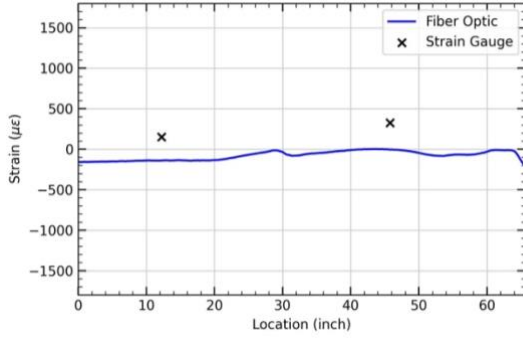
S8



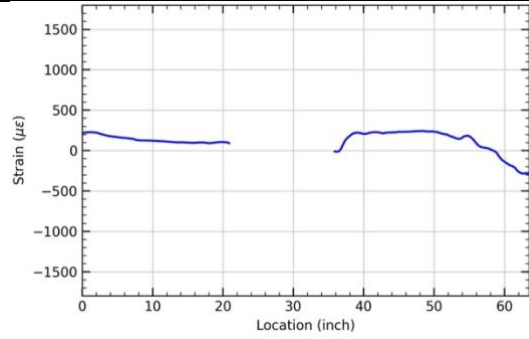
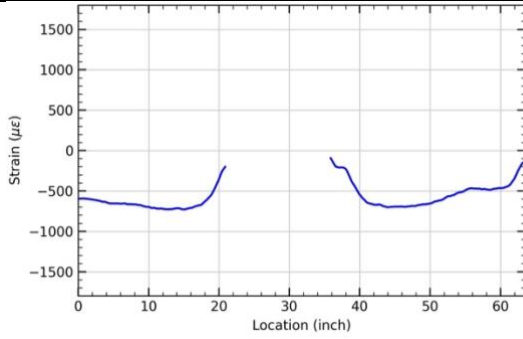
S9



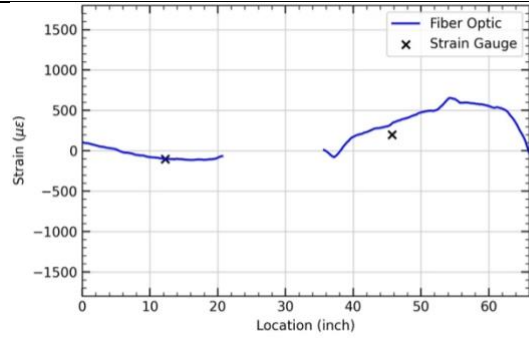
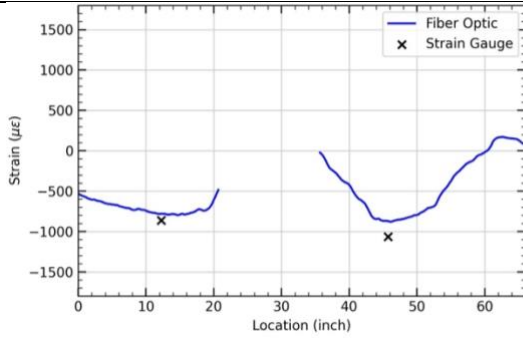
S10



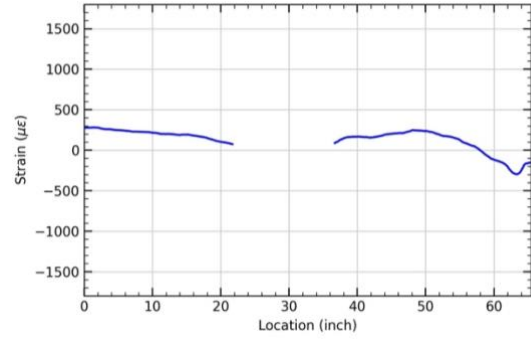
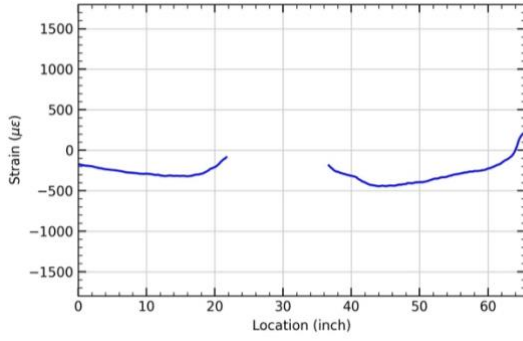
S11



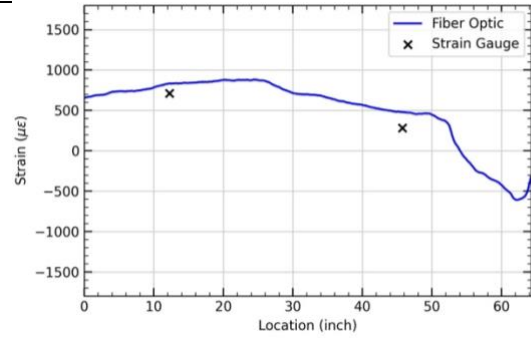
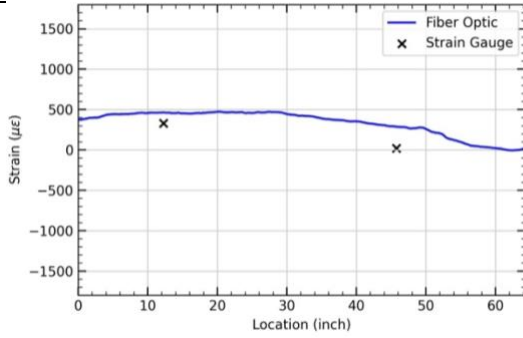
S12



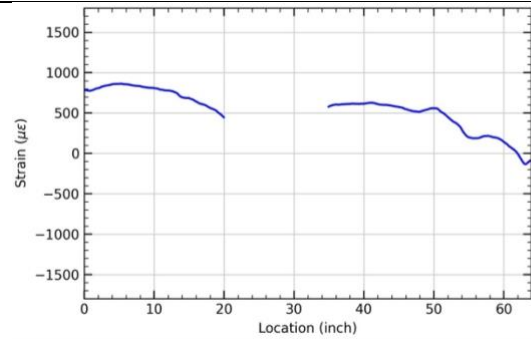
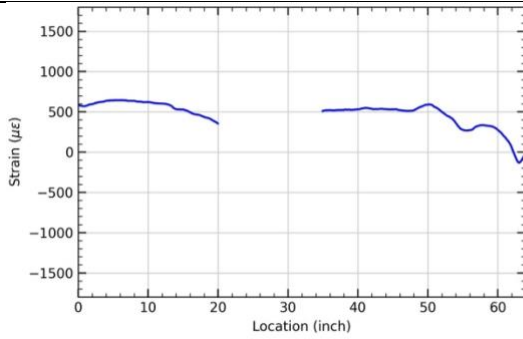
S13



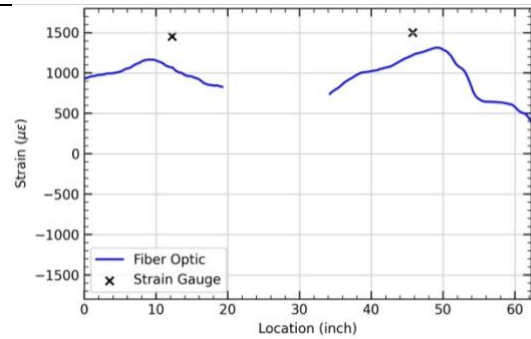
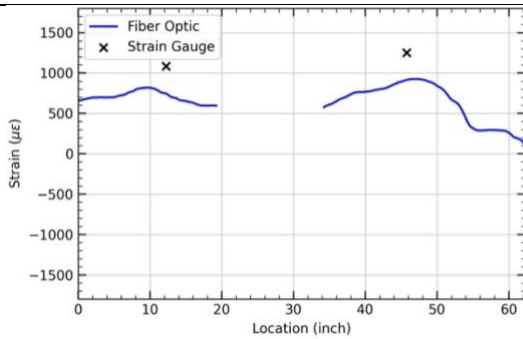
S14



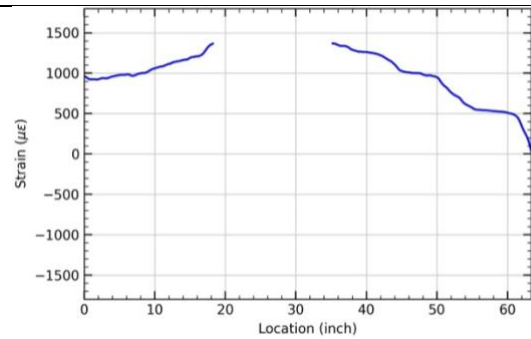
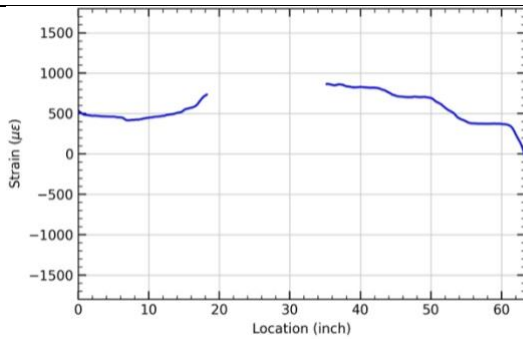
S15



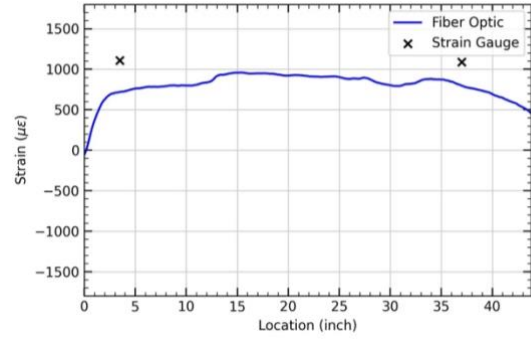
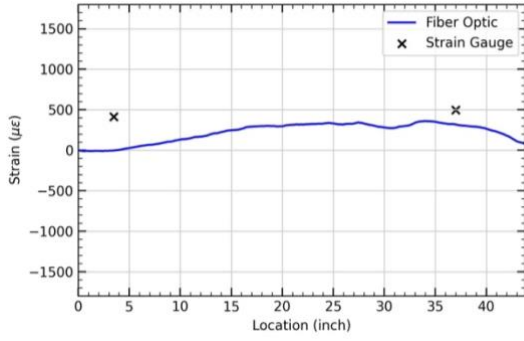
S16



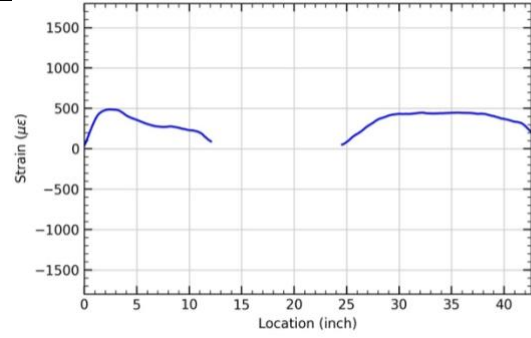
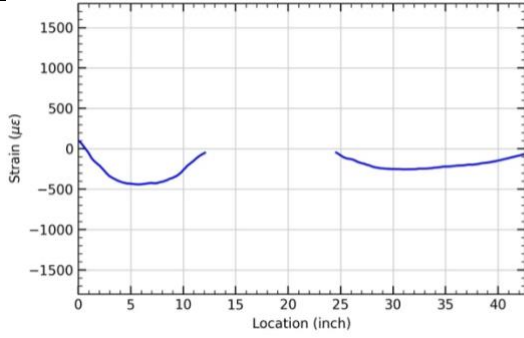
S17



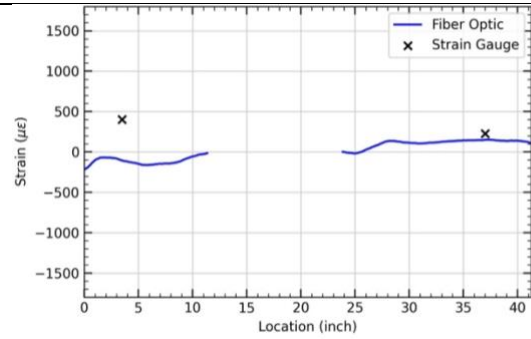
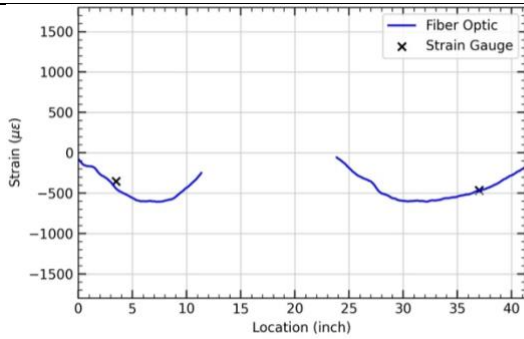
S18



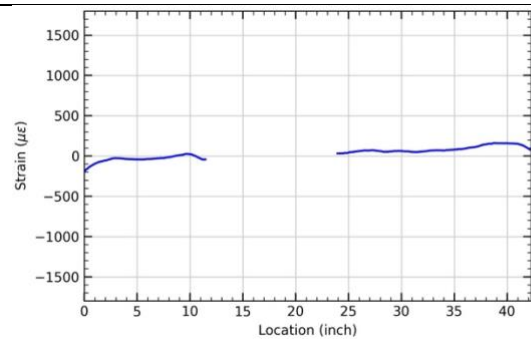
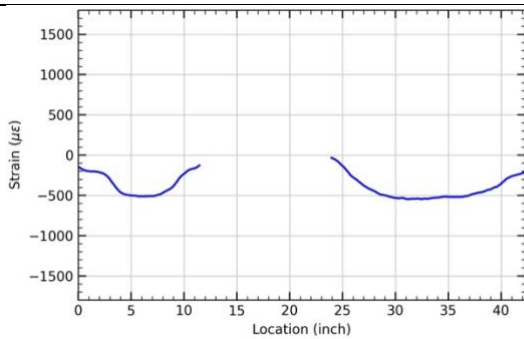
S19



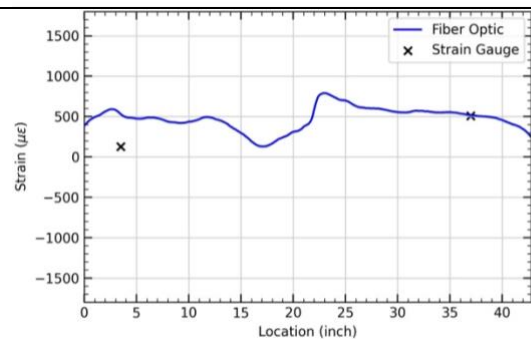
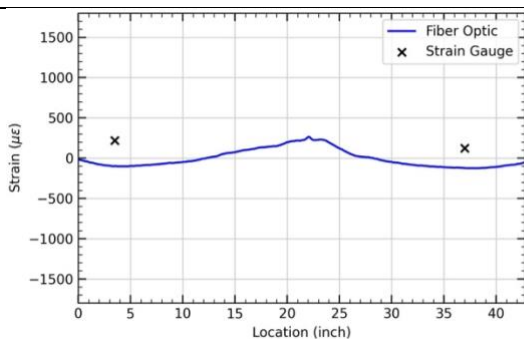
S20



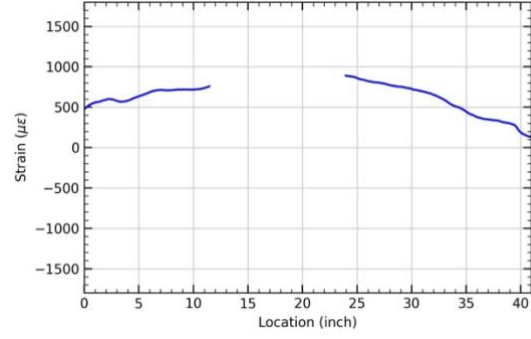
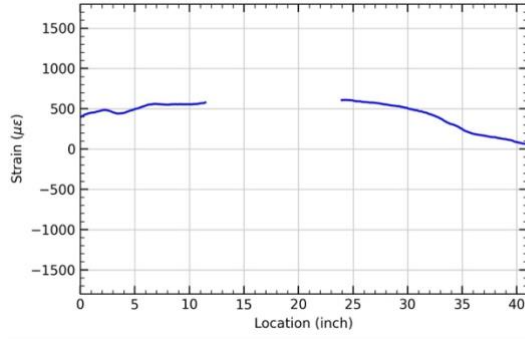
S21



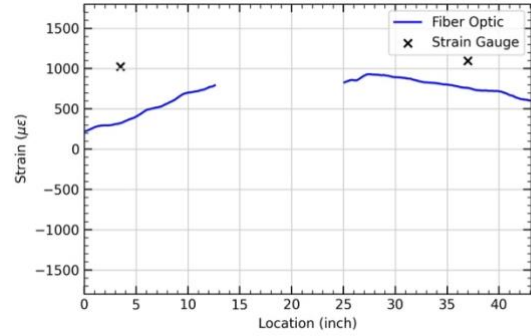
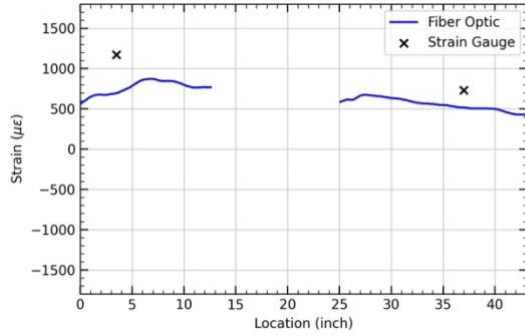
S22



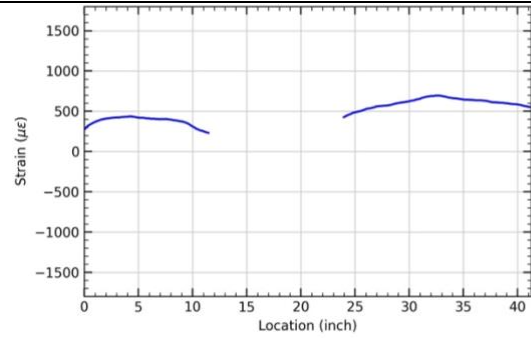
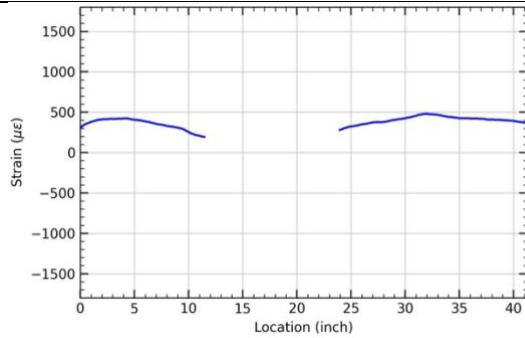
S23



S24



S25



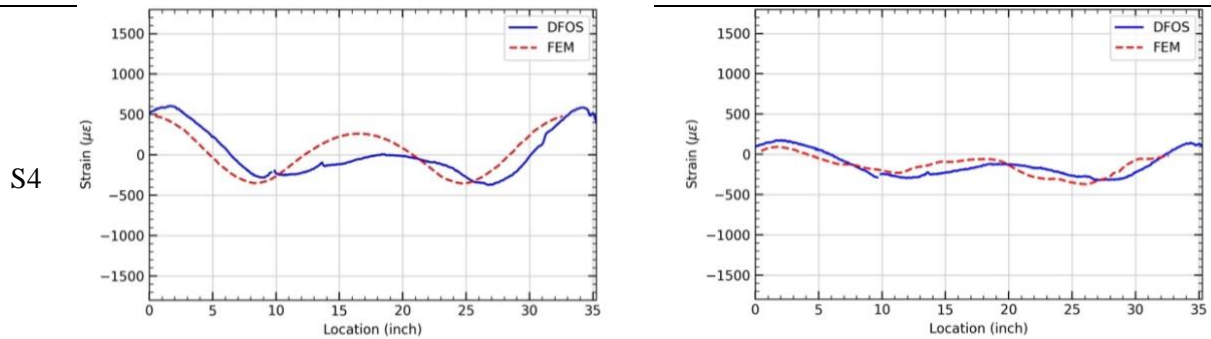
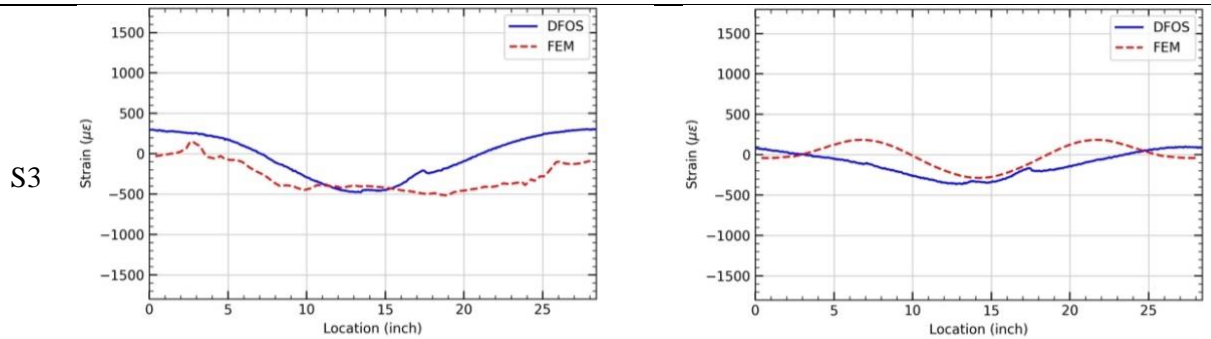
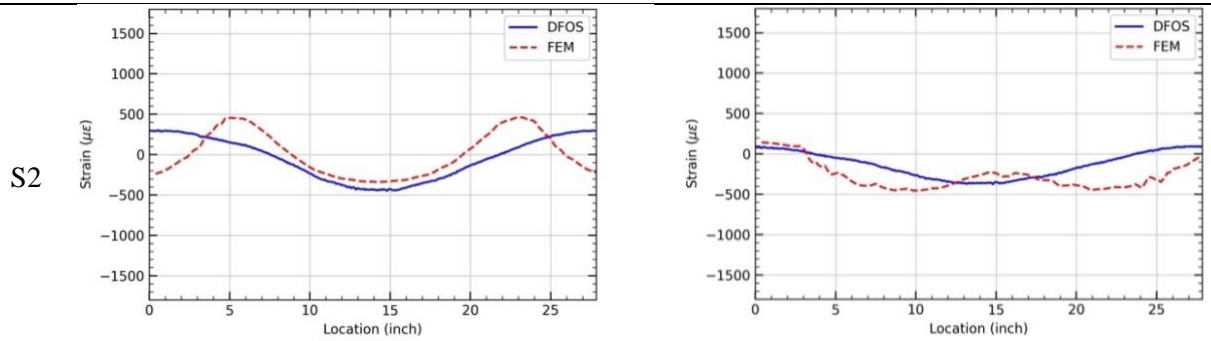
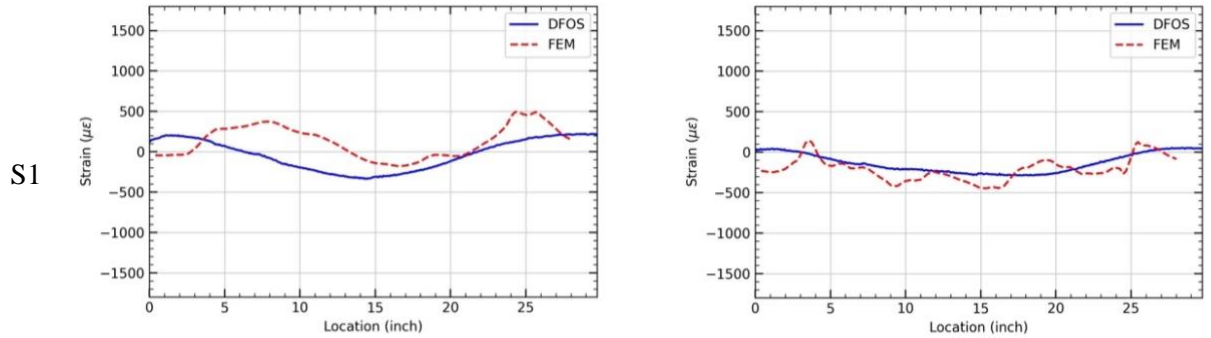
(a) Strain distribution under 8.3-degree rotation condition

(b) Strain distribution under 140 kips axial force condition

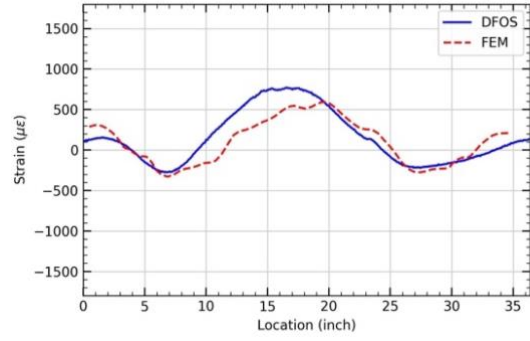
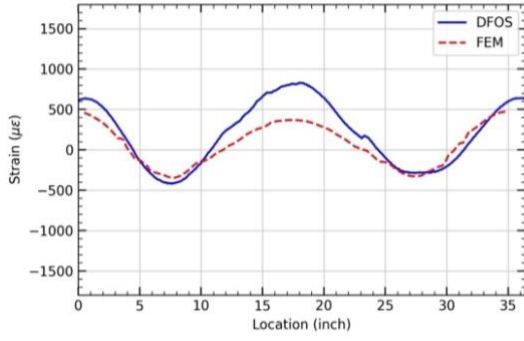
Appendix C: Comparison of FEM simulation results and experimental results

The experimental data were compared to the results from the F.E. model. All the comparison results are shown in this section.

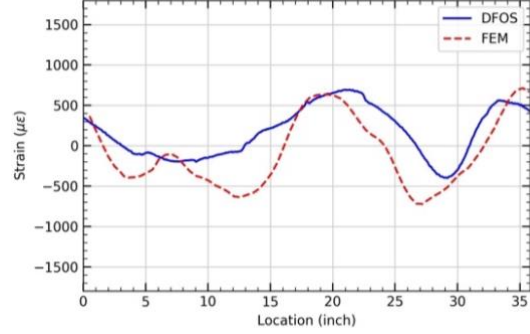
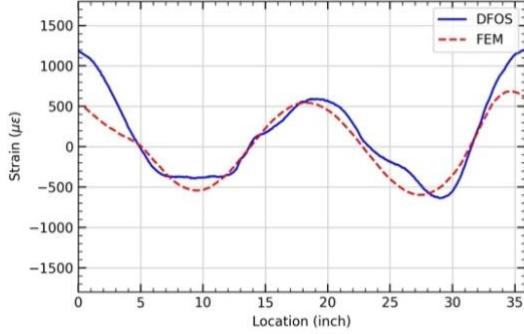
(a) Test 1



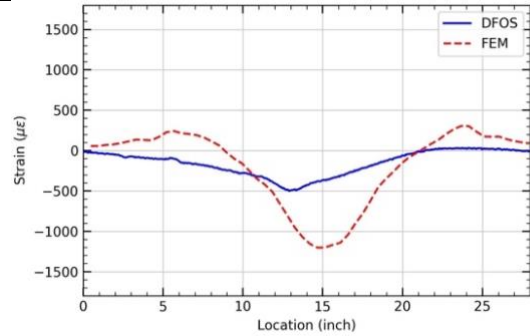
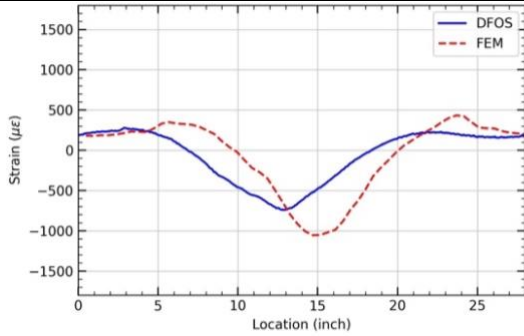
S5



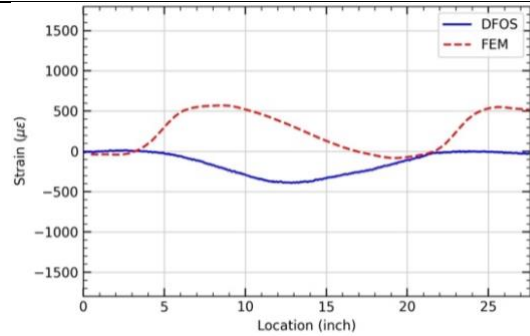
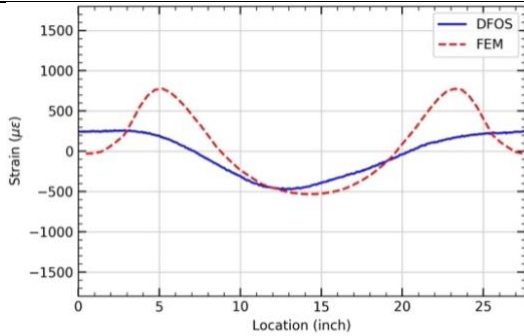
S6



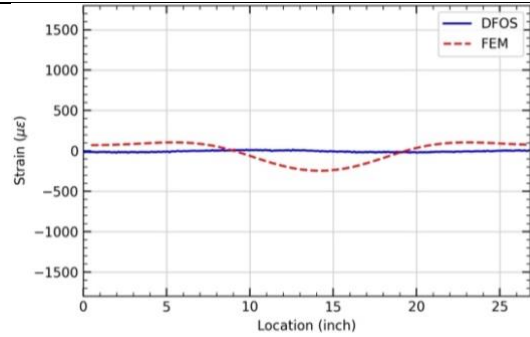
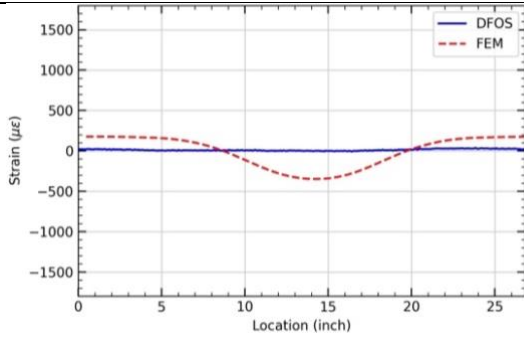
S7



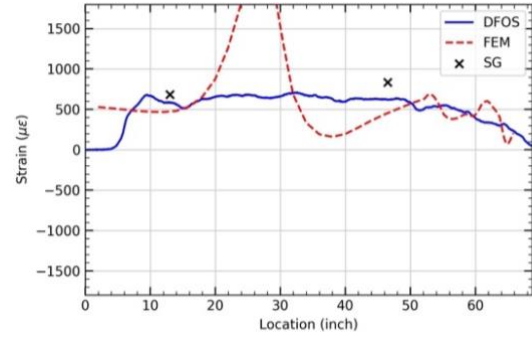
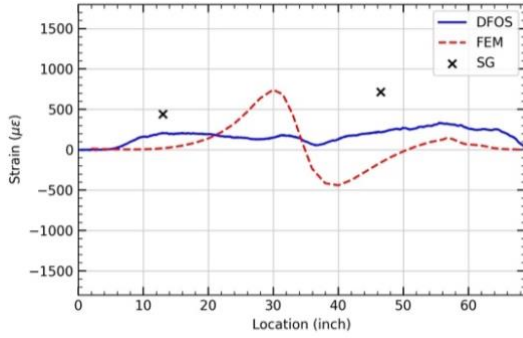
S8



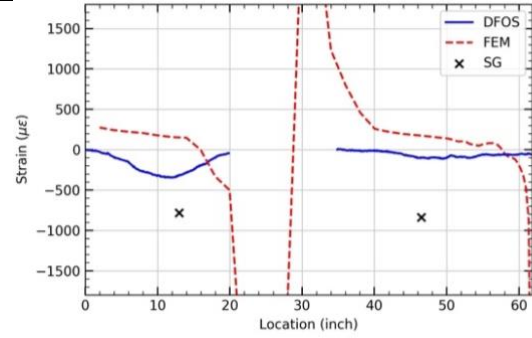
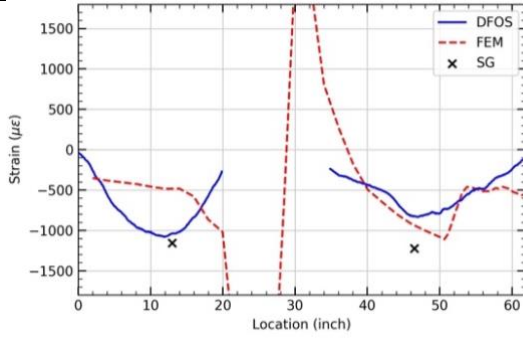
S9



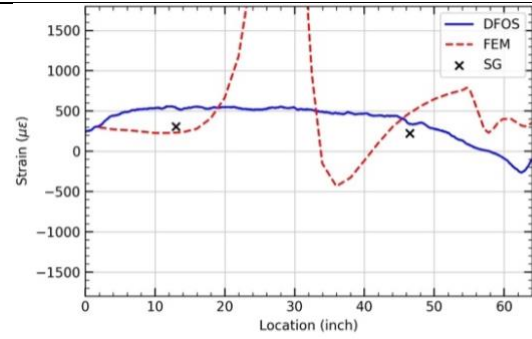
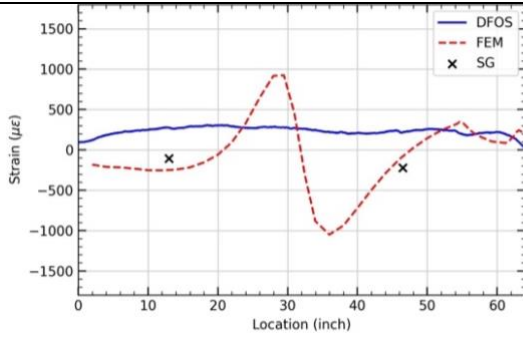
S10



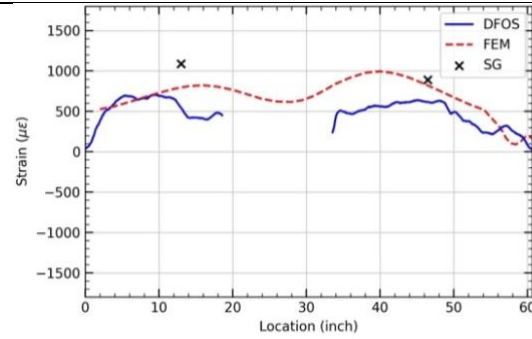
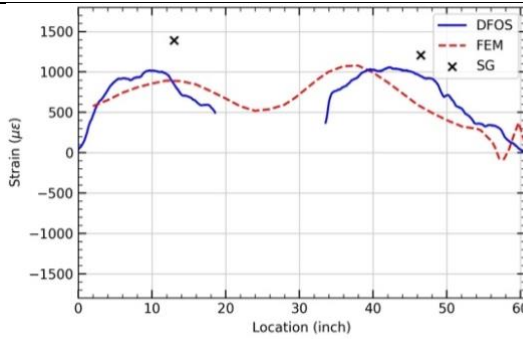
S12



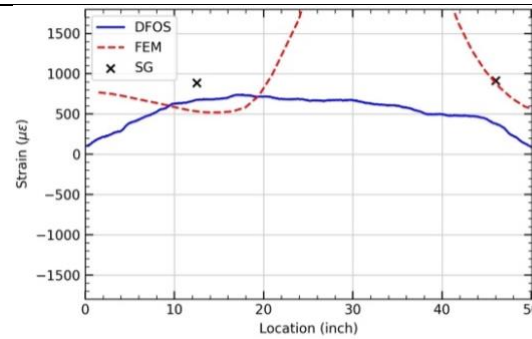
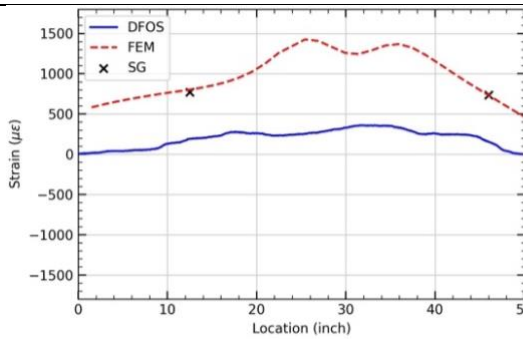
S14



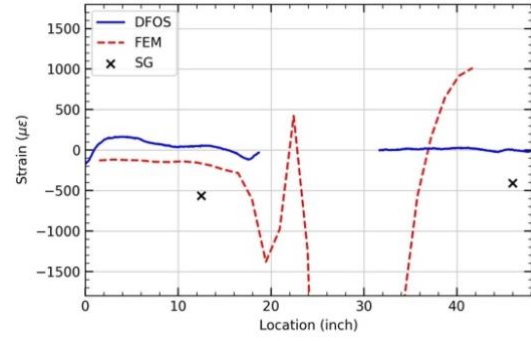
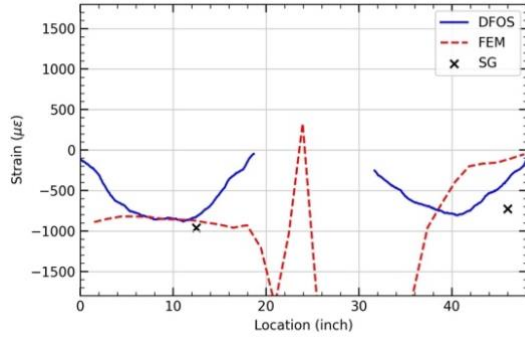
S16



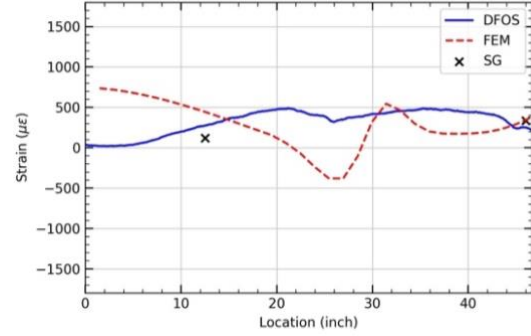
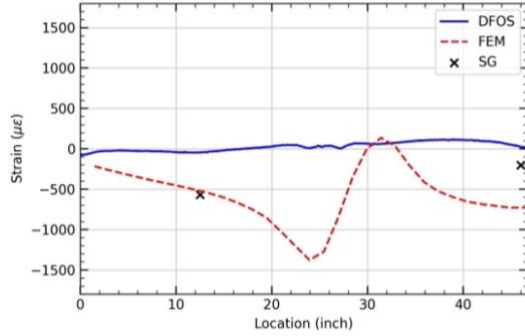
S18



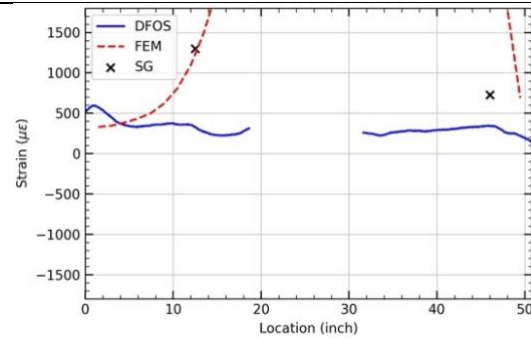
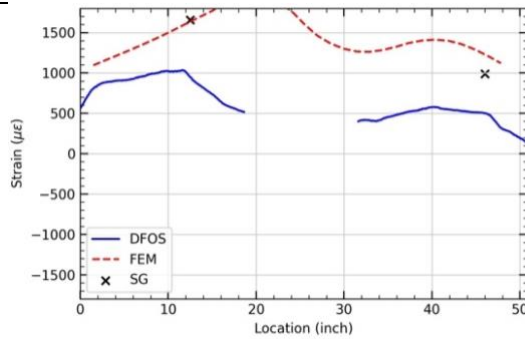
S20



S22



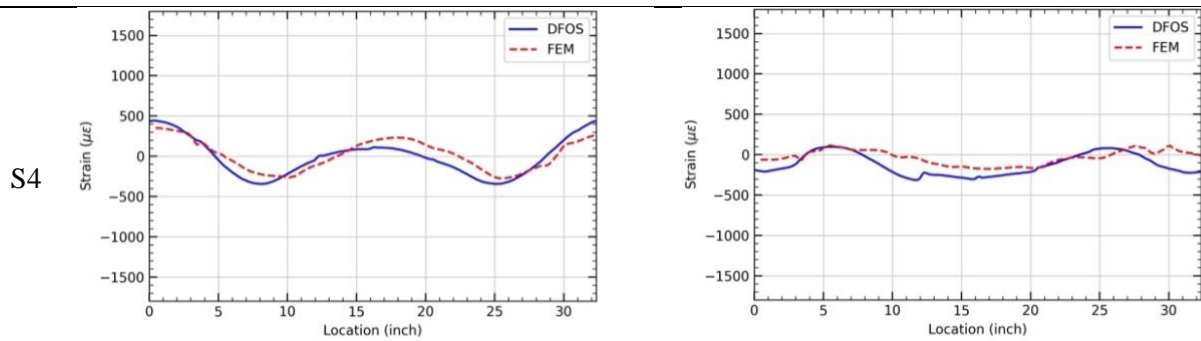
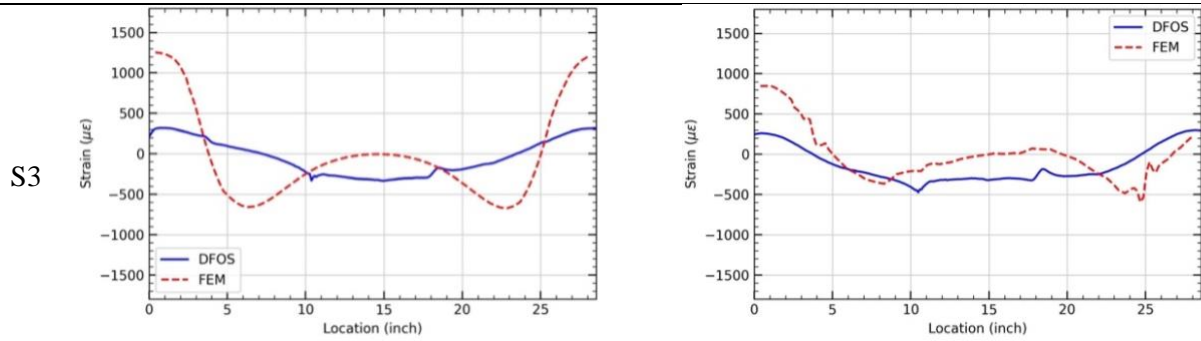
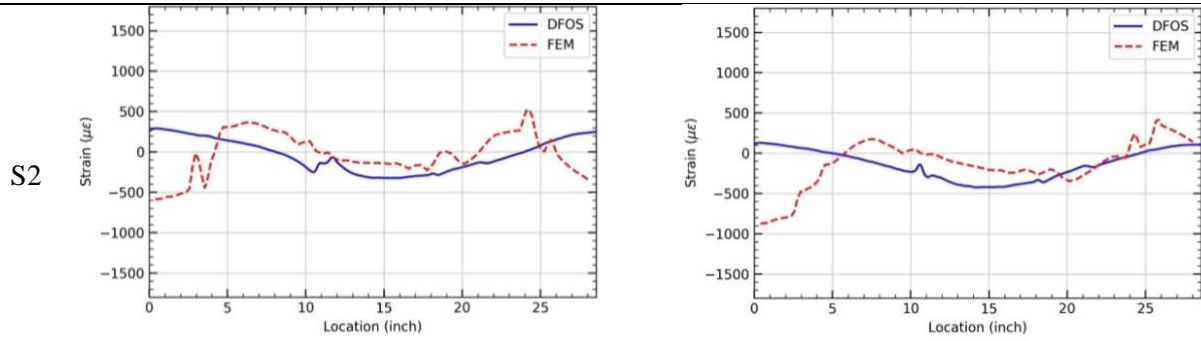
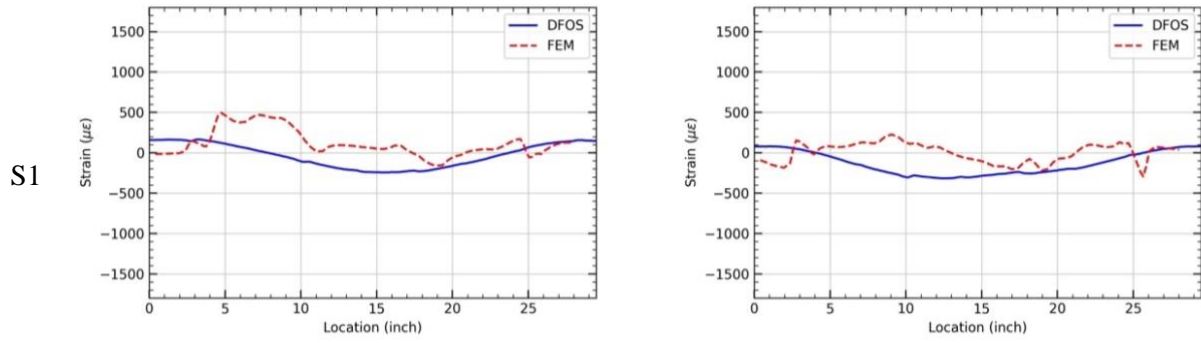
S24



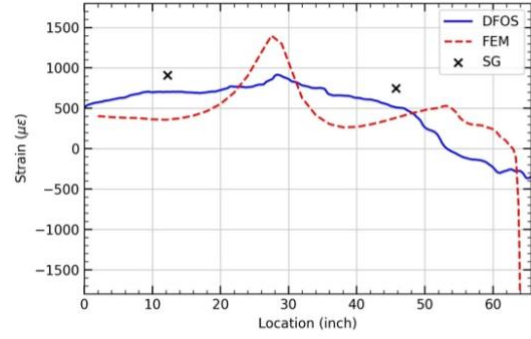
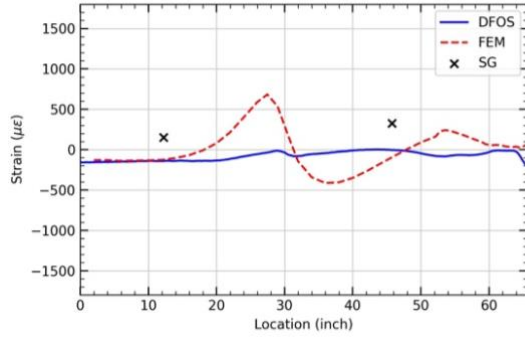
(a) Strain distribution under 8.3-degree rotation condition

(b) Strain distribution under 2.2 inches axial displacement condition

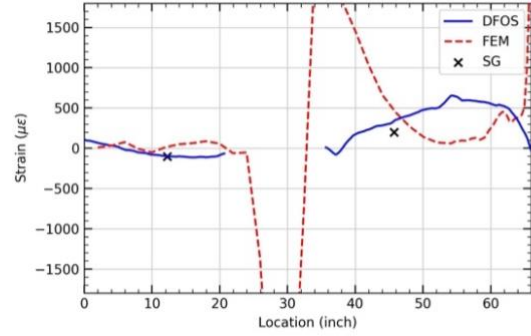
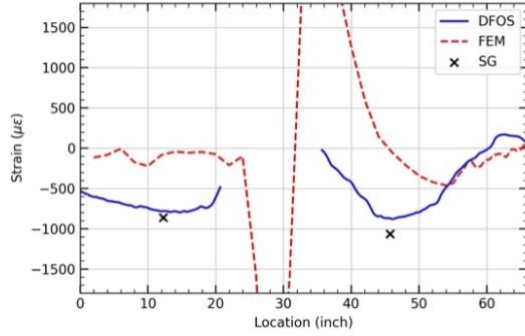
(b) Test 2



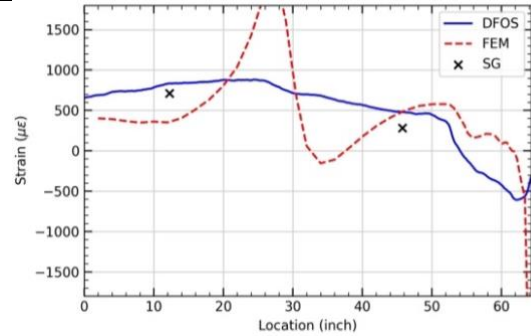
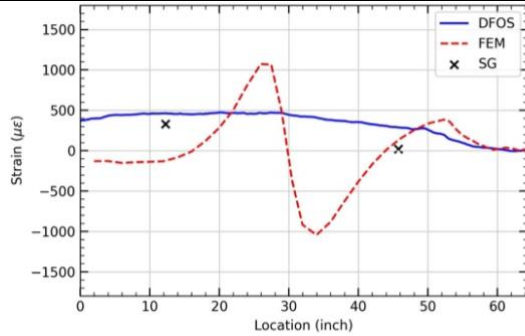
S10



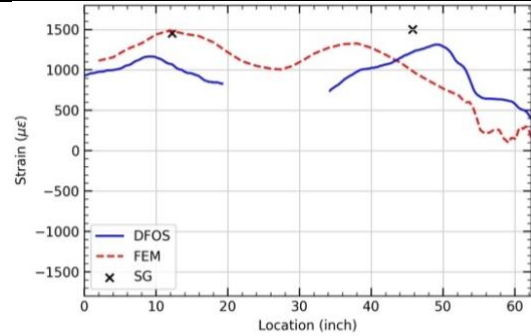
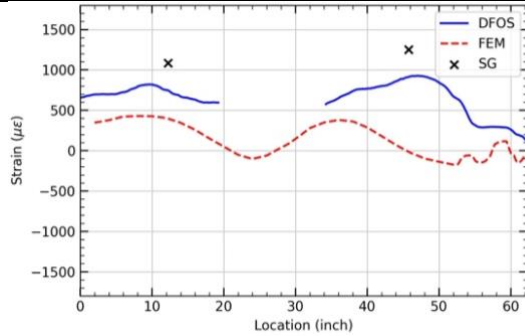
S12



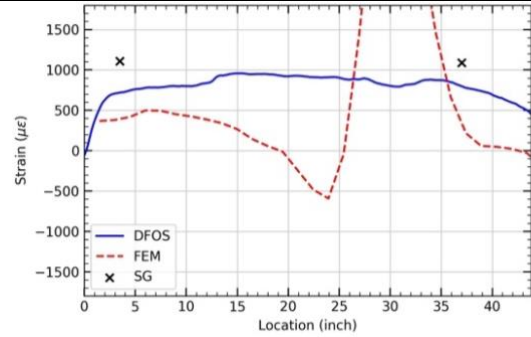
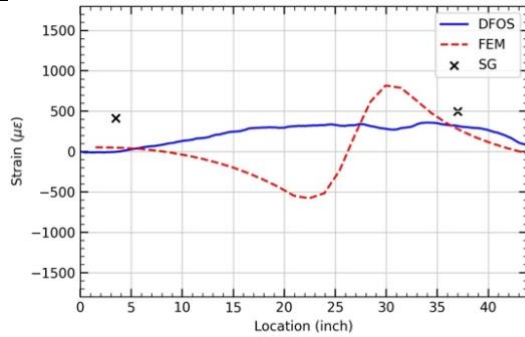
S14



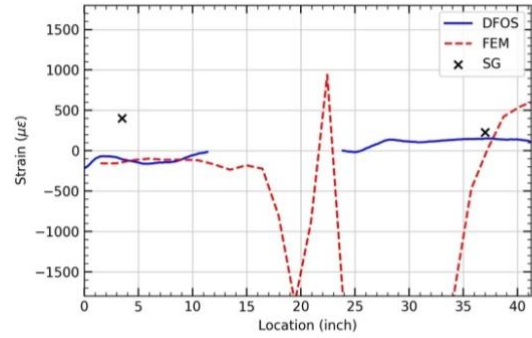
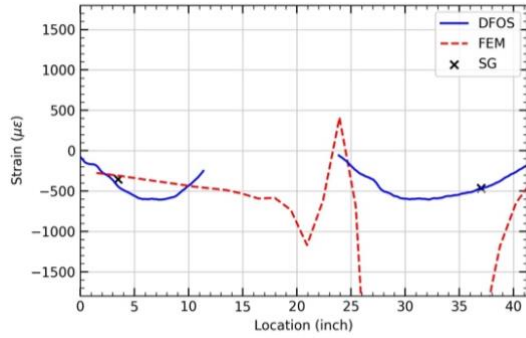
S16



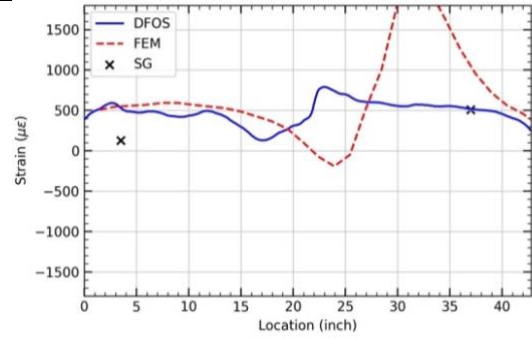
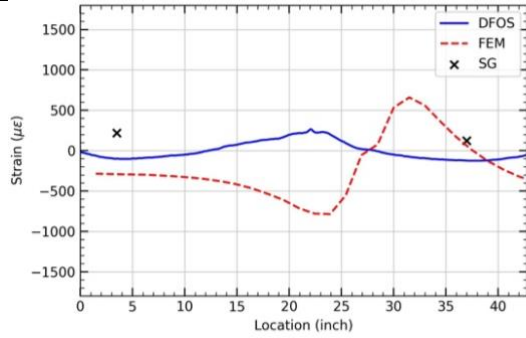
S18



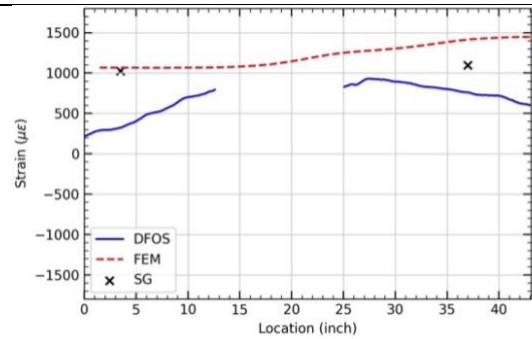
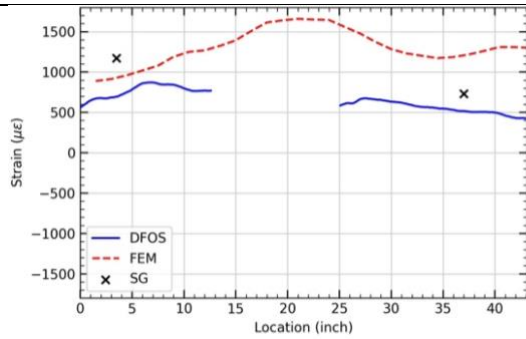
S20



S22



S24



(a) Strain distribution under 8.3-degree rotation condition

(b) Strain distribution under 2.2 inches axial displacement condition